Dynamique et stabilité de tourbillons avec écoulement axial

Clément Roy

▶ **To cite this version:**

Clément Roy. Dynamique et stabilité de tourbillons avec écoulement axial. Dynamique des Fluides [physics.flu-dyn]. Université de Provence - Aix-Marseille I, 2008. Français. NNT : . tel-00436894

HAL Id: tel-00436894

https://theses.hal.science/tel-00436894

Submitted on 27 Nov 2009

HAL is a multi-disciplinary open access archive for the deposit and dissemination of scientific research documents, whether they are published or not. The documents may come from teaching and research institutions in France or abroad, or from public or private research centers.

L'archive ouverte pluridisciplinaire **HAL**, est destinée au dépôt et à la diffusion de documents scientifiques de niveau recherche, publiés ou non, émanant des établissements d'enseignement et de recherche français ou étrangers, des laboratoires publics ou privés.

UNIVERSITÉ DE PROVENCE AIX-MARSEILLE I
Institut de Recherche sur les Phénomènes Hors Équilibre
et
MONASH UNIVERSITY, MELBOURNE, AUSTRALIE
Department of Mechanical Engineering

THÈSE

présentée pour obtenir le grade de

DOCTEUR DE L'UNIVERSITÉ DE PROVENCE

Discipline : Systèmes Complexes : Phénomènes Hors Équilibre, Micro et Nano Électronique
École Doctorale : Mécanique, Physique, Micro et Nanoélectronique

par

Clément ROY

le 10 otobre 2008

Dynamique et stabilité de tourbillons avec écoulement axial

Directeurs de thèse :

M. Thomas LEWEKE
M. Mark. C. THOMPSON
M. Kerry HOURIGAN

JURY :

M. David FABRE	
M. Kerry HOURIGAN	
M. Thomas LEWEKE	
M. Charles H. K. WILLIAMSON	*Rapporteur*
M. Jean-M. CHOMAZ	*Rapporteur*

Table des matières

Chapitre 1

Introduction

1.1 Contexte de l'étude

Cette étude porte sur les tourbillons avec un écoulement axial. On entend ici que la vitesse axiale au centre du tourbillon n'est pas égale à la vitesse axiale à l'extérieur. Ces écoulements sont typiques de ceux rencontrés dans le sillage tourbillonnaire des avions. Pour un avion suiveur, ils représentent un danger potentiel. En effet, un tourbillon génère sur un avion qui le traverse en son centre un moment de roulis qui est proportionnel à sa circulation (Fabre, 2002). L'avion risque alors de se retourner. Le risque qu'un avion rencontre le sillage d'un autre est le plus important dans les environs d'un aéroport. Pour minimiser ce risque, la *Federal Aviation Administration* (FAA) impose alors des temps d'attente entre le passage successifs de deux avions, de manière à ce que le sillage du premier ne soit plus dangereux pour le passage du second. Les avionneurs, pour des raisons économiques liées à la cadence de décollage, ont tout intérêt à ce que le sillage de leurs avions soit le moins dangereux possible. C'est à eux de prouver que le sillage de l'avion vérifie certains critères de sécurité pour que la FAA diminue le temps d'attente imposé après leur décollage. Des projets de recherche sont financés dans le but de trouver un moyen de réduire le danger du sillage. De nombreux projets internationaux sont créés dans ce but. En Europe, les recherches sont motivées par Airbus, qui vient de sortir le gros porteur A380. Par exemple, le projet FAR-Wake auquel ce travail a contribué, aborde le problème du point de vue fondamental. C'est dans ce contexte que cette étude se positionne.

La figure 1.1 présente le sillage typique d'un avion en phase de décollage. Les volets sont utilisés dans cette phase pour augmenter la portance de l'avion. Une paire de tourbillons est alors générée de chaque côté de l'avion. Ces tourbillons possèdent une circulation de même signe : ils sont co-rotatifs. Les deux tourbillons vont alors tourner l'un autour de l'autre en se rapprochant jusqu'à fusionner. Les deux tourbillons résultants ainsi créés (un tourbillon par aile) forment une paire de vortex contra–rotatifs. C'est ce sillage lointain de l'avion qui est dangereux car il peut persister longtemps aux environs des aéroports.

Une des façons d'accélerer la destruction d'un tourbillon est de le rendre instable. La mission principale de cette thèse est d'étudier une instabilité que l'on appelle "instabilité elliptique" successible de se propager dans des paires de tourbillons avec écoulement axial, similaires à celles observées dans les sillages des

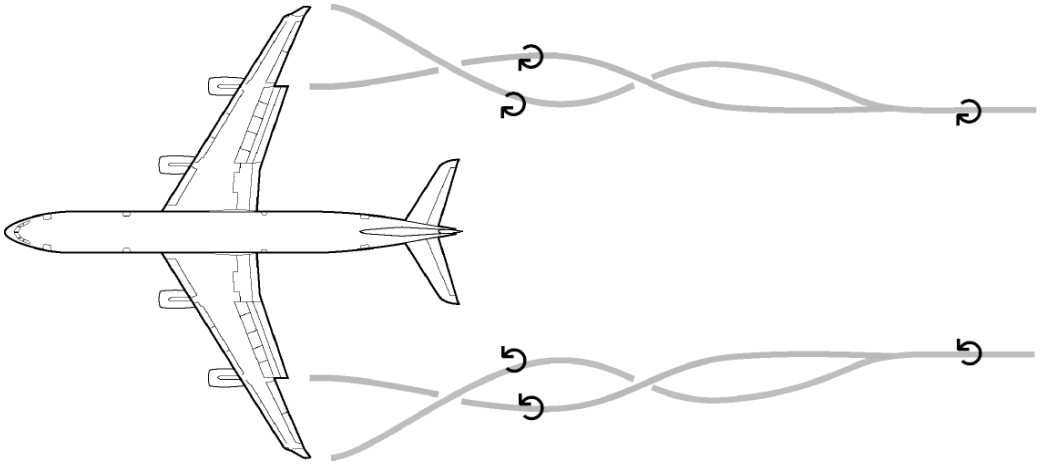

FIG. 1.1 – Sillage simplifié d'un avion en configuration de décollage ou d'atterrissage.

avions. Les connaissances sur l'instabilité elliptique sont déjà très avancées concernant les tourbillons sans écoulement axial. Le but de cette étude est d'étendre ces connaissances dans le cas où un écoulement axial est présent dans les tourbillons, de manière à rendre l'instabilité prédictible dans ce cas. C'est la première des étapes nécessaires à une éventuelle application aéronautique pour accélerer la disparition du sillage d'un avion.

La partie expérimentale de cette étude nécessite la génération de tourbillons avec écoulement axial. La méthode choisie pour réaliser cela est de placer une aile dans un écoulement créé par un canal à eau. La création d'un vortex de cette manière est toujours accompagnée d'un phénomène appelé communément "vortex meandering" ou "flottement du tourbillon". On peut le décrire comme un mouvement ondulatoire de translation du tourbillon à grande longueur d'onde. Ce phénomène, dont l'origine n'est pas clairement définie, vient parasiter l'écoulement. Une partie de l'étude lui sera alors consacrée de manière à le caractériser.

1.2 Modèles de tourbillons

On présente ici les différents modèles de tourbillons qui sont utilisés dans cette étude.

1.2.1 Le tourbillon de Rankine

Le tourbillon de Rankine est le modèle le plus simple faisant intervenir un cœur de vorticité de dimension finie. Il est constitué d'un tube de rayon a de vorticité constante. Son profil de vorticité ζ, est simplement décrit par la loi

$$\zeta(r) = \begin{cases} \frac{\Gamma}{\pi a^2} & r < a \\ 0 & r > a \end{cases} \tag{1.1}$$

où Γ est la circulation totale du tourbillon. Son profil de vitesse azimutale U_θ, illustré par la figure 1.2(b), suit la relation

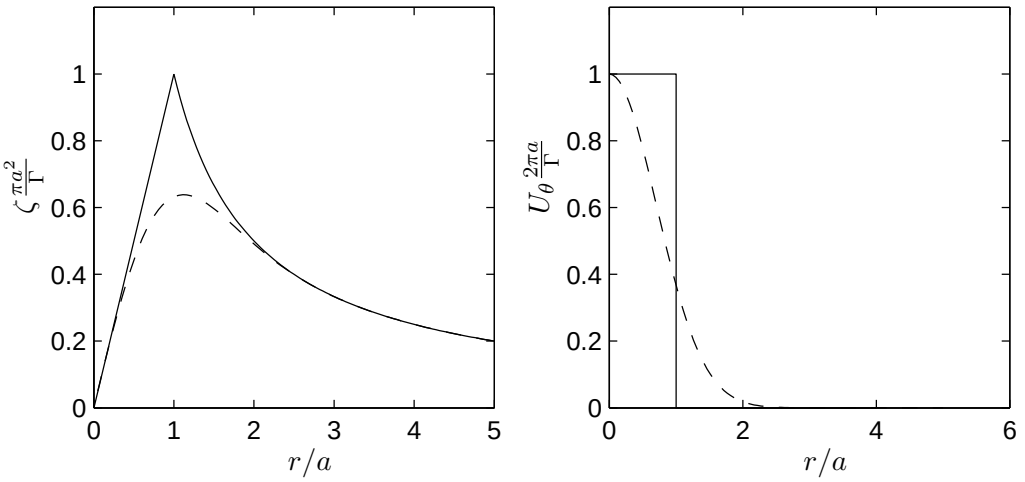

(a) (b)

FIG. 1.2 – (a) Le trait continu correspond au tourbillon de Rankine, le trait discontinu au tourbillon gaussien. (b) Profils de vitesse azimutale.

$$U_\theta(r) = \begin{cases} \frac{\Gamma}{2\pi a^2} r & r < a \\ \frac{\Gamma}{\pi a^2} \frac{1}{r} & r > a \end{cases} . \tag{1.2}$$

De nombreuses études théoriques utilisent ce tourbillon en tirant profit de la simplicité de ce modèle pour expliquer des phénomènes mettant en jeu la notion de cœur de taille finie. Ce modèle est cependant peu réaliste de part la discontinuité de son profil de vorticité qui le rend incompatible avec l'existence de viscosité.

1.2.2 Le tourbillon de Lamb–Oseen

Le tourbillon de Lamb–Oseen qui se caractérise par un profil de vorticité gaussien, est un modèle de tourbillon plus réaliste. Il est solution des équations d'Euler. Ses profils de vorticité et de vitesse azimutale sont décrits par les lois suivantes :

$$\zeta(r) = \frac{\Gamma}{\pi a^2} \exp(r^2/a^2), \tag{1.3a}$$

$$U_\theta(r) = \frac{\Gamma}{2\pi r}(1 - \exp(r^2/a^2). \tag{1.3b}$$

On peut montrer que la vitesse azimutale est maximale pour $r \approx 1.12a$. Ce modèle est utile également dans le domaine visqueux : en effet, si l'on rajoute la condition de diffusion visqueuse du rayon de vorticité selon la relation $a^2(t) = 4\nu t$, où ν est la viscosité cinématique du fluide, alors ce modèle est une solution autosimilaire des équations de Navier–Stokes bidimensionnelles. Cette propriété justifie l'utilisation de ce modèle dans de très nombreuses études.

1.2.3 Le modèle VM2

Un autre tourbillon, récemment proposé par Fabre (Fabre *et al.*, 2002; Fabre & Jacquin, 2004*a*) sous le nom de VM2, convient tout particulièrement aux tour-

billons de sillage. Il est caractérisé par deux échelles (rayons) caractéristiques a_1 et a_2. a_1 délimite le noyau visqueux contenant la majorité de la vorticité et a_2 définit la région contenant toute la circulation. Il dispose également d'un autre paramètre, α, caractérisant la loi de décroissance de la vitesse azimutale pour $a_1 < r < a_2$. Le modèle VM2 est défini par :

$$U_\theta(r) = \frac{\Gamma}{2\pi}\frac{a_2^{\alpha-1}}{a_1^{\alpha+1}}\frac{r}{[1+(1/a_1)^4]^{(1+\alpha)/4}\,[1+(1/a_2)^4]^{(1-\alpha)/4}} \tag{1.4}$$

Au cours de cette étude, on utilisera le VM2 pour modéliser le profil de vitesse azimutale d'un tourbillon de bout d'aile.

1.2.4 Le tourbillon de Batchelor

Ce modèle est l'extension tridimensionnelle du tourbillon bidimensionnel de Lamb–Oseen. Les profils de vitesse et de vorticité axiales sont modélisés par des fonctions gaussiennes. C'est en fait une approximation du modèle défini par Batchelor (1964) pour décrire le développement des tourbillons présents dans le sillage lointain des avions. On reprend ici cette terminologie courante dans la littérature. Le tourbillon de Batchelor est un des modèles réaliste les plus simples pour représenter un tourbillon avec écoulement axial. Il a été l'objet de nombreuses études théoriques et numériques. Lorsque les profils de vorticité s'y prêtent, il est alors pratique d'utiliser ce modèle pour pouvoir comparer, qualitativement et quantitativement, des résultats expérimentaux à des prédictions concernant le même écoulement. C'est ce qui a été fait au cours de cette étude.

1.3 Paramètres des écoulements étudiés

Dans notre étude nous étudieront des écoulements mettant en jeu des tourbillons avec écoulement axial. On pourra caractériser chaque vortex par un nombre de Reynolds

$$\Gamma/\nu, \tag{1.5}$$

où Γ est la ciculation totale du tourbillon et ν est la viscosité cinématique du fluide.

Pour estimer l'écoulement axial par rapport à une vitesse caractéristique de rotation du tourbillon, on utilisera le nombre adimensionné

$$W_0 = (U_0 - U_\infty)\frac{2\pi a}{\Gamma}, \tag{1.6}$$

où U_0 est la vitesse axiale au centre du tourbillon et U_∞ est la vitesse axiale loin du cœur tourbillon. a est le rayon de vorticité caractéristique. Au cours de notre étude, on aura toujours $|W_0| < 0.6$. Dans ce cas, le tourbillon de Batchelor est considéré stable. Il existe des modes de cœur instables mais leur taux de croissance est si faible Fabre & Jacquin (2004*b*) qu'il ne sont jamais dominant devant l'instabilité elliptique.

On comparera la taille caractéristique du cœur de vitesse axiale a_W et le rayon de vorticité a en utilisant le ratio

$$a_W/a. \tag{1.7}$$

Une grande partie de notre étude traitera des paires de vortex co-rotatifs ou contra–rotatifs. On quantifiera dans ce cas l'interaction entre les deux tourbillons écartés de b par le paramètre

$$a/b. \tag{1.8}$$

Pour une paire de tourbillons co-rotatifs, on restera dans tous les cas en amont de la fusion. On aura toujours $a/b < 0.25$, qui correspond au seuil (critère de fusion) au dessus duquel le processus de fusion de deux tourbillons gaussiens commence (Meunier, 2001).

1.4 L'instabilité de Crow

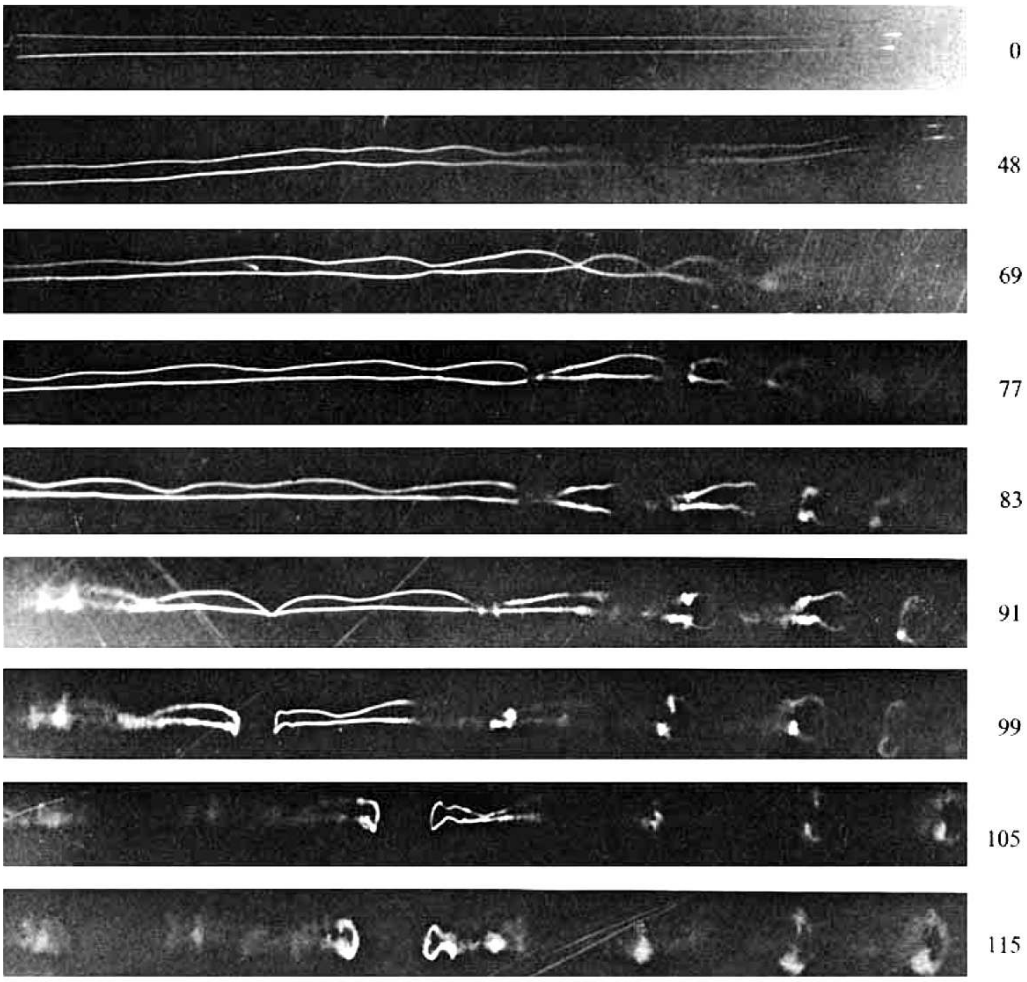

FIG. 1.3 – Série de photographies montrant l'évolution temporelle du sillage d'un avion Comet. Le temps est indiqué en secondes. (d'après Scorer & Davenport, 1970).

La première instabilité qui fut découverte dans une paire de tourbillons est celle que l'on appelle l'instabilité de Crow. Elle s'observe sur une paire de tourbillons contra–rotatifs. Elle consiste en une longue perturbation périodique, déplaçant les cœurs des deux tourbillons symétriquement. Elle peut être aperçue dans le sillage lointain des avions. Les photographies de Scorer & Davenport (1970) visibles dans la figure 1.3 (et notamment celle correspondant à $t = 69$ s) illustrent bien ce phénomène. Des visualisations en laboratoire sont présentées par Thomas & Auerbach (1994). La première analyse théorique de ce mécanisme a été réalisée par Crow (1970). Il a montré que l'induction mutuelle des deux tourbillons pouvait engendrer une instabilité dont la longueur d'onde équivalait à plusieurs distances de séparation des tourbillons. Les déplacements des cœurs sont sinusoïdaux et symétriques par rapport au plan médian entre les tourbillons. Cette instabilité est liée a un équilibre entre l'effet stabilisateur de la rotation auto–induite des perturbations et l'influence déstabilisatrice du champ d'étirement que chaque vortex induit à l'emplacement du second. Les oscillations restent dans des plans inclinés approximativement à 45° par rapport à la ligne joignant la position moyenne des deux tourbillons. Kelvin (1880) a montré qu'une perturbation sinusoïdale d'un filament de vorticité isolé ne croît pas dans le temps mais tourne autour du vortex. En présence d'un second vortex, la composante azimutale du champ de vitesse induit par ce vortex à l'emplacement du premier, annule exactement la rotation auto-induite de ce dernier. La composante radiale du champ d'étirement va alors étirer la perturbation qui reste dans le plan. Jimenez (1975) a montré que la rotation du champ d'étirement rendait ce mécanisme impossible, empêchant l'instabilité de Crow de se propager sur une paire de tourbillon co-rotatifs. Les travaux de Moore & Saffman (1973) et Klein, Majda & Damodaran (1995) ont ensuite étendu les travaux de Crow en étudiant l'influence d'un écoulement axial et d'une distribution de vorticité aléatoire sur l'instabilité. L'analyse de Crow a aussi été reprise dans le cas de systèmes de plus de deux vortex, plus représentatifs du sillage proche d'un avion (Crouch & Jacquin, 2005). Les travaux numériques de Rennich & Lele (1997) confirment les travaux de Crow, mais les différentes études expérimentales sur le sujet ne proposent pas de comparaison quantitative précise avec la théorie en place. Au cours de cette étude, on se propose de comparer la longueur d'onde et le taux de croissance observés expérimentalement sur une paire de tourbillons contra–rotatifs avec écoulement axial, avec les prédictions concernant l'instabilité de Crow.

1.5 L'instabilité elliptique

Si l'instabilité de Crow met en jeux des longueurs d'onde permettant de négliger la taille du cœur du tourbillon lors de l'analyse théorique, il n'en est pas de même pour l'instabilité elliptique. Ce phénomène, que l'on observe sur un tourbillon sujet à un étirement, se caractérise par une longueur d'onde du même ordre de grandeur que le diamètre du cœur du tourbillon. On parle d'instabilité à petite longueur d'onde. On qualifie cette instabilité d'"elliptique" car elle se propage sur un tourbillon déformé elliptiquement. Contrairement à l'instabilité de Crow, l'instabilité elliptique peut aussi bien être observée sur une paire de tourbillons contra–rotatifs que co–rotatifs.

Une manière d'aborder l'instabilité elliptique est de considérer un tourbillon immergé dans un champ d'étirement. Il prend alors une forme elliptique. On peut écrire le champ des perturbations sous la forme de mode normaux linéaires. En suivant cette formulation, les champs des perturbations de vitesse et de pression $\mathbf{u}'$ et p' s'écrivent

$$(\mathbf{u}', p') = [\mathbf{u}(r), p(r)] \exp(ikz + im\theta - i\omega t), \tag{1.9}$$

où k est le nombre d'onde axial, m le nombre d'onde azimutal et ω la fréquence (pulsation). Superposés à un tourbillon de Rankine, les modes normaux linéaires qui sont solutions de la relation de dispersion $D(k, m, \omega) = 0$ sont appelés "modes de Kelvin". Kelvin, dès 1880, fut le premier à introduire ce formalisme pour étudier la stabilité linéaire du tourbillon de Rankine. Pour chaque nombre d'onde azimutal m, il existe une infinité de branche dans le plan (k, ω), qui sont solutions de la relation de dispersion. Pour classer ces branches, on utilise le label n qui correspond au nombre de zéros de $u(r)$. Arendt, Fritts & Andreassen (1997) ont montré que les modes de Kelvin ainsi définis forment une base des perturbations localisées au cœur du tourbillon. On peut donc exprimer toutes les perturbations au cœur du vortex par une combinaison linéaire de modes de Kelvin. On voit bien, ici, tout l'intérêt d'utiliser une telle base pour l'analyse de stabilité d'un tourbillon.

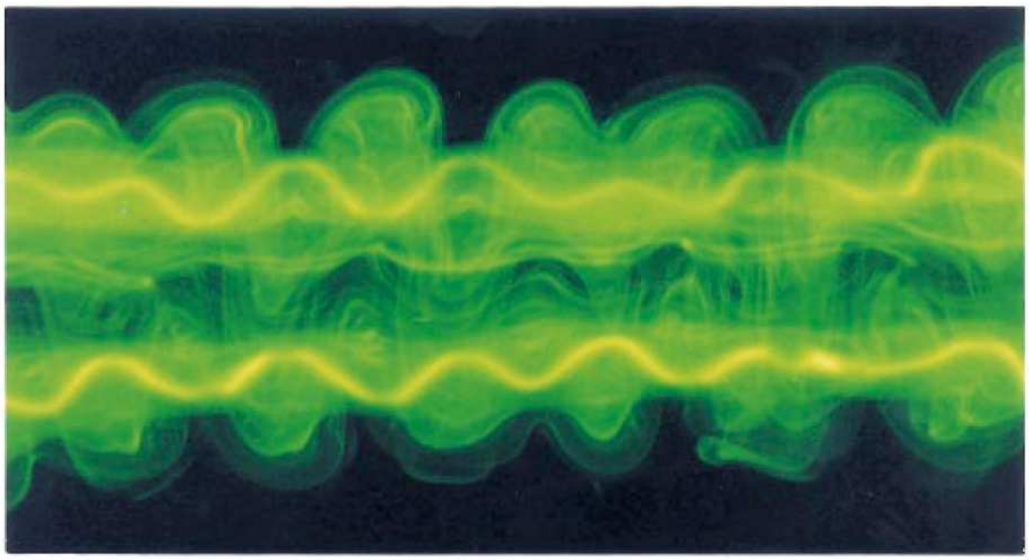

FIG. 1.4 – Visualisation de l'instabilité elliptique sur une paire de tourbillons contra–rotatifs (d'après Leweke & Williamson, 1998).

C'est la méthode qu'empruntèrent Moore & Saffman (1975) et Tsai & Widnall (1976) pour mettre à jour le mécanisme de l'instabilité elliptique. En étudiant un patch de vorticité dans un champ d'étirement, ils montrèrent que le champ d'étirement pouvait résonner avec deux ondes de Kelvin de nombres d'onde axiaux égaux, de fréquences nulles, et de nombres d'onde azimutaux respectifs $m_1 = 1$ et $m_2 = -1$. Les conditions de résonances ont plus tard été généralisées à des nombres d'ondes azimutaux plus élevés (Eloy & Le Dizès, 2001). Elles relient le champ d'étirement aux deux modes de Kelvin de nombres d'onde respectifs

k_1, m_1, ω_1 et k_2, m_2, ω_2 qui doivent vérifier :

$$\begin{pmatrix} k_1 \\ m_1 \\ \omega_1 \end{pmatrix} - \begin{pmatrix} k_2 \\ m_2 \\ \omega_2 \end{pmatrix} = \begin{pmatrix} 0 \\ 2 \\ 0 \end{pmatrix}. \tag{1.10}$$

Deux ondes de Kelvin vont alors pouvoir résonner avec le champ d'étirement si leur nombres d'onde axiaux et leur fréquences sont égaux, et si leurs nombres d'onde azimutaux diffèrent de 2. Eloy & Le Dizès (2001) ont montré que, pour un tourbillon de Rankine, le taux de croissance est maximisé quand les labels n des deux ondes de Kelvin sont égaux. Dans ce cas, le mode est appelé "principal" et on peut l'identifier par le triplet $(-1, 1, n)$. On reprendra la même convention généralisée (m_1, m_2, n) pour décrire tous les modes principaux.

Les conditions 1.10 sont obtenues pour un champ d'étirement stationnaire. En pratique, elles sont donc utilisables dans le cas d'une paire de tourbillons contra-rotatifs. Pour traiter la paire de tourbillons co-rotatifs, il faut tenir compte de la rotation du champ d'étirement au taux Ω. Les conditions de résonance 1.10 deviennent alors :

$$\begin{pmatrix} k_1 \\ m_1 \\ \omega_1 \end{pmatrix} - \begin{pmatrix} k_2 \\ m_2 \\ \omega_2 \end{pmatrix} = \begin{pmatrix} 0 \\ 2 \\ \Omega \end{pmatrix}. \tag{1.11}$$

Par ailleurs, Pierrehumbert (1986) et Bayly (1986) montrèrent qu'un écoulement bidimensionnel, non–visqueux, et dont les lignes de courant sont elliptiques, est instable relativement à des perturbations tridimensionnelles, dans la limite des petites longueurs d'onde. Waleffe (1990) raccorda cette théorie locale à la théorie globale liées aux modes de Kelvin. L'instabilité elliptique peut ainsi être décrite par ces deux approches.

Jusqu'ici, les résultats expérimentaux étaient surtout qualitatif. Leweke & Williamson (1998) étudièrent expérimentalement une paire de vortex contra–rotatifs et montrèrent que la longueur d'onde et le taux de croissance de l'instabilité observée (voir figure 1.4) correspondait aux prédictions de Tsai & Widnall (1976) et Waleffe (1990). La même conclusion fut tirée par Meunier & Leweke (2005) pour le cas d'une paire de tourbillons co-rotatifs.

De manière à étendre les résultats théoriques existant en caractérisant l'instabilité elliptique dans un tourbillon de profil de vorticité continu réaliste, Le Dizès & Laporte (2002) étudièrent des paires de tourbillons contra–rotatifs gaussiens. Ils trouvèrent une expression du taux de croissance de l'instabilité elliptique en fonction des paramètres globaux de l'écoulement. D'autres études, comme par exemple celle de Fabre & Jacquin (2004*a*), caractérisent l'instabilité elliptique dans des tourbillons plus représentatifs des sillages des avions.

La prochaine étape majeure dans l'étude de l'instabilité elliptique fut l'ajout d'un écoulement axial. Notamment, Lacaze, Birbaud & Le Dizès (2005*a*) étudièrent un tourbillon de Rankine plongé dans un champ d'étirement stationnaire auquel ils ajoutèrent un noyau de vitesse axiale. Contrairement au cas sans écoulement axial, ils trouvèrent que des modes de Kelvin avec une complexité azimutale élevée et une fréquence non nulle peuvent résonner avec le champ d'étirement, donnant lieu à une instabilité du système. Les mêmes conclusions

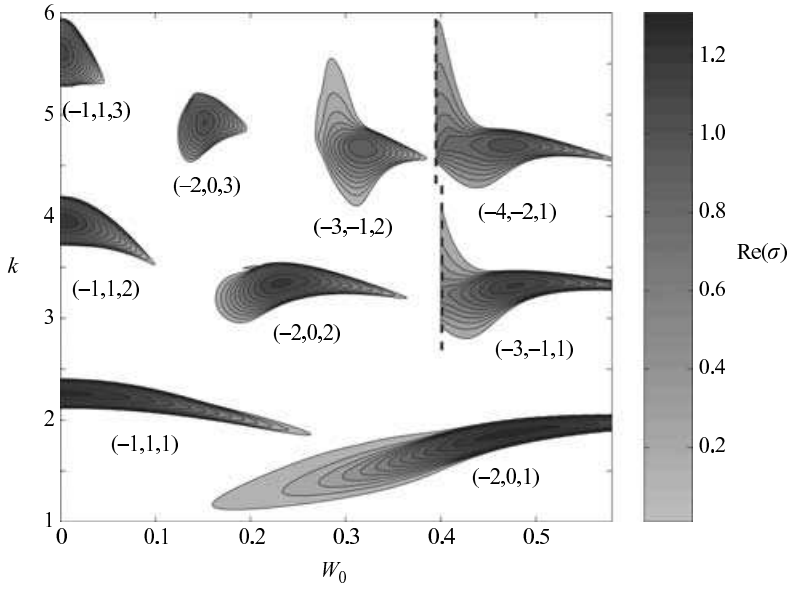

FIG. 1.5 – Taux de croissance de l'instabilité elliptique dans une paire de tourbillons contra-rotatifs pour lesquels $[\Gamma|/2\pi\nu = 20000$ et $a^2/b^2 = 0.015$ (d'après Lacaze *et al.*, 2007).

furent tirées pour le tourbillon de Batchelor (Lacaze, Ryan & Le Dizès, 2007). La figure 1.5 présente les zones d'instabilités correspondant aux modes principaux les plus instables dans le plan (W_0, k). Une autre spécificité relevée par cette étude est que des modes de Kelvin de labels différents peuvent donner lieu à une instabilité dont le taux de croissance sera le plus grand pour un couple (W_0, k) donné.

Afin d'étendre ces résultats, on réalisera, au cours de cette étude, une analyse numérique de stabilité linéaire d'une paire de tourbillons de Batchelor co-rotatifs. On présentera également une étude expérimentale identifiant un mode de l'instabilité elliptique avec $|m| = 2$ prédit par Lacaze *et al.* (2007).

1.6 Vortex meandering

Le terme *vortex meandering* (flottement d'un tourbillon) caractérise le mouvement cohérent à basse fréquence d'un tourbillon de bout d'aile généré dans un laboratoire (soufflerie, canal à eau). Il est aussi connu sous le nom de *wandering*. De nombreuses études y font référence. On peut citer par exemple Gasparek (1957), Corsiglia, Schwind & Chigier (1973) et Baker *et al.* (1974). La figure 1.6 montre une visualisation d'un tourbillon créé par une aile de profil NACA0018 placée dans l'écoulement libre d'une soufflerie. De part cette vue presque axiale, on distingue la longue oscillation axiale du tourbillon typique du vortex meandering.

Ce phénomène semble indissociable de la génération de tourbillons de sillage dans une soufflerie. Il est perçu comme un problème par les expérimentateurs désireux de caractériser précisément le champ moyen d'un écoulement tourbillonnaire créé dans ces conditions. De part le mouvement de translation qu'il impose au tourbillon, le champ des vitesses moyennées temporellement peut différer assez largement des champs de vitesse instantanés, suivant l'amplitude du meandering.

FIG. 1.6 – Visualisation d'un tourbillon de bout d'aile généré dans une soufflerie. $\Gamma/nu = 40000$.

Des études proposent des méthodes de correction du champ moyen pour retirer l'influence du meandering (Baker *et al.*, 1974; Devenport *et al.*, 1996). L'approche de Devenport *et al.* (1996) est basée sur l'hypothèse que la position du tourbillon suit une densité de probabilité gaussienne. C'est donc une méthode purement statistique. Ils rapportent une certaine corrélation entre le niveau de turbulence de la soufflerie et l'intensité du meandering.

À l'heure actuelle, le mécanisme responsable du meandering reste à identifier. Il existe cependant des éléments pouvant théoriquement l'expliquer. Jacquin *et al.* (2001, 2003) relevèrent la nature ondulatoire du meandering. Ils associèrent le phénomène à l'excitation des ondes de Kelvin avec un nombre d'onde azimutal $m = 1$ ("bending wave") par les turbulences de l'écoulement. Pour le tourbillon de Lamb–Oseen, Antkowiak & Brancher (2004) étudièrent la croissance transitoire de perturbations déclenchées par du bruit extérieur. Leur analyse des perturbations optimales montre que ce modèle de tourbillon permet une amplification des perturbations de nombre d'onde azimutal $m = 1$. Ce résultat fut étendu au tourbillon de Batchelor par Heaton (2006). Fontane *et al.* (2008) montra que les perturbations optimales trouvées par Antkowiak & Brancher (2004) peuvent être sélectionnées dans un bruit stochastique par le tourbillon de Lamb–Oseen. On peut donc supposer que dans une soufflerie, à partir de la turbulence de l'écoulement, un tourbillon extrait les perturbations engendrant un mouvement de translation du vortex au bout d'un temps fini.

Dans cette étude, on étudiera expérimentalement un tourbillon de bout d'aile généré dans un canal hydrodynamique. On tentera de relier nos observations au concept de croissance transitoire présenté par Antkowiak & Brancher (2004).

1.7 Plan de l'étude

Cette étude est divisée en deux parties : la première traite de l'étude numérique réalisée, la seconde regroupe les résultats expérimentaux obtenus.

Dans un premier temps, la méthode numérique, utilisée pour l'analyse de stabilité d'une paire de tourbillons co-rotatifs avec écoulement axial, est détaillée. On justifie également le choix des paramètres numériques utilisés pour l'étude.

Ensuite, on expose les résultats obtenus caractérisant l'instabilité elliptique dans une paire de tourbillons co-rotatifs avec écoulement axial. On identifie notament les modes de l'instabilité dont on calcule le taux de croissance. On discute ces résultats que l'on compare avec le cas d'une paire de tourbillons contra–rotatifs.

Après cela, on se consacre à mettre en évidence l'existence de l'instabilité elliptique sur des paires de tourbillons de bout d'aile, générés dans un canal hydrodynamique. On caractérise la strucutre spatiale de modes d'instabilité obtenus pour une paire de vortex co– et contra–rotatifs. Le cas contra–rotatif est analysé plus en détails en comparant nos mesures avec des résultats numériques obtenus par une analyse de stabilité effectuée sur l'écoulement expérimental.

La dernière partie de notre étude porte sur le meandering d'un tourbillon. On présente des données statistiques caractérisant le meandering d'un vortex généré dans un canal hydrodynamique au moyen d'une aile. On tente ensuite de donner des éléments permettant de relier nos observations au phénomène de croissance transitoire des perturbations sous forme d'une onde de nombre azimutal $m = 1$.

Première partie

Étude numérique d'une paire de tourbillons co–rotatifs avec écoulement axial

Chapitre 2

Méthode numérique

Dans ce chapitre, on montre les différentes étapes qui ont été suivies pour mener à l'analyse numérique de l'instabilité elliptique d'une paire de tourbillons co–rotatifs identiques, dont les profils de vorticité et de vitesse axiale sont gaussiens. On étudie la stabilité de ce champ de base bidimensionnel, relativement à des perturbations tridimensionnelles. Le code à éléments spectraux utilisé a été développé par Mark Thompson à Monash University. Il a déjà été employé avec succès dans de nombreux travaux et notamment ceux de Lacaze, Ryan & Le Dizès (2007) qui ont étudié la stabilité d'une paire de tourbillons identiques à ceux de cette étude mais dans le cas contra-rotatif. On s'attache ici à présenter la méthode numérique mise en œuvre et on justifie le choix des différents paramètres numériques.

2.1 Hypothèses de l'étude

De manière à pouvoir poser les équations utilisées lors des simulations numériques, il est nécessaire de définir les hypothèses de l'étude.
Au cours des simulations, le fluide étudié est supposé être un milieu continu. On peut ainsi considérer un élément de fluide infiniment petit pour former les équations différentielles. On reste ainsi dans une échelle macroscopique. Cela revient à faire l'hypothèse que l'échelle de longueur moléculaire est négligeable devant les échelles de longueur caractéristiques de l'écoulement et des phénomènes étudiés.
Ensuite, on suppose que le fluide est incompressible, c'est à dire que la densité d'un élément de fluide n'est pas affectée par des variations de pression. On évite ainsi tout problème dû à la propagation des ondes acoustiques. Notre étude est donc subsonique.
De plus, le fluide est supposé Newtonien. Cela signifie que le rapport de la contrainte de cisaillement sur le taux d'étirement est constant et définit alors la viscosité dynamique. C'est notamment le cas des gaz et des liquides de faible masse molaire. Ces hypothèses sont classiques et ont été utilisées dans de nombreuses simulations numériques mettant en jeu des tourbillons. On peut citer, par exemple, les travaux de Parras & Fernandez-Feria (2007), Schmid & Rossi (2004) et Delbende, Chomaz & Huerre (1998).

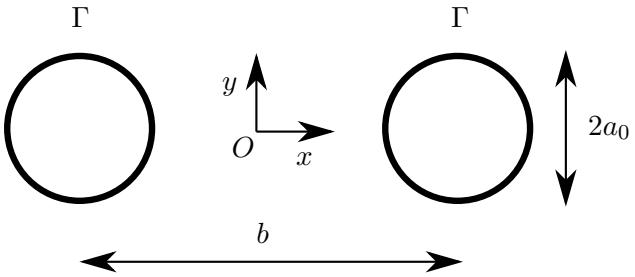

FIG. 2.1 – Définition du repère cartésien. Les vortex sont situés sur l'axe Ox en $x_{c1} = -b/2$ et $x_{c2} = b/2$.

2.2 Conditions initiales

Notre étude consiste à analyser la stabilité d'une paire de vortex identiques co-rotatifs. Afin d'obtenir l'écoulement de base étudié, deux vortex axisymétriques sont placés côte à côte à la distance b l'un de l'autre. Leurs profils de vorticité ω et de vitesse axiale W sont gaussiens. Dans le repère cylindrique centré sur chaque vortex, les profils s'écrivent

$$\omega(r) = \frac{\Gamma}{\pi a_0^2} e^{-r^2/a_0^2} \tag{2.1}$$

et

$$W(r) = K\frac{\Gamma}{\pi a_0^2} e^{-r^2/a_0^2}. \tag{2.2}$$

Le paramètre a_0 définit un rayon du vortex ; c'est la valeur du rayon à l'instant initial de la simulation (voir chapitre 2.3.5 pour la définition du rayon du vortex à un temps quelconque). La vitesse axiale est choisie proportionnelle à la vorticité d'un facteur K. Par la suite, elle pourra se déduire directement du champ de vitesse dimensionnelle. Dans le repère cartésien fixe centré sur le vortex, le champ des vitesses $\big[U_v(x,y), V_v(x,y), W_v(x,y)\big]$, à l'instant $t = 0$, est alors de la forme

$$U_v = -\frac{\Gamma y}{2\pi(x^2+y^2)}\left(1 - e^{-(x^2+y^2)/a_0^2}\right), \tag{2.3a}$$

$$V_v = \frac{\Gamma x}{2\pi(x^2+y^2)}\left(1 - e^{-(x^2+y^2)/a_0^2}\right), \tag{2.3b}$$

$$W_v = K\frac{\Gamma}{\pi a_0^2} e^{-\left(x^2+y^2\right)/a_0^2}. \tag{2.3c}$$

On se place maintenant dans le repère cartésien fixe, centré sur le milieu O du segment reliant le centre des deux vortex à $t = 0$, défini dans la figure 2.1. Les tourbillons étant identiques, O est alors le centre de vorticité du système.[1] À $t = 0$, le champ des vitesses $\big[U_{cart}(x,y), V_{cart}(x,y), W_{cart}(x,y)\big]$ de la somme de deux vortex de circulation Γ et de rayon a_0, placés à la distance b l'un de l'autre à s'écrit alors

[1] On définit le centre de vorticité en calculant le premier moment de la vorticité (centre de masse pondéré par la vorticité).

$$U_{cart} = -\frac{\Gamma}{2\pi}\left[\frac{y}{x_1^2+y^2}\left(1-e^{-\left(x_1^2+y^2\right)/a_0^2}\right)+\frac{y}{x_2^2+y^2}\left(1-e^{-\left(x_2^2+y^2\right)/a_0^2}\right)\right], \tag{2.4a}$$

$$V_{cart} = \frac{\Gamma}{2\pi}\left[\frac{x_1}{x_1^2+y^2}\left(1-e^{-\left(x_1^2+y^2\right)/a_0^2}\right)+\frac{x_2}{x_2^2+y^2}\left(1-e^{-\left(x_2^2+y^2\right)/a_0^2}\right)\right], \tag{2.4b}$$

$$W_{cart} = K\frac{\Gamma}{\pi a_0^2}\left[e^{-\left(x_1^2+y^2\right)/a_0^2}+e^{-\left(x_2^2+y^2\right)/a_0^2}\right], \tag{2.4c}$$

où

$$x_1 = x - b/2, \tag{2.5}$$

$$x_2 = x + b/2. \tag{2.6}$$

Dans le cas d'un système de vortex co-rotatifs de même circulation, on peut montrer que la vitesse induite par chaque tourbillon sur le voisin est telle que dans le repère fixe, le système tourbillonnaire tourne autour du point O à la vitesse Ω telle que

$$\Omega = \frac{\Gamma}{\pi b^2}\left(1-e^{-b^2/a_0^2}\right) \approx \frac{\Gamma}{\pi b^2}. \tag{2.7}$$

Typiquement, pour $a_0/b = 0.15$, on a $exp(-b^2/a_0^2) \approx 10^{-20}$. Pour les valeurs de a_0/b de notre étude, le terme exponentiel de l'équation (2.7) est donc aisément négligeable.

En imposant au repère illustré par la figure 2.1 un mouvement de rotation autour de O à la vitesse angulaire Ω, on définit ce que l'on appelle communément le repère tournant. Pour des temps faibles comparés au temps caractéristique de diffusion visqueuse, ce repère présente l'avantage de maintenir le centre des tourbillons dans la même position au cours du temps, si le système suit les équations (2.9) et (2.10) présentées plus bas. On saura tirer profit de cette caractéristique par la suite. Dans le repère tournant, le champ des vitesses $\mathbf{U} = \big[(U(t=0), V(t=0), W(t=0)\big]$ s'exprime alors

$$U(t=0) = U_{cart} - \Omega y, \tag{2.8a}$$

$$V(t=0) = V_{cart} + \Omega x, \tag{2.8b}$$

$$W(t=0) = W_{cart}. \tag{2.8c}$$

Ce champ constitue la condition initiale de la phase de génération de l'écoulement de base dans le repère tournant. Il est illustré par la figure 2.2.

2.3 Génération de l'écoulement de base

2.3.1 Équations régissant l'écoulement

Une fois le problème initialisé et les hypothèses de travail clairement définies, il est maintenant possible de poser les équations régissant le système. Dans le

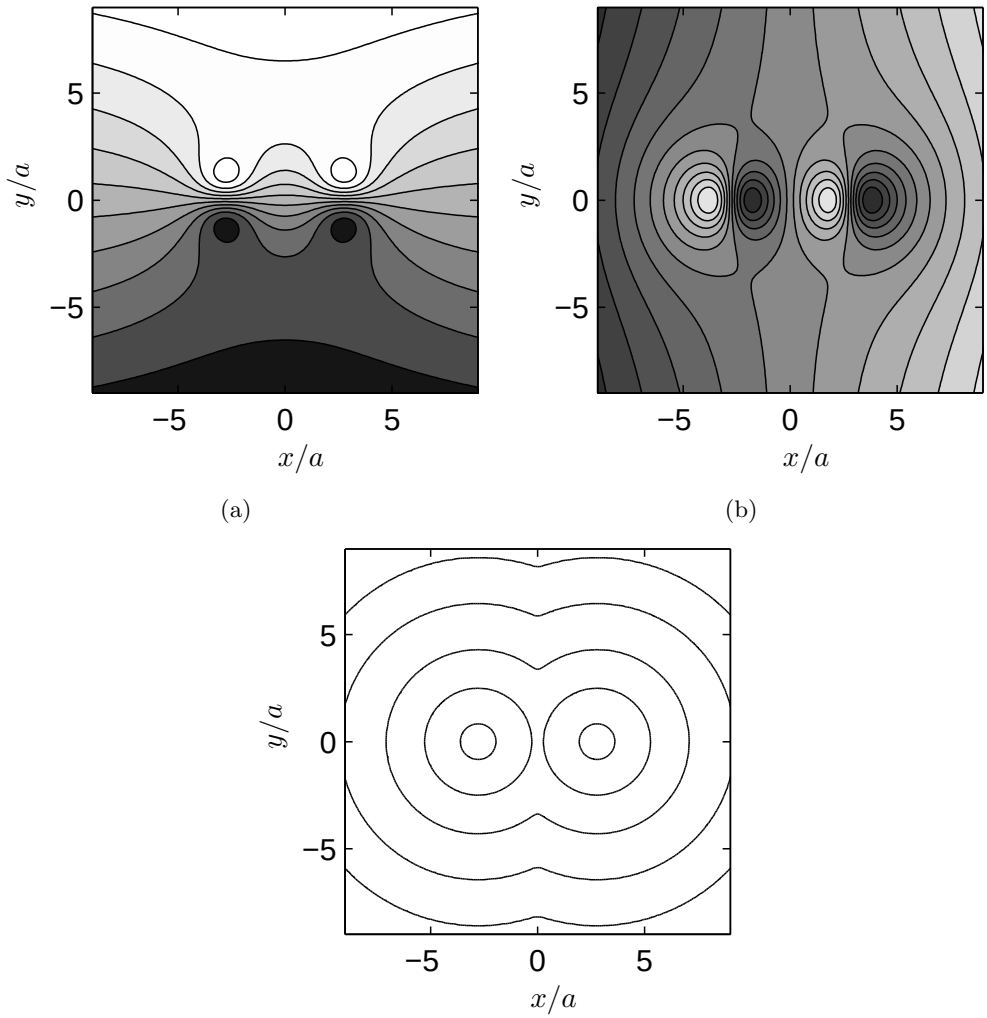

FIG. 2.2 – (a) et (b) : champs des vitesses $U(t=0)b\pi/2\Gamma$ et $V(t=0)b\pi/2\Gamma$ utilisés lors de l'initialisation des simulations numériques pour $a/b = 0.18$ dans le repère tournant. Les niveaux de couleur sont linéaires et varient de -1 à 1 du noir au blanc. (c) : champ de vorticité à $t = 0$. La vorticité est adimensionnée par $\Gamma/\pi a^2$. Les niveaux représentés correspondent à 10^{-32}, 10^{-18}, 10^{-8}, 0.002 et 0.5, de l'extérieur du domaine vers l'intérieur. On rappelle que la vitesse axiale $W(t=0)$ est choisie proportionnelle à la vorticité axiale.

repère tournant, les équations de Navier–Stokes régissant l'écoulement d'un fluide incompressible s'écrivent

$$\frac{\partial \mathbf{U}}{\partial t} = -\left(\mathbf{U}\cdot\nabla\right)\mathbf{U} - \frac{\nabla P}{\rho} + \nu\nabla^2\mathbf{U} - \mathbf{2\Omega}\times\mathbf{U}. \tag{2.9}$$

Le terme correspondant à la force centrifuge est écrit sous forme d'un gradient et est inclus dans le potentiel P avec la pression. Il convient également de rajouter l'équation de continuité

$$\nabla \cdot \mathbf{U} = \mathbf{0}. \tag{2.10}$$

Dans la partie de droite de l'équation (2.9), le premier terme représente les forces d'inertie. Le terme $-2\boldsymbol{\Omega} \times \mathbf{U}$ est l'opérateur de Coriolis et est nécessaire pour travailler dans le repère tournant. Les autres termes sont les forces de pression et de viscosité. L'équation (2.10) découle de l'hypothèse d'incompressibilité et de l'équation de conservation de la masse. Elle annonce que dans un élément de fluide, les débits d'entrée et de sortie sont égaux.

2.3.2 Time splitting

Il existe de nombreuses techniques pour intégrer temporellement le système d'équations présenté en 2.3.1. La méthode de time-splitting qui a été utilisée pour nos simulations a été développée par Karniadakis, Israeli & Orszag (1991). Elle utilise des conditions aux limites sur la pression réduisant l'erreur de divergence aux limites à $O\left(\Delta t/Re\right)^J$ où J est l'ordre du schéma d'intégration temporelle utilisé. En pratique, les conditions aux limites sur la pression sont du premier ordre, ce qui renforce la stabilité du système. La méthode consiste à diviser en plusieurs étapes l'intégration des termes du membre de droite de l'équation (2.9). Une fois réalisée, cette étape aboutit à une intégration temporelle d'un pas de temps Δt. On intègre en premier le terme non-linéaire (terme convectif) dans lequel on inclut l'opérateur de Coriolis. Le résultat de cette opération fournit une première estimation du champ de vitesse final. En partant de cette valeur de départ, on procède ensuite à l'intégration du terme de pression. Avec cette deuxième valeur, on peut finalement intégrer la partie linéaire de l'équation (2.9) (à savoir le terme de diffusion visqueuse) pour obtenir la valeur du champ de vitesse un pas de temps plus tard. Cette méthode a été décrite dans les travaux de thèse de Sheard (2004), Ryan (2004) et Leontini (2007).

On peut résumer le processus de time-splitting par les équations

$$\mathbf{U}_1 = \mathbf{U}^{(n_t)} - \int_t^{t+\Delta t} \left[(\mathbf{U}.\nabla)\mathbf{U} + 2\boldsymbol{\Omega} \times \mathbf{U}\right] dt, \tag{2.11a}$$

$$\mathbf{U}_2 = \mathbf{U}_1 - \int_t^{t+\Delta t} \nabla P dt, \tag{2.11b}$$

$$\mathbf{U}^{(n_t+1)} = \mathbf{U}_2 + \int_t^{t+\Delta t} \nu \nabla^2 \mathbf{U} dt. \tag{2.11c}$$

Dans les équations (2.11), Δt est le pas de temps, n_t est le nombre de pas de temps précédemment intégrés, $\mathbf{U}^{(n_t)}$ et $\mathbf{U}^{(\mathbf{n_t+1})}$ sont les champs des vitesses à l'instant t et $t + \Delta t$, et $\mathbf{U}_1$ et $\mathbf{U}_2$ sont les champs des vitesses calculés aux étapes d'intégration intermédiaires. On posera par la suite

$$\mathscr{N}(\mathbf{U}) = -(\mathbf{U}.\nabla)\mathbf{U} - 2\boldsymbol{\Omega} \times \mathbf{U}, \tag{2.12a}$$

$$\mathscr{L}(\mathbf{U}) = \nu \nabla^2 \mathbf{U}. \tag{2.12b}$$

Intégration du terme de convection

Afin d'intégrer le terme non-linéaire $\mathscr{N}$ défini par (2.12a), une méthode bien connue de Adams-Bashforth (Bashforth & Adams, 1883) à l'ordre 3 a été utilisée afin d'obtenir une haute précision temporelle tout en autorisant l'utilisation d'un pas de temps raisonnablement élevé. À cause de la nature non-linéaire de ce terme, une méthode explicite était nécessaire, ce qui implique en outre le contrôle du pas de temps par une condition de Courant (Canuto, 1988). Le calcul de $\mathbf{U}_1$ s'effectue finalement en suivant l'équation

$$\mathbf{U}_1 = \mathbf{U}^{(n_t)} + \frac{\Delta t}{12}\left[23\mathscr{N}\left(\mathbf{U}^{(n_t)}\right) - 16\mathscr{N}\left(\mathbf{U}^{(n_t-1)}\right) + 5\mathscr{N}\left(\mathbf{U}^{(n_t-2)}\right)\right]. \quad (2.13)$$

Cette intégration est pratiquée sur tout le domaine sans imposer de conditions aux limites sur les nœuds de la périphérie (Canuto, 1988).

Intégration du terme de pression

Pour intégrer le terme de pression de l'équation (2.9), on utilise la méthode de Adams-Moulton (Moulton, 1926) au second ordre. Cela se traduit par l'équation

$$\mathbf{U}_2 = \mathbf{U}_1 - \frac{\Delta t}{2\rho}\left(\nabla P^{(n_t+1)} + \nabla P^{(n_t)}\right). \quad (2.14)$$

En considérant que

$$\frac{1}{2}\left(\nabla P^{(n_t+1)} + \nabla P^{(n_t)}\right) = \nabla P^{(n_t+1/2)}, \quad (2.15)$$

en prenant la divergence de l'équation (2.11b) et en utilisant l'équation (2.10), on obtient une équation de Poisson qui s'écrit

$$\nabla^2 P^{(n_t+1/2)} = \frac{\rho}{\Delta t}\nabla \cdot \mathbf{U}_1. \quad (2.16)$$

On peut résoudre l'équation (2.16) pour trouver $\nabla^2 P^{(n_t+1/2)}$. En utilisant ensuite (2.14) et (2.15), on peut finalement obtenir une valeur pour $\mathbf{U}_2$.

Pour assurer la continuité à la frontière, Karniadakis *et al.* (1991) proposèrent d'imposer les conditions aux limites sur la dérivée de la pression (conditions de Neumann)

$$\frac{\partial P^{(n_t+1/2)}}{\partial \mathbf{n}} = \frac{\rho}{2}\mathbf{n} \cdot \left[\mathscr{N}\left(\mathbf{U}^{n_t}\right) - \nu\nabla \times \left(\nabla \times \mathbf{U}^{n_t}\right) - 2\boldsymbol{\Omega} \times \mathbf{U}^{\mathbf{n_t}}\right], \quad (2.17)$$

où $\mathbf{n}$ est le vecteur unitaire normal à la frontière du domaine. Cette équation est obtenue en sommant une estimation au premier ordre en temps des termes des équations (2.11), résultant en une forme discrétisée des équations de Navier–Stokes. On applique ensuite à chacun des membres de l'équation obtenue, le produit scalaire avec le vecteur normal $\mathbf{n}$. En utilisant l'écoulement de l'itération précédente, on impose ainsi des conditions sur la dérivée de la pression dans la direction normale à la frontière. Une fois la pression obtenue, la vitesse est évaluée par l'équation (2.14).

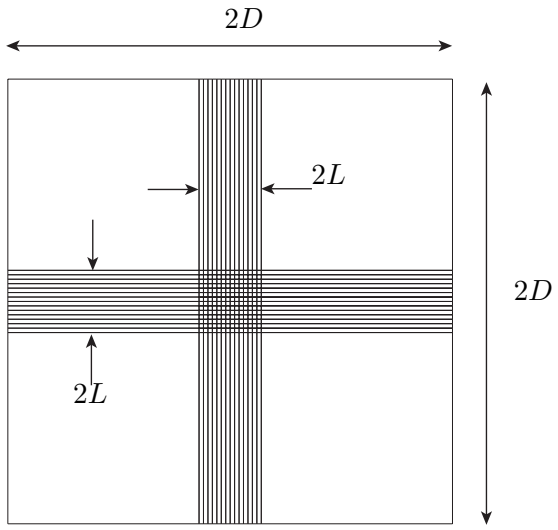

FIG. 2.3 – Maillage utilisé pour la génération de l'écoulement de base. Il est composé d'un domaine intérieur carré de côté $2L$ et d'un domaine extérieur carré de côté $2D$.

Intégration du terme linéaire

Il convient maintenant d'intégrer le terme linéaire de l'équation (2.9) pour tenir compte de la diffusion visqueuse dans le calcul du champ des vitesses. On utilise pour cela la technique de Crank-Nicolson (Crank & Nicolson, 1947) qui est en fait une méthode de Adams-Moulton résolue implicitement à l'ordre 2. L'utilisation de ce schéma est justifié par sa stabilité numérique inconditionnelle. L'équation (2.11c) devient alors

$$\mathbf{U}^{(n_t+1)} = \mathbf{U}_2 + \frac{\Delta t}{2}\left[\mathscr{L}\left(\mathbf{U}^{(n_t+1)}\right) + \mathscr{L}\left(\mathbf{U}^{(n_t)}\right)\right]. \tag{2.18}$$

Après simplification, l'équation (2.18) conduit à une équation de Helmholtz de laquelle on peut extraire $\mathbf{U}^{(n_t+1)}$. Comme on a utilisé l'équation de continuité lors de l'intégration du terme de pression, $\mathbf{U}_2$ et par conséquent $\mathbf{U}^{n_t+1}$ suivent l'équation (2.10). C'est à cette étape que sont utilisées les conditions aux limites sur le champ de vitesse définies dans le chapitre 2.3.4.

2.3.3 Méthode de résolution par éléments spectraux

L'objectif de cette partie est de présenter la méthode de calcul utilisée pour résoudre les équations régissant l'écoulement dans l'ensemble du domaine numérique. Pour cela, la première chose à réaliser est la discrétisation du domaine.

Discrétisation de l'espace

L'espace est divisée en macro-éléments à l'intérieur desquels une solution continue est interpolée. Tous les maillages utilisés au cours de notre étude sont formés de macro-éléments quadrilatéraux. Dans les zones où les gradients des vitesses sont élevés, il peut être nécessaire d'augmenter la densité des macro-éléments

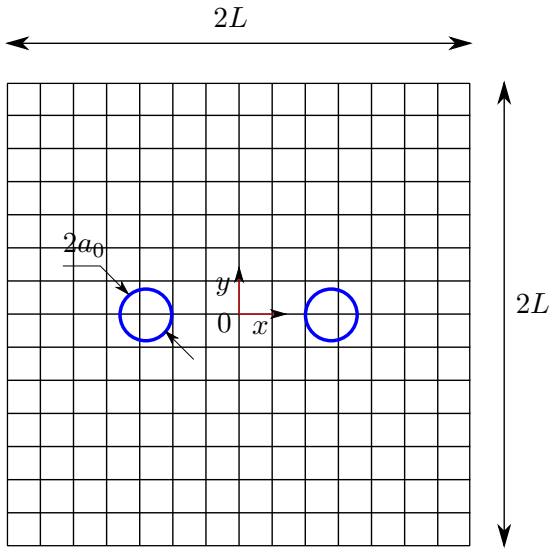

FIG. 2.4 – Zoom sur la partie intérieure du maillage. Le cercle bleu de rayon a_0 symbolise le vortex.

("raffinement-h").

La figure 2.3 présente le type de maillage utilisé pour la génération des écoulements de base. Il est constitué d'une zone centrale très dense dans laquelle sont placés les deux vortex. Les macro-éléments y sont carrés et de même dimension. En périphérie de cette zone ont été placés de gros macro-éléments rectangulaires. Leur rôle est d'écarter les frontières de la zone sensible de manière à diminuer l'influence des conditions aux limites. Cela est mis en place pour parer à un inconvénient de la méthode de résolution par éléments spectraux utilisée : la continuité des dérivées du champ de vitesse n'est pas assurée en chaque nœud. Il est donc possible que de la vorticité se décolle des frontières du domaine où l'erreur est maximale.

Une vue rapprochée de la zone à forte densité de nœuds est présentée figure 2.4. Les vortex sont symbolisés par deux cercles bleus de même rayon a_0 de manière à visualiser la taille relative des éléments par rapport aux vortex. Le maillage présenté figures 2.3 et 2.4 a également été utilisé dans la majeure partie des études de stabilité réalisées. Cependant, des cas problématiques ont nécessité une résolution plus élevée. Dans ce cas, le maillage illustré figure 2.5 a permis de concentrer les nœuds dans le voisinage d'un seul vortex. Ce maillage a été utilisé en interpolant en ses nœuds l'écoulement de base obtenu avec un maillage du type de la figure 2.3. Comme visualisé sur la figure 2.5, le vortex est centré sur la zone où la densité de nœuds est maximale. Les effets de l'instabilité elliptique étant localisés au cœur du vortex, les structures plus fines du champ des perturbations peuvent ainsi être résolues. Pour la validation du domaine numérique utilisé et une étude de convergence, on peut se référer à la partie 2.5. En particulier, le tableau 2.1 page 39 présente le nombre de points au cœur du vortex en fonction du maillage utilisé.

On se restreint maintenant à la résolution des équations dans un seul élément. Pour cela, on projette cet élément sur un carré de côté 2 centré en 0. On peut

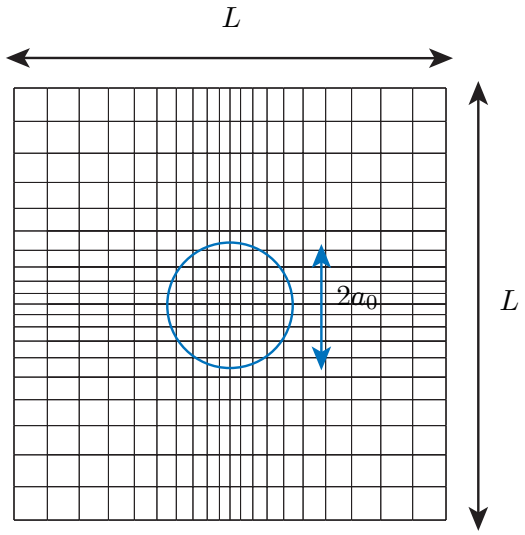

FIG. 2.5 – Maillage à résolution élevée utilisé pour l'analyse de stabilité. Il est composé d'un carré de côté L centré sur un vortex symbolisé par le cercle bleu de rayon a_0.

ainsi définir (ξ, η) comme un système de coordonnées orthonormales allant de -1 à 1 dans ce nouveau repère. Sur chacune des deux dimensions de l'élément, les $p+1$ points sont répartis de manière à respecter la quadrature de Gauss-Lobatto-Legendre. Karniadakis & Sherwin (1999) décrivent les points de la quadrature comme les solutions de l'équation

$$\begin{aligned} &(1-\xi^2)P_p'(\xi) = 0, \\ &\text{pour } -1 \leq \xi \leq 1, \end{aligned} \tag{2.19}$$

où les polynômes de Legendre P_p peuvent être décrits par la formule de Rodriguez (Kreiszig, 1993)

$$\begin{aligned} P_p = \frac{1}{2^p p!}\frac{\mathrm{d}^p}{\mathrm{d}\xi^p}\left(\xi^2-1\right)^p, \\ \text{pour } p = 0, 1, 2, \ldots. \end{aligned} \tag{2.20}$$

Les cœfficients de pondération Φ associés à ξ s'écrivent

$$\begin{aligned} \phi_i = \frac{2}{p(p+1)}\frac{1}{[P_p(\xi_i)]^2}, \\ \text{pour } i = 0, 1, \ldots, m-1, m. \end{aligned} \tag{2.21}$$

Les champs de vitesse et de pression seront interpolés en ces points. Le nombre de points interpolés par macro-élement est égal à $(p+1)^2$. En augmentant p, on augmente donc la résolution. On parle alors de "raffinement-p".

Résolution

Afin de résoudre les équations de Navier–Stokes (2.9), la méthode consiste à partir d'une solution test ($\mathbf{U}_{test}, P_{test}$) qui va servir de première estimation de la solution de l'équation (2.9). L'erreur induite par l'introduction de cette fonction est quantifiée par la relation

$$\mathbf{R} = \frac{\partial \mathbf{U}_{test}}{\partial t} + (\mathbf{U_{test}} \cdot \nabla)\, \mathbf{U_{test}} + \frac{\nabla P_{test}}{\rho} - \nu \nabla^2 \mathbf{U_{test}} + \mathbf{2\Omega} \times \mathbf{U_{test}}. \tag{2.22}$$

La prochaine étape consiste à pondérer le résidu $\mathbf{R}$ en répartissant de manière dirigée l'erreur sur tout le domaine. Le but est de minimiser l'erreur locale. Dans notre cas, les fonctions test ainsi que les fonctions de pondération ont été choisies comme des tenseurs de polynômes de Lagrange d'ordre d'interpolation p. C'est une méthode de Galerkin. Des précisions sur la méthode de Galerkin peuvent être trouvées dans les travaux de Fletcher (1984, 1991). Les polynômes de Lagrange sont de la forme.

$$L_i(\xi) = \prod_{j=0, j\neq i}^{p} \frac{\xi - \xi_j}{\xi i - \xi_j}. \tag{2.23}$$

où i et j sont les indices des points et ξ est la coordonnée spatiale. Un tenseur des polynômes de Lagrange en deux dimensions $N_{q,s}(\xi, \eta)$ est le produit d'un polynôme de Lagrange $L_q(\xi)$ dans une direction avec un polynôme de Lagrange $L_s(\eta)$ dans l'autre direction. La minimisation du maximum de l'erreur locale se fait en imposant nul le produit scalaire (dans l'espace des fonctions) du résidu avec le tenseur $N_{q,s}$. En utilisant le système de coordonnées de l'élément, on obtient alors l'équation

$$\iint_{\mathscr{E}} \mathbf{R} N_{q,s}(\xi, \eta) J(\xi, \eta) \mathrm{d}\xi \mathrm{d}\eta = 0 \tag{2.24}$$

où $\mathscr{E}$ est le domaine numérique entier et J la matrice Jacobienne associée au changement de coordonnées.

Il est ensuite possible d'utiliser ce schéma lors de chacune des étapes du time-splitting présentées en 2.3.2. En utilisant les équations (2.11), (2.13) et (2.14) et (2.18) et en profitant de la propriété d'associativité de l'intégrale, on peut alors décomposer le résidu en une somme de termes que l'on va intégrer spatialement un par un. Chaque terme est de la forme

$$\iint_{\mathscr{E}} \mathbf{C} N_{q,s}(\xi, \eta) J(\xi, \eta) \mathrm{d}\xi \mathrm{d}\eta \tag{2.25}$$

où $\mathbf{C}$ est un champ vectoriel. Le développement peut continuer en exprimant $\mathbf{C}$ en tant que somme de polynômes de Lagrange. On peut également développer $N_{q,s}$ dans les deux directions pour obtenir l'expression

$$\iint_{\mathscr{E}} \sum_{i,j=0}^{p} \mathbf{C}^*_{i,j} L_i(\xi) L_j(\eta) L_q(\xi) L_s(\eta) \mathbf{J}(\xi, \eta) \mathrm{d}\xi \mathrm{d}\eta, \tag{2.26}$$

où $\mathbf{C}^*$ est un champ vectoriel exprimé en chaque nœud. i est la position du nœud dans la direction ξ et j est la position du nœud dans la direction η.

En posant

$$\Phi_{i,j} = (\phi_i, \phi_j)\,, \tag{2.27}$$

on peut insérer la condition de quadrature de Gauss-Lobatto-Legendre pour réécrire l'expression (2.26) sous la forme

$$\sum_{k,l=0}^{p} \Phi_{k,l} \sum_{i,j=0}^{p} \mathbf{C}^*_{i,j} L_i(\xi_k) L_j(\eta_l) L_q(\xi_k) L_s(\eta_l) \mathbf{J}(\xi_k, \eta_l), \tag{2.28}$$

où k représente la position dans la direction ξ et l la position dans la direction η. On peut ensuite simplifier considérablement cette expression en profitant de la propriété des polynômes de Lagrange selon laquelle

$$L_i(\xi_k) = \delta_{ik} \ \forall (i,k) \in \mathbb{N}^2 \tag{2.29}$$

où δ_{ik} est le symbole de Kronecker. On aboutit finalement à une expression très simple du type

$$\Phi_{q,s} = \mathbf{J}(\xi_q, \eta_s) \mathbf{C}^*_{q,s}. \tag{2.30}$$

En procédant de la même manière pour tous les termes issus de l'équation (2.22), on obtient un système d'équations linéaires résoluble pour le champ de pression et de vitesse dans tout le domaine.

Il a été démontré dans Thompson *et al.* (1996) que la méthode ici présentée converge spatialement de manière exponentielle quand le degré des polynômes de Lagrange p augmente.

2.3.4 Conditions aux limites

De manière à fermer le système d'équations présenté dans le chapitre 2.3.1, il est nécessaire de poser des conditions sur les valeurs des champs des vitesses aux limites du domaine. Pour cela, on impose une vitesse constante dans le temps sur les quatre frontières du domaine présenté figure 2.3. Pour chaque limite, on choisit d'utiliser la valeur initiale du champ présenté par (2.8). On justifie cette hypothèse par le fait que les frontières du domaine se trouvent très écartées des tourbillons ($D/a \approx 60$, voir tableau 2.1). On peut aussi rappeler que la diffusion visqueuse est très lente et que ses effets sont principalement localisés où les gradients de vitesse sont les plus important : dans les vortex.

2.3.5 Mise en œuvre

Le tourbillon gaussien est un modèle de vortex bien connu théoriquement. Notamment, si l'on rajoute la condition de diffusion visqueuse du rayon présentée §1.2.2, le modèle ainsi créé est une solution autosimilaire des équations de Navier–Stokes. En revanche, une paire de tourbillons axisymétriques gaussiens ne satisfait pas aux équations de la mécanique des fluides, elle n'est pas solution des équations d'Euler. Cela est dû au fait que dans ce modèle, l'influence du premier vortex sur

l'autre n'est pas prise en compte. En effet, l'approximation des vortex ponctuels montre que chaque vortex induit un champ d'étirement situé à l'emplacement de l'autre. La conséquence de cela est une déformation des vortex. Moore & Saffman (1971) ont montré qu'un patch de vorticité prenait une forme elliptique quand il était plongé dans un champ d'étirement. Pour des profils de vorticité continus, le même résultat a été obtenu par Ting & Tung (1965) et Jiménez, Moffatt & Vasco (1996).

De plus, la présence d'un tourbillon au cœur d'un champ d'étirement de taux S_e influe directement sur la valeur du taux d'étirement au centre du vortex S_i. Pour un tourbillon de Rankine, Moore & Saffman (1971) ont montré que $S_i = 2S_e$. L'étirement effectif au centre est donc augmenté. Des résultats abondant dans le même sens ont été trouvés par Moffatt, Kida & Ohkitani (1994) pour un vortex gaussien. Ensuite, Le Dizès & Laporte (2002) ont montré que la correction de l'étirement au centre du tourbillon, pour tenir compte de la vorticité, était un moteur de l'instabilité elliptique. Il nous est donc nécessaire d'établir un écoulement tenant compte de cet aspect.

De nombreux travaux ont étudié le processus d'adaptation d'un tourbillon dans un champ d'étirement (Bassom & Gilbert, 1999; Sipp, Jacquin & Cossu, 2000). Pour des vortex co-rotatifs, Le Dizès & Verga (2002) ont montré qu'en partant d'une paire de tourbillons bidimensionnels, axisymétriques et de profils de vorticité variés, la résolution des équations de Navier–Stokes implique une phase de relaxation rapide au cours de laquelle chaque vortex s'équilibre avec l'autre en se déformant elliptiquement. Dans le repère tournant, un état quasi-stationnaire est ensuite atteint[2], qui se comporte comme une solution attractive. Ils ont trouvé que le système de tourbillons ainsi obtenu est principalement caractérisé par a_e/b où a_e est le rayon de vorticité défini par l'équation (2.50) page 36. Si la phase de relaxation dépend du profil de vorticité initial, en revanche, ils montré que l'état quasi-stationnaire trouvé est indépendant du modèle des tourbillons initiaux. Il est donc possible de l'obtenir en initialisant la simulation avec une paire de tourbillons gaussiens. Ces résultats ont été utilisés avec succès pour les simulations numériques présentées par Le Dizès & Verga (2002) et Lacaze *et al.* (2007). On utilise la même méthode pour obtenir notre écoulement final en partant de l'écoulement présenté dans (2.8).

Afin d'estimer l'état d'avancement de la phase de relaxation, on peut observer l'excentricité ϵ du vortex elliptique. Pour cela, on se concentre sur la partie du domaine présenté sur la figure 2.4 pour laquelle $x \geqslant 0$. On se place dans le repère tournant. Le centre d'un vortex est tel que ses coordonnées (x_c, y_c) vérifient

$$x_c = \iint_{x>0} x\omega \mathrm{d}x\mathrm{d}y/\Gamma \tag{2.31a}$$

$$y_c = \iint_{x>0} y\omega \mathrm{d}x\mathrm{d}y/\Gamma = 0. \tag{2.31b}$$

On pose θ_c l'angle d'orientation de l'ellipse par rapport à l'axe des x. θ_c est solution de l'équation

$$\iint_{x>0} \big[\cos\theta(x-x_c) + \sin\theta y\big]\big[\cos\theta(x-x_c) - \sin\theta y\big]\omega \mathrm{d}x\mathrm{d}y = 0. \tag{2.32}$$

[2]Le système ainsi atteint reste sujet à une lente diffusion visqueuse

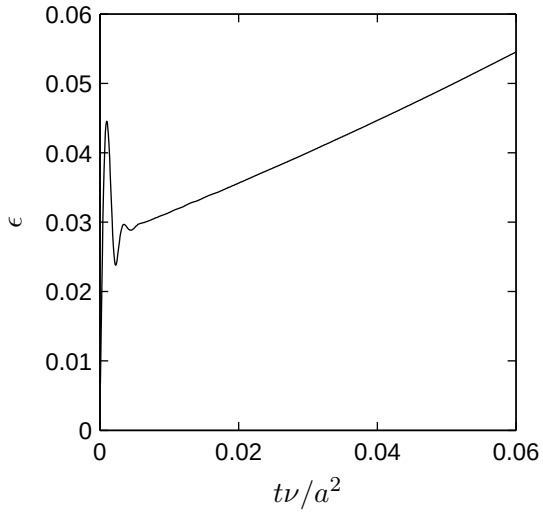

FIG. 2.6 – Évolution temporelle de l'excentricité ϵ pendant la phase de relaxation du tourbillon. On prend ici l'exemple de $Re = 1400$, $a/b = 0.14$. Le temps est adimensionné par le temps de diffusion visqueuse caractéristique.

Il est alors possible de définir le petit et grand rayon du vortex elliptique a_m et a_M par

$$a_m^2 = \frac{1}{\Gamma} \iint_{x>0} \left[\cos\theta_c(x - x_c) + \sin\theta_c y - x_c \right]^2 \omega \mathrm{d}x\mathrm{d}y, \tag{2.33a}$$

$$a_M^2 = \frac{1}{\Gamma} \iint_{x>0} \left[-\sin\theta_c(x - x_c) + \cos\theta_c y \right]^2 \omega \mathrm{d}x\mathrm{d}y. \tag{2.33b}$$

Ces deux rayons nous permettent alors de définir l'excentricité ϵ du vortex elliptique,

$$\epsilon = \frac{a_M - a_m}{a_M + a_m}. \tag{2.34}$$

Au cours de l'intégration temporelle, ϵ va varier fortement au cours du temps. On peut observer la figure 2.6 qui présente l'évolution de ϵ dans le temps. ϵ oscille de manière amortie autour d'un état moyen (voir Le Dizès & Verga, 2002) quasi-stationnaire. Quand l'amplitude de ces oscillations devient négligeable, on peut alors considérer que l'écoulement obtenu est solution des équations d'Euler. Il est alors possible de pratiquer une analyse de stabilité.

Pour la suite de l'étude, on définit le rayon de vorticité a d'après la méthode utilisée par Le Dizès & Laporte (2002) pour faciliter la comparaison des résultats entre les deux études. On utilise les coordonnées du centre du vortex (x_c, y_c) calculées par les formules (2.31) pour évaluer la rayon a grâce au second moment de vorticité :

$$a = \frac{1}{2\Gamma} \iint_{x>0} \left[(x - x_c^2) + (y - y_c^2) \right] \omega(x, y) \mathrm{d}x\mathrm{d}y. \tag{2.35}$$

On utilise cette méthode pour calculer le rayon a des tourbillons à la fin de la phase de relaxation. On tient ainsi compte de l'impact de la lente diffusion visqueuse. On vérifie également que la distance b entre les deux vortex n'a pas évolué. Le rapport a/b ainsi obtenu caractérise le champ de base (Le Dizès & Verga, 2002).

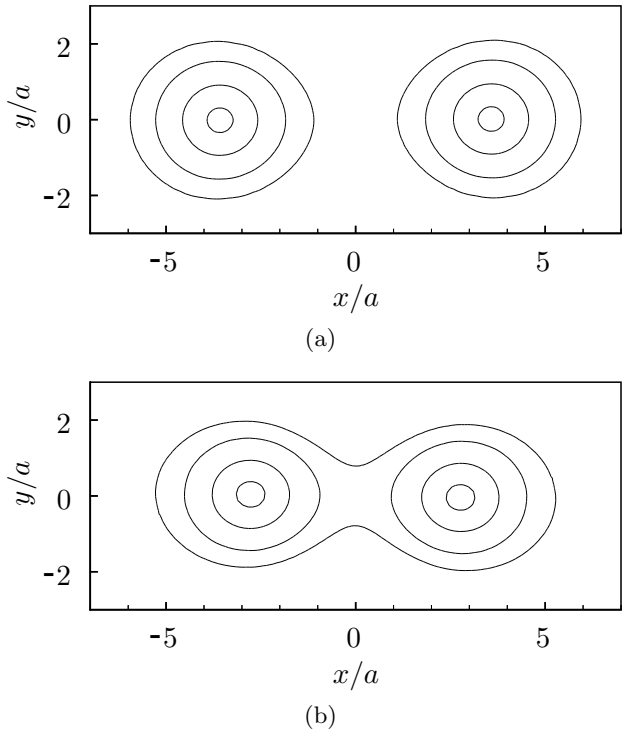

FIG. 2.7 – Iso-contours de vorticité correspondant à deux écoulement de base obtenus après relaxation à partir d'une paire de vortex gaussiens. (a) $a/b = 0.14$, (b) $a/b = 0.18$. La vorticité est adimensionnée par $\Gamma/\pi a^2$. De l'extérieur vers l'intérieur du domaine, les contours correspondent à 0.007, 0.07, 0.4, et 0.9.

2.4 Analyse de stabilité

2.4.1 Hypothèses de l'étude

Une fois que l'écoulement de base souhaité est obtenu, on peut pratiquer une analyse de stabilité. Le but est de calculer le taux de croissance d'une perturbation tridimensionnelle, de longueur d'onde axiale λ. Pour cela, on pose les mêmes hypothèses que celles décrites dans la partie 2.1. De manière à simplifier les calculs, on fait également l'hypothèse que la période T des perturbations est négligeable devant le temps caractéristique de la diffusion visqueuse :

$$T \ll \frac{a^2}{\nu}. \tag{2.36}$$

Cela permet de supposer l'écoulement de base stationnaire. On impose donc

$$\frac{\partial \mathbf{U}}{\partial t} = 0 \tag{2.37}$$

et

$$\frac{\partial P}{\partial t} = 0. \tag{2.38}$$

Il est ainsi possible de laisser évoluer un champ de perturbations sur un écoulement de base pour lequel les paramètres $Re = \Gamma/\nu$, $W_0 = 2\pi a W_{(r=0)}/\Gamma$ et a/b sont constants.

La bidimensionnalité de l'écoulement de base nous permet également de poser

$$\frac{\partial \mathbf{U}}{\partial z} = 0 \tag{2.39}$$

et

$$\frac{\partial P}{\partial z} = 0. \tag{2.40}$$

2.4.2 Résolution du champ des perturbations

On introduit maintenant $(\mathbf{u}, p)(t, x, y, z) = (u, v, w, p)$, le champ des perturbations tridimensionnel et on note $(\boldsymbol{\mathcal{U}}, \mathcal{P})(t, x, y, z) = (\mathcal{U}, \mathcal{V}, \mathcal{W}, \mathcal{P})$, le champ total issu de la somme du champ de l'écoulement de base avec le champ des perturbations tel que

$$(\boldsymbol{\mathcal{U}}, \mathcal{P}) = (\mathbf{U} + \mathbf{u}, P + p). \tag{2.41}$$

De même que le champ de l'écoulement de base, $(\boldsymbol{\mathcal{U}}, \mathcal{P})$ suit les équations de Navier–Stokes (2.9) ainsi que l'équation de continuité. En soustrayant membre à membre ces deux systèmes d'équations et en linéarisant par rapport aux perturbations, on obtient l'équation pour les perturbations

$$\frac{\partial \mathbf{u}}{\partial t} + (\mathbf{u} \cdot \nabla)\,\mathbf{U} + (\mathbf{U} \cdot \nabla)\,\mathbf{u} = -\frac{\nabla p}{\rho} + \nu \nabla^2 \mathbf{u} - \mathbf{2\Omega} \times \mathbf{u}, \tag{2.42a}$$

$$\nabla \cdot \mathbf{u} = 0. \tag{2.42b}$$

Le système (2.42) regroupe des équations différentielles du second ordre linéaires par rapport à z. Il est donc possible de chercher des solutions de la forme

$$\mathbf{u}(t,x,y,z) = \tilde{\mathbf{u}}_{\mathbf{1}}(t,x,y)\sin(2\pi z/\lambda) + \tilde{\mathbf{u}}_{\mathbf{2}}(t,x,y)\cos(2\pi z/\lambda)\,, \tag{2.43a}$$

$$p(t,x,y,z) = \tilde{p}_1(t,x,y)\sin(2\pi z/\lambda) + \tilde{p}_2(t,x,y)\cos(2\pi z/\lambda)\,. \tag{2.43b}$$

où $\tilde{\mathbf{u}}_{\mathbf{1}}, \tilde{\mathbf{u}}_{\mathbf{2}}, \tilde{p}_1$ et $\tilde{p}_2$ sont des fonctions ne dépendant pas de z. On simplifie ainsi la dépendance en z en une combinaison linéaire de deux harmoniques de période λ correspondant à la longueur d'onde axiale de la perturbation étudiée. Cela revient à faire un développement de Fourier dans la direction z pour un seul nombre d'onde. En substituant les expressions (2.43) dans le système (2.42), on obtient alors

$$\mathrm{D}_{xy}\tilde{u}_1 + \tilde{u}_1\frac{\partial U}{\partial x} + \tilde{v}_1\frac{\partial U}{\partial y} - \frac{2\pi}{\lambda}W\tilde{u}_2 = -\frac{\partial \tilde{p}_1}{\partial x} + \nu\nabla_\lambda^2\tilde{u}_1 + 2\Omega\tilde{v}_1, \tag{2.44a}$$

$$\mathrm{D}_{xy}\tilde{u}_2 + \tilde{u}_2\frac{\partial U}{\partial x} + \tilde{v}_2\frac{\partial U}{\partial y} + \frac{2\pi}{\lambda}W\tilde{u}_1 = -\frac{\partial \tilde{p}_2}{\partial x} + \nabla_\lambda^2\tilde{u}_2 + 2\Omega\tilde{v}_2, \tag{2.44b}$$

$$\mathrm{D}_{xy}\tilde{v}_1 + \tilde{u}_1\frac{\partial V}{\partial x} + \tilde{v}_1\frac{\partial V}{\partial y} - \frac{2\pi}{\lambda}W\tilde{v}_2 = -\frac{\partial \tilde{p}_1}{\partial y} + \nu\nabla_\lambda^2\tilde{v}_1 - 2\Omega\tilde{u}_1, \tag{2.44c}$$

$$\mathrm{D}_{xy}\tilde{v}_2 + \tilde{u}_2\frac{\partial V}{\partial x} + \tilde{v}_2\frac{\partial V}{\partial y} + \frac{2\pi}{\lambda}W\tilde{v}_1 = -\frac{\partial \tilde{p}_2}{\partial y} + \nu\nabla_\lambda^2\tilde{v}_2 - 2\Omega\tilde{u}_2, \tag{2.44d}$$

$$\mathrm{D}_{xy}\tilde{w}_1 + \tilde{u}_1\frac{\partial W}{\partial x} + \tilde{v}_1\frac{\partial W}{\partial y} - \frac{2\pi}{\lambda}W\tilde{w}_2 = \frac{2\pi}{\lambda}\tilde{p}_2 + \nu\nabla_\lambda^2\tilde{w}_1, \tag{2.44e}$$

$$\mathrm{D}_{xy}\tilde{w}_2 + \tilde{u}_2\frac{\partial W}{\partial x} + \tilde{v}_2\frac{\partial W}{\partial y} + \frac{2\pi}{\lambda}W\tilde{w}_1 = -\frac{2\pi}{\lambda}\tilde{p}_1 + \nu\nabla_\lambda^2\tilde{w}_2, \tag{2.44f}$$

$$\frac{\partial}{\partial x}\tilde{u}_1 + \frac{\partial}{\partial y}\tilde{v}_1 - \frac{2\pi}{\lambda}\tilde{w}_2 = 0, \tag{2.44g}$$

$$\frac{\partial}{\partial x}\tilde{u}_2 + \frac{\partial}{\partial y}\tilde{v}_2 + \frac{2\pi}{\lambda}\tilde{w}_1 = 0. \tag{2.44h}$$

où on définit les opérateurs linéaires

$$\mathrm{D}_{xy} = \frac{\partial}{\partial t} + U\frac{\partial}{\partial x} + V\frac{\partial}{\partial y}, \tag{2.45a}$$

$$\nabla_\lambda^2 = \frac{\partial^2}{\partial x^2} + \frac{\partial^2}{\partial y^2} - \frac{4\pi^2}{\lambda^2}. \tag{2.45b}$$

Il est ensuite possible de résoudre ce système linéaire de huit équations à huit inconnues afin d'obtenir les valeurs du champs $(\mathbf{u}, p)$. Les techniques d'interpolation spatiale et d'intégration temporelles sont basées sur le même principe que celles utilisées pour obtenir l'écoulement de base mais le caractère linéaire du système (2.44) simplifie sensiblement la démarche.

2.4.3 Calcul du taux de croissance

Une fois le champ des perturbations résolu, il est possible de caractériser l'évolution des perturbations en quantifiant leur croissance. En supposant que les

perturbations évoluent de manière linéaire, chaque composante de $\mathbf{u}$ et p va alors suivre une croissance exponentielle avec un taux de croissance σ. En pratique, on calcule σ en évaluant l'évolution de la norme $\mathscr{L}^2$ de $\mathbf{u}$ sur l'ensemble du domaine pendant un intervalle de temps. On utilise alors la relation

$$\|\mathbf{u}\|_{t'} = e^{\sigma(t'-t)}\|\mathbf{u}\|_t, \tag{2.46}$$

où on note

$$\|\mathbf{u}\|_t = \sum_{(x,y)\in\mathscr{E}} \sqrt{u^2(x,y,t) + v^2(x,y,t) + w^2(x,y,t)} \tag{2.47}$$

à l'instant t. En pratique, il suffit de sommer uniquement la première composante u du champ $\mathbf{u}$. On peut justifier cela en avançant que les modes étudiés étant globaux, la croissance de chaque composante de la vitesse doit être la même. Dans le cas contraire, la structure des modes changerait de période à période. Il a été vérifié que la valeur du taux de croissance obtenu ne dépend pas de la composante de la vitesse choisie. On évalue finalement σ par la relation

$$\sigma = \frac{\ln\left(\sum_{\mathscr{E}} \sqrt{u^2(x,y,t')}\right) - \ln\left(\sum_{\mathscr{E}} \sqrt{u^2(x,y,t)}\right)}{t'-t} \tag{2.48}$$

Dans le cas d'une paire de vortex contra-rotatifs, on adimensionne σ par le temps de retournement de la paire $2\pi^2 b^2\Gamma/\sigma$.

Le champ des perturbations est initialisé numériquement par un bruit aléatoire tridimensionnel. Il y a donc une infinité de modes de géométries différentes qui sont tenus en compte dans l'évaluation de $\|\mathbf{u}\|_t$. Cependant, de part la nature exponentielle de la croissance de ces modes, l'intégration des équations dans le temps va entraîner une sélection du mode le plus instable ou le moins stable qui va alors, à terme, s'avérer prédominant devant tous les autres. Si, au début, la grandeur σ calculée en utilisant (2.46) n'a rien de physique, il suffit d'attendre un temps suffisant pour qu'elle corresponde au taux de croissance du mode dominant. L'évolution temporelle de σ est présentée dans la figure 2.8. Quand σ ne varie plus, le mode le plus instable est sélectionné. Il existe cependant des configurations pour lesquelles les modes les plus instables sont complexes. $\sigma(t)$ est, dans ce cas, une fonction périodique. Le taux de croissance est alors obtenu en calculant la moyenne temporelle.

2.5 Validation

Afin de valider les résultats obtenus par cette étude, il et nécessaire de prouver l'efficacité de la méthode de résolution utilisée par le code. Il convient également de justifier les choix réalisés sur les valeurs des paramètres techniques. On pense au maillage utilisé, au pas de temps et au degré des polynômes d'interpolation.

2.5.1 Validation du code utilisé

Le code utilisé au cours de l'étude est le fruit d'un travail de développement réalisé par M.C. Thompson. Avec succès, il a servi de base à de nombreuses études.

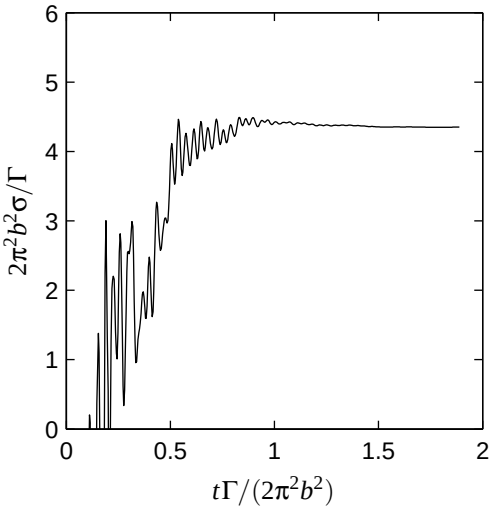

FIG. 2.8 – Exemple d'évolution temporelle du taux de croissance calculé pour $Re = 1400$, $a/b = 0.14$, $W_0 = 0.02$ et $2\pi a/\lambda = 3.52$

On peut notamment citer Thompson, Leweke & Williamson (2001*b*), qui ont étudié les mécanismes de transition dans les sillages de bluff body. Sheard, Thompson & Hourigan (2003) ont analysé la stabilité du sillage d'un anneau. On peut également citer l'étude de Leontini, Stewart, Thompson & Hourigan (2006) sur le sillage d'un cylindre oscillant à faible nombre de Reynolds. Plus particulièrement, Lacaze *et al.* (2007) ont étudié la stabilité d'une paire de vortex contra-rotatifs avec écoulement axial en partant de tourbillons gaussiens.

2.5.2 Méthode de la validation des paramètres

Pour la validation du maillage, du pas de temps et du degré des polynômes d'interpolation utilisés, on se base sur la phase de relaxation de l'écoulement de base. On considère une solution obtenue à l'aide de paramètres assurant une haute résolution, un faible pas de temps et un maillage couvrant un domaine important. On suppose que l'erreur obtenue sur la solution grâce à ces paramètres est négligeable. Elle devient une solution de référence à laquelle les résultats issus de configurations moins précises mais aussi moins coûteuses seront comparés. On utilise pour cela deux grandeurs pour comparer les résultats obtenus : le rayon basé sur l'ellipticité du vortex a_e et l'excentricité ϵ du vortex elliptique défini par (2.34). On définit a_e par

$$a_e = \sqrt{\frac{a_m^2 + a_M^2}{2}} \tag{2.49}$$

où a_m et a_M sont définis dans 2.3.3. Le rayon a_e a la particularité de suivre la loi de diffusion visqueuse (Batchelor, 1967)

$$a_e^2 = a_{e0}^2 + 4\nu(t - t_0). \tag{2.50}$$

où $a_{e0} = a_e(t_0)$.

On désire comparer les valeurs de a_e et de ϵ obtenues avec une configuration test, avec les valeurs obtenues avec la configuration de référence. On définit alors e_a, l'erreur sur a, et e_ϵ, l'erreur sur ϵ :

$$e_a = \frac{a_{ref} - a_{test}}{a_{ref}}, \tag{2.51a}$$

$$e_\epsilon = \frac{\epsilon_{ref} - \epsilon_{test}}{\epsilon_{ref}}, \tag{2.51b}$$

où les indices $_{ref}$ et $_{test}$ se rapportent à la solution de référence et à la solution test. Pendant la phase de relaxation, on calcule e_a et e_ϵ à chaque itération dans le temps. Il est ensuite possible d'évaluer les écarts types δ_a et δ_ϵ portant sur ces quantités. Les grandeurs ainsi définies tiennent donc compte de l'erreur sur toute la plage du temps correspondant à la génération de l'écoulement de base. On se sert de ces paramètres pour apprécier la précision d'une configuration.

2.5.3 Validation des paramètres

On présente dans cette section une étude de convergence servant à valider la précision des calculs. On prend pour cet exemple l'écoulement de base pour lequel $a/b = 0.14$. On a également $Re = \Gamma/\nu = 14000$. Dans ce cas, la solution de référence a été obtenue avec

$$L_{ref}/a = 16.25, \tag{2.52a}$$

$$\Delta t_{ref} = 0.005, \tag{2.52b}$$

$$p_{ref} = 13, \tag{2.52c}$$

où le pas de temps Δt est exprimé en unités de temps numérique.

Validation du maillage

Dans chacune des configurations étudiées ici, seule la taille du domaine L change par rapport à la solution de référence. On choisit $L/a = 8.75$ pour optimiser le temps de calcul tout en gardant une erreur acceptable.

Validation du pas de temps et du degré des polynômes d'interpolation

Les solutions étudiées dans les figures 2.10 et 2.11 utilisent la taille de domaine optimisée $L/a = 8.75$ choisie en 2.5.3. Les conditions de Courant imposent une dépendance entre Δt et p du point de vue de la convergence. On utilise donc pour les solutions présentées dans la figure 2.10, le degré d'interpolation optimisé en 2.11 et inversement. Cette étape de la validation se fait donc de manière couplée. On ne présente ici que les figures correspondant aux valeurs choisies. Finalement, on opte pour $p = 10$ et $\Delta t = 0.025$.

Résultats de la validation

Pour les deux cas étudié avec le code à éléments spectraux, ($\mathrm{R}e = 14000, a/b = 0.14$) et ($\mathrm{R}e = 14000, a/b = 0.18$), les paramètres numériques utilisés sont listés

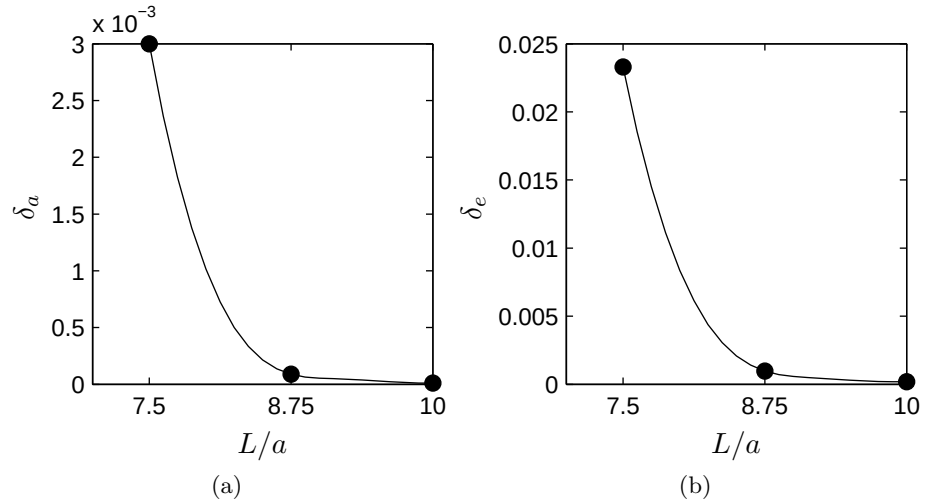

FIG. 2.9 – Écart type de l'erreur de la solution étudiée par rapport à un état de référence au cours de la phase de relaxation pour différentes tailles de domaine interne L. (a) et (b) caractérisent le rayon a et l'excentricité globale e.

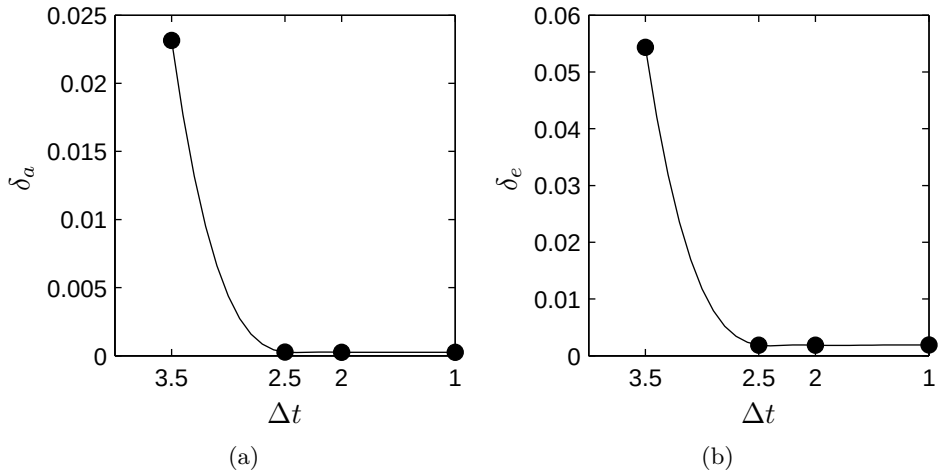

FIG. 2.10 – Écart type de l'erreur de la solution étudiée par rapport à un état de référence au cours de la phase de relaxation pour différents pas de temps Δt. (a) et (b) caractérisent le rayon a et l'excentricité globale e. Le pas de temps est exprimé en unités arbitraires.

dans le tableau 2.1. On notera notamment que pour $a/b = 0.14$, l'analyse de stabilité pour les grandes valeurs de W_0 a nécessité l'utilisation d'un maillage permettant une plus forte densité des points au cœur du vortex. On a, pour cela, utilisé le maillage présenté à la figure 2.5. Cela peut s'expliquer, à posteriori, par la complexification spatiale des structures des modes les plus instables quand W_0 augmente (voir chapitre 3), entraînant l'apparition de structures de plus en plus fines dans le cœur du vortex.

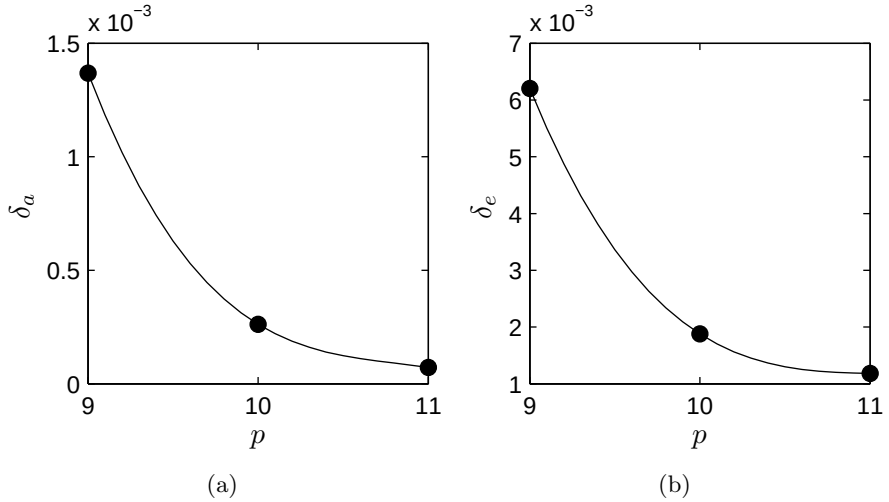

(a) (b)

FIG. 2.11 – Écart type de l'erreur de la solution étudiée par rapport à un état de référence au cours de la phase de relaxation pour différents degrés p des polynômes de Lagrange. (a) et (b) caractérisent le rayon a et l'excentricité globale e.

Re	a/b	W_0	$2\pi a/\lambda$	D/a	L/a	n_v	p	Δt
14000	0.14	[0,0.35]	[0.8,4.8]	62.5	8.75	289	10	0.025
14000	0.14	[0.35,0.6]	[0.8,4.8]		7	441	6	0.04
14000	0.18	[0,0.58]	[0.8,5]	62.5	8.75	289	11	0.01

TAB. 2.1 – Récapitulatif des paramètres utilisés lors des simulations. n_v est le nombre de points dans le cœur du vortex.

Chapitre 3

Résultats de l'analyse de stabilité

Ce chapitre est constitué d'un article publié dans *Physics of fluids* sous la référence : "Stability of a pair of co-rotating vortices with axial flow", Roy C., Schaeffer N., Le Dizès S. & Thompson M. C. *Physics of fluids*. **20**, 094101 (2008). Il expose les résultats obtenus concernant l'étude de stabilité linéaire d'une paire de tourbillons co-rotatifs avec la présence d'un écoulement axial.

Abstract

The three-dimensional linear temporal stability properties of a flow composed of two co-rotating q-vortices (also called Batchelor vortices) are predicted by numerical stability analysis. As for the corresponding counter-rotating case, when the axial flow parameter is increased, different instability modes are observed and identified as a combination of resonant Kelvin modes of azimuthal wavenumbers m and $m+2$ within each vortex. In particular, we show that the sinuous mode, which is the dominant instability mode without axial flow, is stabilized in the presence of a moderate axial flow. Different types of mode with a large amplitude in the critical layer are also identified. For small separation distances (above the merging threshold), unstable eigenmodes, corresponding to axial wavenumbers which cannot be easily identified with simple resonant interactions of Kelvin modes, are also observed. Their growth rate is a substantial fraction of the growth rates of low-order resonant modes. The effects of Reynolds number and vortex separation distance on the growth rate parameter map are considered. Finally, we analyze the similarities and differences between the stability characteristics of co- and counter-rotating vortex pairs.

3.1 Introduction

Large commercial aircrafts are known to create multiple trailing-vortex systems. These vortices can induce large turning moments on an aircraft following, which can be particularly dangerous during takeoff and landing. Given the vortex strength scales with aircraft size, the imminent introduction of several new and much larger passenger aircrafts means that this problem is worsening over time,

and must be explicitly taken account of in air-traffic scheduling. From a purely scientific point-of-view, the component vortices take part in a complex dynamical evolution including merging, and the end result is generally a pair of counter-rotating vortices in the far wake. The two co-rotating vortices generated by the tip of the wing and the outer flap constitute the prototype vortex system that provides one motivation for the analysis presented here, although the focus of this study is mainly theoretical. The goal is to provide the three-dimensional instability characteristics when the two vortices are identical co-rotating q-vortices (or Batchelor vortices[1]) including axial flow in their cores.

The *two-dimensional* large Reynolds number dynamics of co-rotating vortex pairs is now well-understood. When the vortices are far-apart, their dynamics is well-described by the point vortex approach (Saffman, 1992) ; the two vortices remain in equilibrium with each other, and their cores are elliptically deformed owing to the strain field induced by the other vortex (Le Dizès & Verga, 2002). When they are positioned closer to each other, equilibrium is no longer possible and the two vortices merge to form a single vortex (e.g. Meunier, Le Dizès & Leweke, 2005). When the Reynolds number is large, the two-dimensional dynamics is affected by the development of three-dimensional instabilities. Meunier & Leweke (2005) observed experimentally that a sinuous deformation of each vortex core develops and modifies the merging process. This instability is due to the elliptic character of the streamlines and has been observed in several other systems (see Kerswell (2002) for a review and references). A model has been developed for a vortex pair without axial flow by Le Dizès & Laporte (2002). It was demonstrated that the sinuous deformation corresponds to the resonant combination of two stationary Kelvin modes of azimuthal wavenumbers $m = 1$ and $m = -1$. Subsequently, the effect of axial flow on counter-rotating vortices was analyzed by Lacaze, Birbaud & Le Dizès (2005a) and Lacaze, Ryan & Le Dizès (2007). Lacaze *et al.* (2007) considered a pair of counter-rotating Batchelor vortices. They demonstrated that other instability modes with different azimuthal and temporal characteristics were excited when axial flow was added. They were able to show that each instability mode corresponds to a resonant combination of two Kelvin modes of azimuthal wavenumbers m and $m + 2$.

This work naturally follows on from that investigation of the stability of a pair of equi-strength counter-rotating vortices (Lacaze *et al.*, 2007) ; however, it extends that analysis in a number of ways. First, the choice of co-rotating vortices means that the individual vortices undergo rotation about their centroid, rather than the pure self-induced translation of the counter-rotating case. The addition of the associated centrifugal/Coriolis terms to the equations of motion complicates the theoretical stability analysis considerably, which is yet to be completed. The present paper investigates the problem using numerical stability analysis, and explicitly studies the effect of these terms on the stability characteristics. Second, while the theoretical analysis focuses on the resonance between particular pairs of Kelvin modes, at moderate strain rates, most of the wavenumber-axial flow parameter space lead to positive growth ; this aspect was not explored. In particular, as pointed out by Lacaze *et al.* (2007), the theoretical analysis does not take into

[1]Herein, we use this common terminology, although the solution initially obtained by Batchelor (1964) was the leading order approximation describing the spatial development of far wake trailing line vortices.

account the deviations from ellipticity of the vortices or the presence of the hyperbolic point between the two vortices, which is automatically accounted for by the numerical stability analysis. Surprisingly, the background growth rate can be almost as high as the growth rate corresponding to identifiable resonant interactions. Third, modes with substantial amplitude in the critical layer are identified.

3.2 Formulation

3.2.1 Base flow

The formulation mainly follows the numerical part of Lacaze *et al.* (2007), except that here, we consider co-rotating vortices instead of counter-rotating vortices. We take as the base flow, the z-independent flow obtained from the two-dimensional interaction of two co-rotating Batchelor vortices. Each Batchelor vortex taken alone is a solution of the Navier-Stokes equations. Its axial velocity and axial vorticity can be written in cylindrical coordinates as

$$\omega_z = \frac{\Gamma}{\pi a^2} e^{-(r/a)^2} \quad ; \quad U_z = \frac{\xi a_0^2}{a^2} e^{-(r/a)^2} \ , \tag{3.1}$$

where the circulation Γ, the axial velocity strength ξ and initial core radius a_0 are constants. The radius $a(t)$ evolves owing to viscous diffusion according to

$$a(t) = \sqrt{4\nu t + a_0^2} \ , \tag{3.2}$$

where ν is the kinematic viscosity.

The sum of two co-rotating Batchelor vortices is not a solution. As explained in Le Dizès & Verga (2002), in the two-dimensional dynamics, there is first a rapid relaxation process during which each vortex equilibrates with the other. In the frame rotating at the angular speed of the vortex pair, a quasi-steady solution is reached which subsequently slowly evolves due to viscous diffusion. As long as the system is far from the merging threshold ($a/b < 0.23$), the two vortices remains separated by a constant distance b and rotate around each other at a constant angular speed $\Omega = \Gamma/(\pi b^2)$. Each vortex also feels the strain field induced by the presence of the other one. Its streamlines are deformed elliptically at leading order and this makes each vortex sensitive to the elliptic instability. The two-dimensional simulation is necessary to obtain a correct estimate of the strain field within each vortex. In particular, as noted in Le Dizès & Verga (2002), the strain rate at the vortex center is twice as large as obtained from summing the contributions from the two separate Gaussian vortices. What is remarkable is that after the relaxation process (and before merging), the vortex system is mainly characterized by a single parameter a/b where the vortex radius a evolves according to (3.2) as predicted for a single vortex.

The presence of axial flow does not modify these results because the axial flow and axial vorticity dynamics decouple. Moreover, as the axial flow satisfies the same advection-diffusion equation, it remains proportional to the axial vorticity during the whole two-dimensional evolution. In practice, we perform the two-dimensional simulation without axial flow and then add, after the completion of the relaxation process, an axial velocity component such that $U_z(x, y) = \frac{aW_0}{2}\omega_z(x, y)$.

After the relaxation period, the radius of each vortex has slightly evolved. It is this new value of a which is taken as the characteristic length scale for the stability analysis. The base flow is then characterized by 3 parameters, a/b, W_0 and the Reynolds number $Re = \Gamma/\nu$, although the base flow is mainly independent of this last parameter.

We shall consider a continuous range of W_0 between 0 and 0.6 for three couples of parameters $(Re = 14000, a/b = 0.14)$, $(Re = 14000, a/b = 0.18)$ and $(Re = 31400, a/b = 0.168)$, and provide some selected results for a few other combinations. For these values of W_0, the Batchelor vortex can be considered as stable. Weakly unstable center modes exist but their growth rate are so small (see Fabre & Jacquin, 2004*b*) that they never become dominant over the elliptic instability mode.

3.2.2 Perturbation analysis

The stability of the base flow obtained from the two-dimensional simulation is examined by considering the problem in the frame rotating with the vortices and for which the base flow is quasi-stationary. In this rotating frame, the Navier-Stokes equations including all the Coriolis terms, are linearized around the base flow. In addition, the weak diffusion of the base flow is suppressed by freezing the base flow. As the base flow is assumed homogeneous in the axial direction, and because the perturbation equations are linear and independent of z for the axial derivatives, the axial dependence can be represented as a Fourier series. Linearity allows the stability of each wavelength, $\lambda = 2\pi/k$, to be determined separately. In practice, for a given axial wavelength, the perturbation equations are integrated in time with a random field as an initial condition. The characteristics of the most unstable mode are obtained by integrating for a sufficiently long time. For each set of base flow parameters and each wavenumber k, we obtain the growth rate, the rotation frequency and the spatial structure of the most unstable mode.

3.2.3 Numerical codes

Two different numerical codes have been used. The first one was used for a similar study of counter-rotating vortices in Lacaze *et al.* (2007). It is based on a high-order spectral element technique which has been described in Thompson, Hourigan & Sheridan (1996) and applied to various related problems (e.g. Thompson, Leweke & Provansal, 2001*a*; Ryan, Thompson & Hourigan, 2005). The same code parameters and simulation domain as in Lacaze *et al.* (2007) are used here.

The second code has been developed for the present study and a nonlinear analysis to follow. It is a pseudo-spectral code, periodic in the three spatial Cartesian directions. Such a code is classical (Vincent & Meneguzzi, 1991) and has already been used for similar studies (Billant, Brancher & Chomaz, 1999; Otheguy, Chomaz & Billant, 2006). Because the code is fully spectral, it is very fast, but is in principle limited to flows with zero total circulation (Pradeep & Hussain, 2004). A trick has then to be used to simulate co-rotating vortex pairs for which the circulation is 2Γ : a solid body rotation $\Omega_0 \mathbf{e_z}$ has to be subtracted from the base flow so that the global circulation at the boundary of the domain is zero (Otheguy *et al.*, 2006). Time integration is performed using an Adams-Bashforth

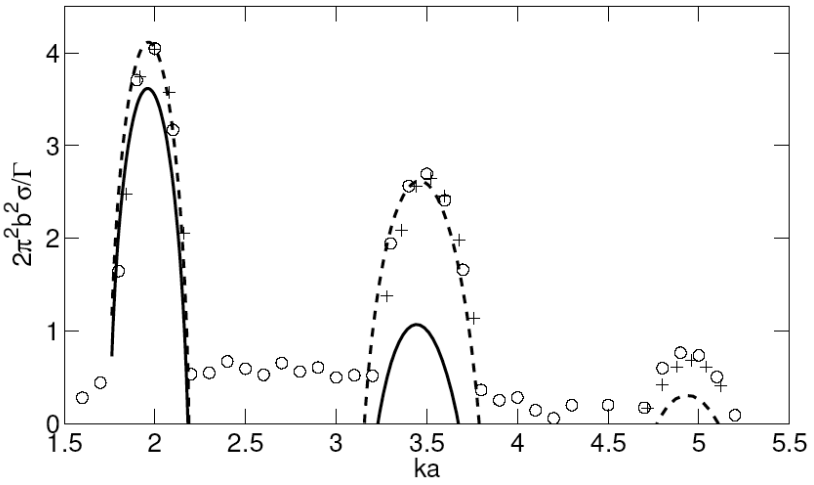

FIG. 3.1 – Comparison of the growth rate computed with the 2 codes for Re = 14000 and $a/b = 0.14$. Circles and crosses are data obtained with the fully spectral code and with the spectral-element code respectively. Theoretical predictions are in solid line [formula (6.1a) from Le Dizès & Laporte (2002)], and in dashed line [same formula with a viscous damping term computed by the global approach (see text)].

temporal scheme. For determining the 2D base flow, the size L of the square domain has been chosen sufficiently large to reduce the influence of image vortices. Typically, we have taken L/b between 5 and 6. A smaller domain with $L'/b \approx 2.5$, centered on the vortex pair has been taken for the simulation of the perturbation equations. This is possible because the perturbations are localized in the center of each vortex and decrease very fast to zero away from the vortices. Thus, there is no difficulty in considering the perturbations periodic on a smaller domain.

The two numerical codes have been compared and validated for a configuration without axial flow. In figure 3.1 is plotted the growth rate of the perturbations obtained by the two different codes, together with the theoretical formula[2]. As it can be seen, the two codes provide the same results for the first three modes. The relative error between the two codes is generally only a few percent. This difference was traced to a slight sensitivity of the growth rate predictions to the time allowed for quasi-equilibrium to be reached before freezing the base flow, which was slightly different for the two cases. On the other hand, the large underestimation of the growth rate by the theoretical formula is due to a incorrect estimate of the damping rate associated with viscous effects. In the theory, the damping rate is based on a local approach. If a global estimate is computed using the method of Lacaze *et al.* (2007), the viscous damping is found to be significantly smaller (Lacaze, private communication) and a much better estimate is obtained. The adjusted theoretical predictions are also shown on this figure by the dashed lines. Note that even this estimate loses accuracy for the higher wavelength mode.

[2]Note that there is a misprint in formula (6.1a) in Le Dizès & Laporte (2002) : b^2/a_1^2 should be b^4/a_1^4.

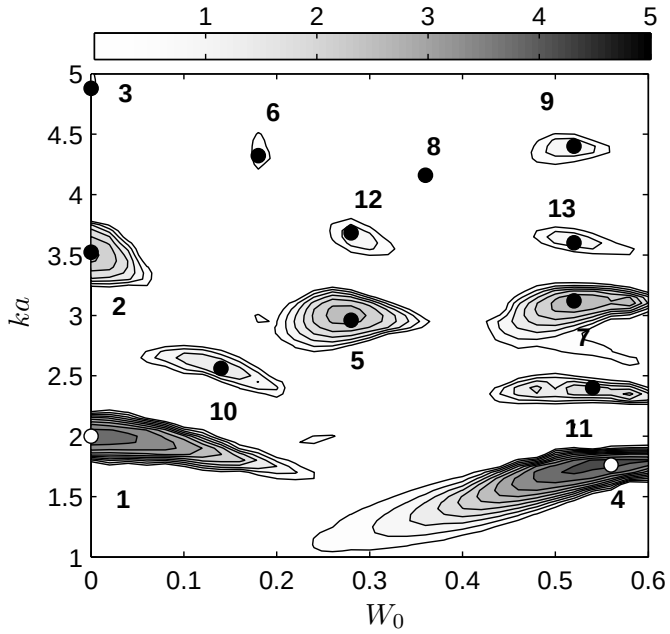

FIG. 3.2 – Contours of instability growth rate in the (W_0, ka) plane for $a/b = 0.14$ and Re = 14000. A number has been provided to each important unstable mode and is used hereafter to refer to each of them.

3.3 Results

3.3.1 Mode map

Using the procedure explained above, we have first explored a large part of the parameter space for a fixed Reynolds number $Re = 14000$ and $a/b = 0.14$, with a resolution step for W_0 and k of 0.002 and 0.1 respectively. The growth rate contours of the most unstable modes are displayed in figure 3.2. Only the growth rates (normalized by the turn-over time of the vortex pair) in excess of 0.5 have been indicated in this figure. It demonstrates the existence of several islands of instability. Each island corresponds to a specific instability mode. These modes are localized in the core of each vortex and have the same spatial structure in each vortex. Their spatial structure is shown in figure 3.3. The characteristics of each mode are also provided in table 3.1.

The first point to note is that the instability map shown in figure 3.2 is very similar to the map obtained for equal strength counter-rotating vortices (see figure 11 in Lacaze *et al.* (2007)). The first three modes, labeled 1, 2, 3, which have maximum growth rates for no axial flow but persist for small W_0, are the well-known sinuous modes of the elliptic instability (Meunier & Leweke, 2005). They correspond to the resonant combination of two Kelvin modes of azimuthal wavenumber $m = 1$ and $m = -1$. Here, the functional dependence of the Kelvin modes is written as $\exp(im\theta + ikz - i\omega t)$ where m and k are the azimuthal and axial wavenumbers, and ω the frequency. Moreover, we assume that k is positive. For $W_0 = 0$, the sinuous modes are stationary ($\omega = 0$) and have been called "principal modes" as they are formed from two Kelvin modes with the same (broad) radial

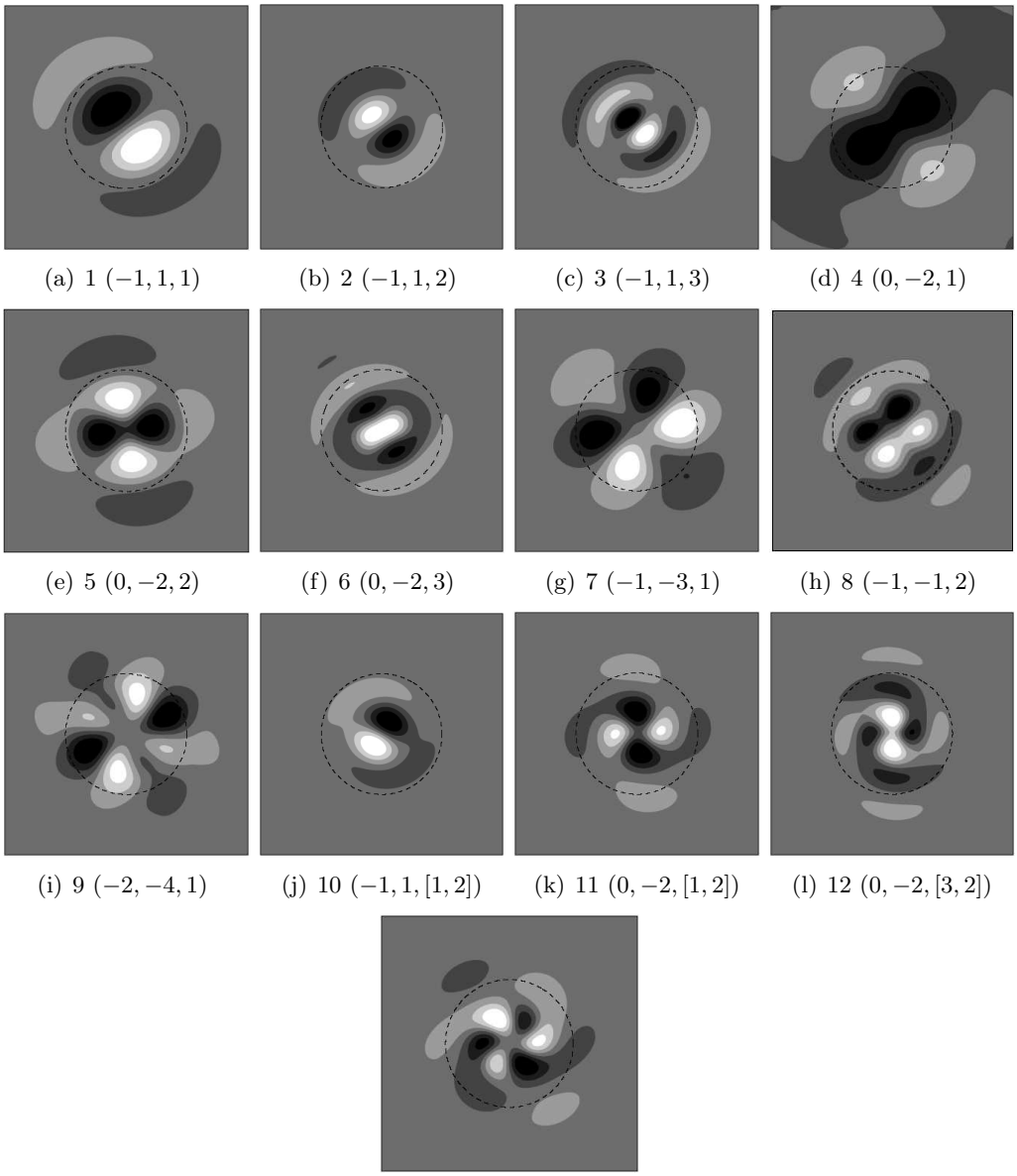

(a) 1 $(-1, 1, 1)$ (b) 2 $(-1, 1, 2)$ (c) 3 $(-1, 1, 3)$ (d) 4 $(0, -2, 1)$

(e) 5 $(0, -2, 2)$ (f) 6 $(0, -2, 3)$ (g) 7 $(-1, -3, 1)$ (h) 8 $(-1, -1, 2)$

(i) 9 $(-2, -4, 1)$ (j) 10 $(-1, 1, [1, 2])$ (k) 11 $(0, -2, [1, 2])$ (l) 12 $(0, -2, [3, 2])$

(m) 13 $(-1, -3, [1, 2])$

FIG. 3.3 – Axial vorticity perturbation fields resulting from the elliptical instability for Re = 14000 and $a/b = 0.14$. Each plot is associated with a number corresponding to one point identified in figure 3.2. Contours are linear and symmetric around 0. The dashed line is a circle of radius a centered on the vortex center.

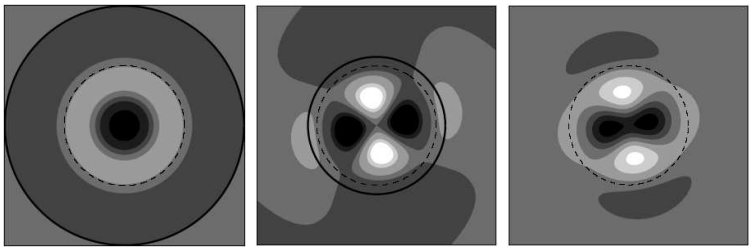

(a) (b) (c)

FIG. 3.4 – Azimuthal decomposition of the instability mode 5 : axial vorticity in a section perpendicular to the vortex axis. (a) Axisymmetric component ($m = 0$), (b) $m = \pm 2$ component, (c) superimposition of $m = 0$ and $m = \pm 2$ components. The circle (solid line) in figures (a) and (b) indicates the position of the turning point r_t (see text).

structure. The radial structure of the Kelvin mode can be identified by a label specifying the number of zeros of the radial velocity component of the mode in the vortex core (Lacaze *et al.*, 2007). Principal modes are denoted by (m_1, m_2, n) where m_1 and m_2 are the azimuthal mode numbers of the two resonant Kelvin modes and n their common (radial) label. It is possible to identify other resonant modes as combinations of Kelvin modes with different radial dependences, in which case the mode is denoted by $(m_1, m_2, [n_1, n_2])$. Examples of these mixed modes can be found in Lacaze *et al.* (2007).

The modes 1, 2 and 3 of figure 3.2 are the principal modes $(-1, 1, 1)$, $(-1, 1, 2)$ and $(-1, 1, 3)$ respectively. Their spatial structures shown in figures 3.3(a,b,c) have 1, 2 and 3 radial oscillations as indicated by their radial mode numbers. Comparatively to the counter-rotating case, the principal Coriolis effect is to modify the resonance condition, thus shifting the unstable modes toward smaller k which results in bigger growth rates.

For $W_0 = 0$, the numerical growth rate for these modes is in good agreement with the theory [see figure 3.1]. As the axial flow is progressively increased, these modes are progressively stabilized, as also predicted for counter-rotating vortex configurations (Lacaze *et al.*, 2007). As explained in Lacaze *et al.* (2007), this phenomenon has two different causes. First, as soon as an axial flow is present, the symmetry between the $m = 1$ modes and the $m = -1$ modes is broken. The resonance between the two helical modes becomes less efficient because their radial structures are no longer perfectly in phase. Moreover, the symmetry breaking creates a small detuning in the resonant frequency with respect to the frequency which maximizes the local instability in the vortex center. Thus, the strength of the local elliptic instability in the vortex center is also less important. The second cause is the damping of the Kelvin mode $m = -1$. The damping of this mode is due to the appearance of a viscous critical layer in its radial structure (Le Dizès, 2004; Fabre, Sipp & Jacquin, 2006). When the damping rate of the mode is greater than the growth rate associated with the resonance, the instability mode disappears.

The other instability modes which are destabilized for larger values of W_0 are no longer stationary sinuous modes. The mode labeled 5 corresponds to the principal mode $(-2, 0, 2)$ which has also been observed in the numerical simulation

	mode	m	n	W_0	$2\pi a/\lambda$	$2\pi^2 b^2 \omega/\Gamma$	$2\pi^2 b^2 \sigma/\Gamma$
Re = 14000, $a/b = 0.14$	1	-1,1	1	0	2.00	0	4.04
	2	-1,1	2	0	3.52	0	2.64
	3	-1,1	3	0	4.88	0	0.611
	4	0,-2	1	0.56	1.76	-28.8	2.85
	5	0,-2	2	0.28	2.96	-39.1	2.71
	6	0,-2	3	0.18	4.32	-42.3	0.868
	7	-1,-3	1	0.52	3.12	-84.7	2.88
	8	-1,-3	2	0.36	4.16	-91.16	0.30
	9	-2,-4	1	0.52	4.40	-141	1.23
	10	-1,1	1,2	0.14	2.56	-7.53	1.63
	11	0,-2	1,2	0.54	2.40	-26.3	1.30
	12	0,-2	3,2	0.28	3.68	-37.0	1.21
	13	-1,-3	1,2	0.52	3.60	-79.1	1.20
Re = 14000, $a/b = 0.18$	1	-1,1	1	0	1.76	0	5.21
	2	-1,1	2	0	3.12	0	4.99
	3	-1,1	3	0	4.48	0	4.73
	4	0,-2	1	0.58	1.68	-15.7	4.81
	5	0,-2	2	0.3	2.88	-20.1	3.74
	6	0,-2	3				
	7	-1,-3	1	0.54	3.04	-46.4	3.81
	8	-1,-3	2				
	9	-2,-4	1				
	10	-1,1	1,2	0.1	2.32	-0.59	4.50
	11	0,-2	1,2	0.56	2.24	-15.2	3.06
	12	0,-2	3,2				
	13	-1,-3	1,2				
Re = 31400, $a/b = 0.168$	1	-1,1	1	0	1.8	0	5.08
	2	-1,1	2	0	3.2	0	4.83
	3	-1,1	3	0	4.6	0	4.45
	4	0,-2	1	0.58	1.65	-20.7	4.84
	5	0,-2	2	0.28	2.88	-26.0	4.11
	6	0,-2	3	0.19	4.11	-27.0	3.39
	7	-1,-3	1	0.55	3	-53.95	4.21
	8	-1,-3	2	0.37	4.0	-59.8	2.85
	9	-2,-4	1	0.53	4.21	-93.6	3.49
	10	-1,1	1,2	0.1	2.4	-0.78	3.42
	11	0,-2	1,2	0.6	2.2	-15.97	3.0
	12	0,-2	3,2	0.305	3.47	-21.9	3.24
	13	-1,-3	1,2	0.56	3.4	-48.4	2.84

TAB. 3.1 – Parameters of the modes identified in figures 3.2, 3.6 and 3.7(a).

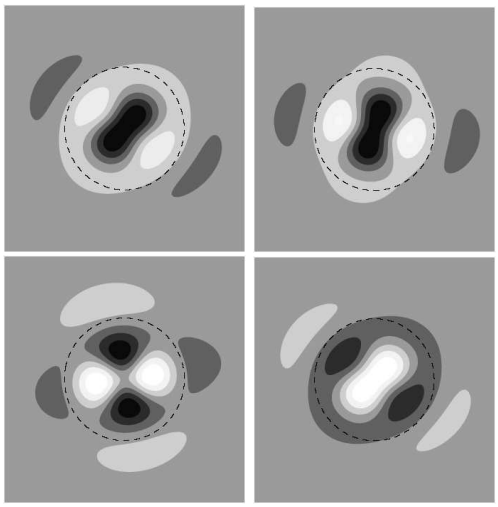

(a)

(b)

FIG. 3.5 – (a) Temporal evolution of the axial vorticity of the instability mode 5 during half a period. Times correspond to 0, $T/8$, $2T/8$, $4T/8$, respectively. (b) Three-dimensional visualization showing a vorticity isosurface indicating the deformation induced by mode 5. Here, the maximum vorticity of the instability mode is 0.4 times the maximum vorticity of the base flow.

of counter-rotating vortices. This mode is here the most unstable for $W_0 \approx 0.3$ and $ka \approx 3$. The label of the mode can be obtained by looking at the azimuthal decomposition of the instability mode in one of the vortices as shown in figure 3.4 for mode 5. The figures 3.4(a) and 3.4(b) show the $m = 0$ and the $m = \pm 2$ contribution to this instability mode while figure 3.4(c) is the superimposition of these two contributions alone. We clearly see that the eigenmode shown in figure 3.3(e) is well reproduced, confirming that mode 5 is mainly a combination of the azimuthal wavenumbers $m = 0$ and $m = \pm 2$. The time evolution and the three-dimensional structure of the mode, which are shown in figures 3.5(a) and (b) respectively, provide further information on the characteristics of the Kelvin modes involved in the construction of mode 5. We observe that the helical structure is right-hand oriented and rotates anti-clockwise. This indicates that the axial and azimuthal wavenumbers are of opposite sign, and the frequency and azimuthal wavenumber are of the same sign. Thus, our choice of positive k, $m = -2$ and

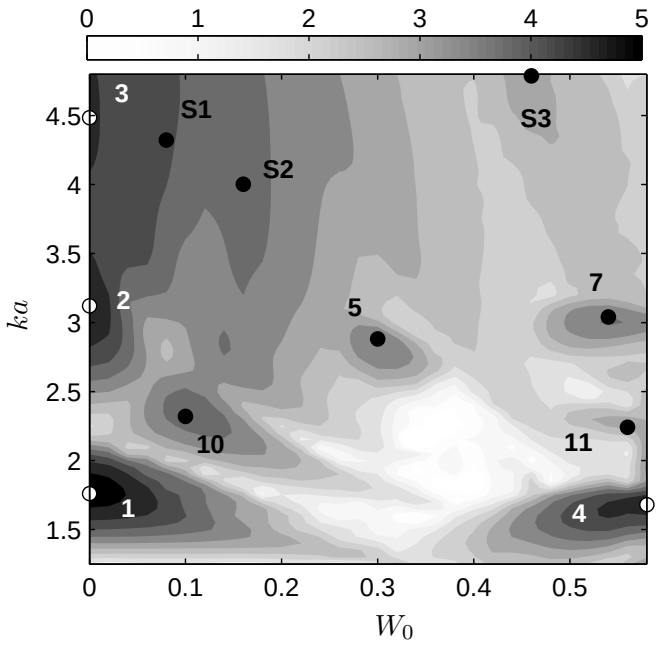

FIG. 3.6 – Same as figure 3.2 for $a/b = 0.18$ and $\mathrm{Re} = 14000$.

$\omega < 0$ (as indicated in table 3.1).

The label n of the Kelvin mode involved in the resonance can be obtained by looking at the radial variation of each azimuthal component. Le Dizès & Lacaze (2005) have shown that the label corresponds to the number of radial oscillations between the origin and a turning point r_t which delimits the region where the mode is localized. As explained in Le Dizès & Lacaze (2005), the radial location r_t can be computed from the vortex profile and the characteristics of the mode. The turning point r_t has been indicated for the $m = 0$ and $m = -2$ components of mode 5 in figures 3.4(a) and 3.4(b), respectively.

Using a similar azimuthal decomposition and by comparing the figures with the theoretical plot of Lacaze *et al.* (2007), the principal modes $(-2, 0, 1)$, $(-2, 0, 3)$, $(-3, -1, 1)$, $(-3, -1, 2)$ and $(-4, -2, 1)$ can be identified with the modes 4, 6, 7, 8 and 9 of figure 3.2 (see figure 3.3). Note that an $m = \pm 2$ structure is clearly visible on modes 4 and 6, $m = \pm 3$ structure on modes 7 and 8, and $m = \pm 4$ on mode 9. As expected, the maximum growth rate of the principal modes decreases as their axial wavenumber increases. Other instability modes are also visible in figure 3.2. They are not principal modes, which means that they involve Kelvin modes with different radial labels. A few of them have been illustrated in figure 3.3. By looking at the number of oscillations of the main azimuthal components, labels have been tentatively given for each of these modes.

3.3.2 Effects of Reynolds number and vortex separation distance variations

Similar contour plots to figure 3.2 are displayed in figures 3.6 and 3.7(a) for a/b increased from 0.14 to 0.18 (closer vortices) and a larger Reynolds number (Re increased from 14000 to 31400), respectively. A corresponding set of instabi-

lity modes as shown in figure 3.2 have also been identified in these figures. Their characteristics are given in table 3.1. When a/b is increased, the peaks associated with the main modes move slightly owing to the variation of the mean rotation $2(a/b)^2$ of the pair which modifies the conditions of resonance. In particular, the resonant mode positions are shifted to occur at slightly higher axial flow velocities and smaller wavenumbers. For example, for mode 4, an approximately 30% increase in a/b from 0.14 to 0.18, results in a shift in (ka, W_0) coordinates from (1.76, 0.56) to (1.68, 0.58). The relative shift is not uniform across all modes however ; the 30% change in a/b typically leads to approximately a 10% change in ka but only a few percent change in W_0. The position of the peaks is by contrast almost unaffected by variations of the Reynolds number. This is also clearly seen in figure 3.8(b) where growth rate variations are displayed for a fixed $W_0 = 0.29$ and for various Reynolds numbers.

An important feature of figures 3.6 and 3.7(a) is the global increase in the growth rate when either a/b or Re increases. For the range of parameters of these figures, almost the whole parameter space considered is now unstable. However, there are differences between increasing Reynolds number and increasing a/b. When the Reynolds number is increased, the growth rate peaks remain distinct : more modes become unstable but they can still be identified. Note in particular that mode 8, displayed in figure 3.3(h) and which corresponds to the principal mode $(-1, -3, 2)$, is now unstable, whereas it was almost stable for the parameters of figure 3.2. When a/b increases, the tendency is different. The peaks of the modes for large ka tend to disappear : the growth rate increases almost uniformly as ka increases. The trend is demonstrated in figure 3.8(a) for a fixed value of $W_0 = 0.29$ for $a/b = 0.18$. In addition, figure 3.9 shows the behavior for the zero axial velocity case. The growth rate ultimately decreases for large ka, but what is important is that there is no dominant mode selection in that case. Again, this is clearly indicated in figure 3.6, which shows specific modes are virtually indistinguishable from the background noise for $ka \gtrsim 3.5$ for $a/b = 0.18$. The modes for $ka \gtrsim 3.5$ are apparently mixed and most of them have a spiral-like structure as illustrated in figures 3.10(a-c).

The spiral structure is probably associated with a critical layer in one of the resonant modes (Lacaze *et al.*, 2007). This critical layer is known to be responsible for the stabilization of some modes, such as the mode $(-1, 1, 1)$ for increasing W_0. However, for increasing a/b, this stabilizing effect becomes less important. Moreover, the instability band also becomes wider and the frequency detuning between modes less important when a/b grows. Thus, we expect that more and more modes would become unstable in larger and larger overlapping instability regions. The consequence is that the growth rate possesses a large growth envelope with no sharp peaks.

3.3.3 Comparison of the stability of co- and counter-rotating vortex pairs

Le Dizès & Laporte (2002) compared the dominant instability modes for co- and counter-rotating vortices for the case without axial flow. In general, the growth rates of instabilities for counter-rotating vortices are lower than for co-rotating vortices and the corresponding wavenumbers of the modes lie between those of the

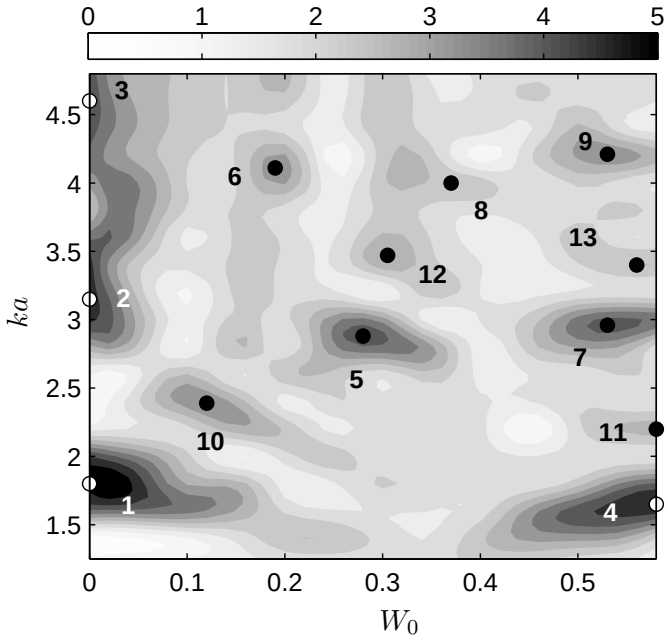

(a)

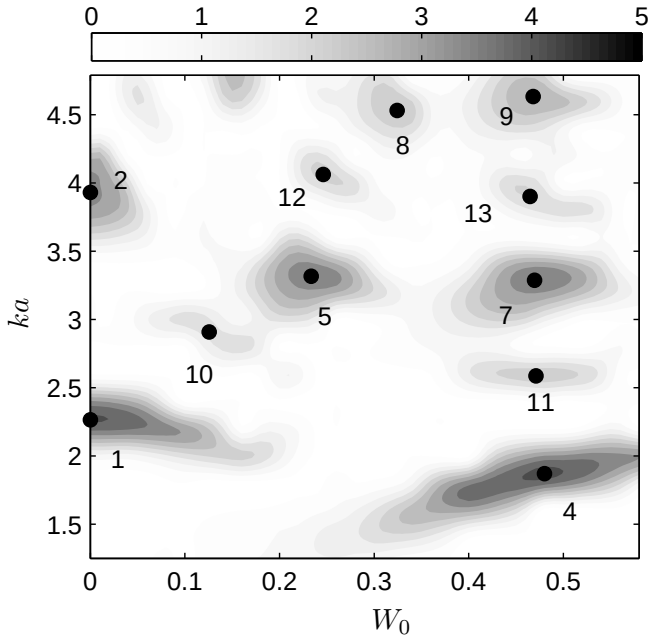

(b)

FIG. 3.7 – As for figure 3.2 for $a/b = 0.168$ and Re $= 31400$: (a) co-rotating vortices ; (b) counter-rotating vortices

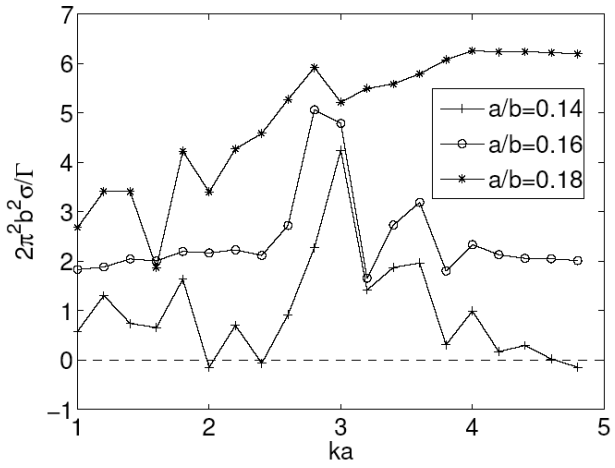

(a)

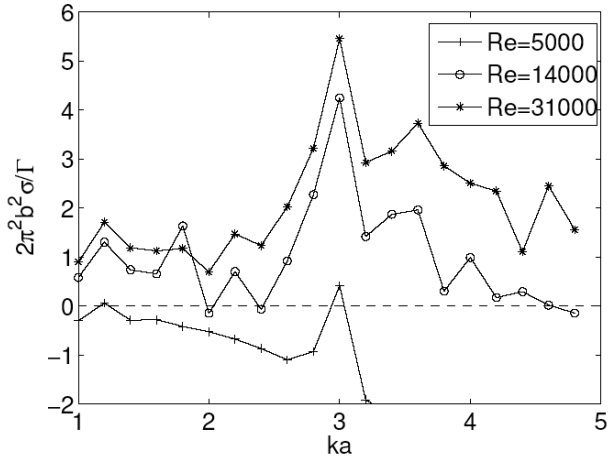

(b)

FIG. 3.8 – Instability growth rate versus axial wavenumber for $W_0 = 0.29$. (a) Vortex separation distance dependence for Re = 14000. (b) Reynolds number dependence for $a/b = 0.14$.

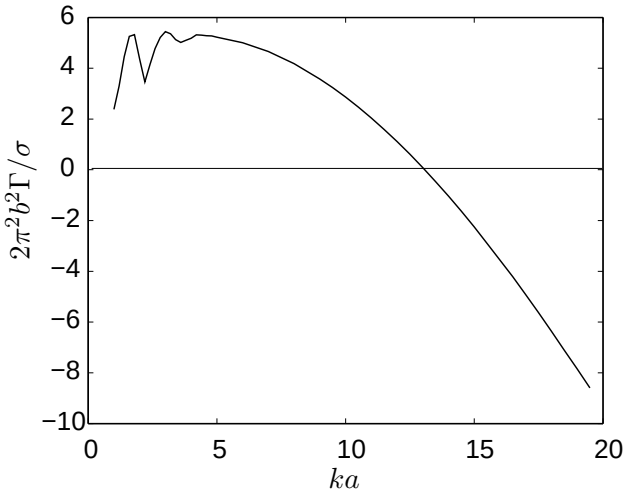

FIG. 3.9 – Growth rate as a function of wavenumber for the co-rotating case with no axial flow for Re = 14000 and $a/b = 0.18$.

other case. Figure 3.11 shows growth rate curves for the case without axial flow for $a/b = 0.168$ at Re = 31400, which highlights both effects. These predictions are consistent with the analytical and numerical predictions in Le Dizès & Laporte (2002). For the case with axial flow, for which an analytical theory is yet to be developed, figures 3.7(a) and (b) display the instability maps for the co- and counter-rotating cases for Re = 31400 and $a/b = 0.168$. This allows an explicit, albeit numerical, determination of the effect of the added Coriolis force on the stability of co-rotating vortex pairs. As previously mentioned, this difference from the counter-rotating case appears because of the mutually-induced rotation of the each vortex about their centroid, meaning that they appear quasi-stationary in a rotating frame.

There are both similarities and differences between the stability maps. The first point is that a similar set of identifiable modes corresponding to the same Kelvin mode interactions appears on each map in roughly the same locations. However, the actual positions of the modes for the co-rotating vortex map are shifted to approximately 20% higher axial velocities. Another key difference is the background growth rate between identifiable modes. This is very much larger in the co-rotating case, which is also clear from figure 3.9 at zero axial flow, which explicitly shows

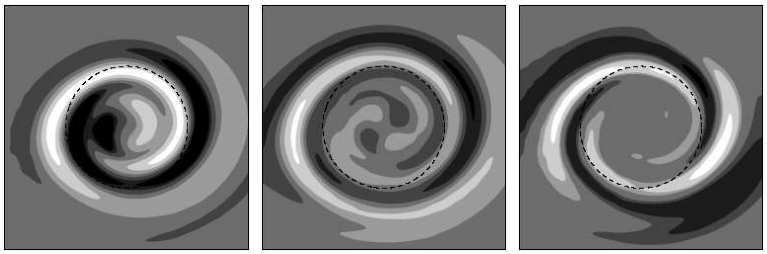

(a) S1 (b) S2 (c) S3

FIG. 3.10 – Instability modes with a critical layer (see fig. 3.6).

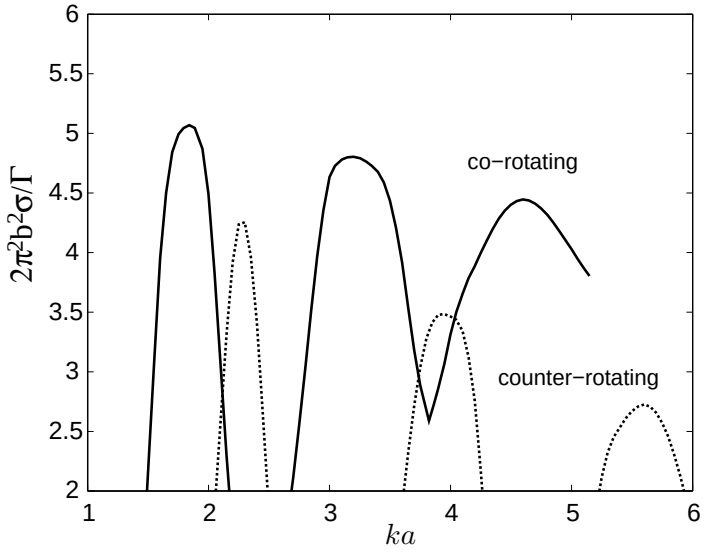

FIG. 3.11 – Comparison of growth rates for equal strength co- and counter-rotating vortices with zero axial velocity for $a/b = 0.168$ and $\mathrm{Re} = 31400$.

the slow falloff of the growth rate for high wavenumbers. Indeed, as discussed in the previous section, as a/b is increased to 0.18, the background growth rate virtually swamps the growth rate of local resonant Kelvin mode interactions for higher wavenumbers and may even dominate co-rotating vortex evolution for close vortex cores at particular axial core velocities. This effect occurs at separations well under the merging limit (Meunier *et al.*, 2005) for co-rotating vortices of $a/b \simeq 0.23$.

3.4 Conclusions

In this work, we have analyzed the linear stability of a co-rotating vortex pair with axial flow. We have demonstrated that new elliptic instability modes are destabilized by axial flow. For small Reynolds numbers and small a/b, we have shown that the instability diagram resembles the theoretical prediction for counter-rotating vortices (Lacaze *et al.*, 2007), although there are some explicit differences between these cases. When axial flow is progressively increased, the principal modes (combination of Kelvin modes of same radial branch label) of azimuthal wavenumbers $(-1, 1)$ are stabilized and replaced by other principal modes $(-2, 0)$, $(-3, -1)$ and $(-4, -2)$. For large Reynolds numbers or large a/b, other instability modes have been observed and associated with a combination of Kelvin modes with different labels. These other modes are less unstable than the principal modes, whose characteristics are almost invariant. But they make the vortex pair unstable in a large wavenumber band whatever the axial flow. Clearly, it would be interesting to determine the nonlinear evolution of the instability modes and its influence on the merging process.

3.5 Acknowledgments

We would like to thank Thomas Leweke and Kerry Hourigan for discussions and support. We are also grateful to Laurent Lacaze for having computed the theoretical viscous damping used to plot the dashed line in figure 3.1.

Deuxième partie

Étude expérimentale de tourbillons avec écoulement axial

Chapitre 4

Instabilité elliptique dans une paire de tourbillons

Ce chapitre est constitué d'un article en prépartion pour une soumission à *Journal of Fluid Mechanics*, abordant, de manière expérimentale, l'instabilité elliptique de paires de tourbillons avec écoulement axial.

Abstract

In this paper, we present results from an experimental study of the dynamics of pairs of vortices, whose axial velocity in the cores differs from the one of the surrounding fluid. Co- and counter-rotating vortex pairs at moderate Reynolds numbers were generated in a water channel, at the tips of two rectangular wings. Measurements of the three-dimensional velocity fields by means of stereoscopic Particle Image Velocimetry revealed a significant axial velocity deficit in their cores. For counter-rotating pairs, the long-wavelength Crow instability, involving symmetric wavy displacements of the vortices, could be clearly observed using dye visualisations. Measurements of the axial wavelength and growth rate of the unstable perturbation were found to be in good agreement with theoretical predictions, when the full experimentally measured velocity profile of the vortices, including axial flow, is taken into account. The dye visualisations further revealed the existence of a short-wavelength core instability. High-speed video recordings and Proper Orthogonal Decomposition of the visualisation time series allowed a precise characterisation of the instability mode, which involves perturbations of azimuthal wave number $m = 2$, as well as an axisymmetric wave ($m = 0$). These waves fulfill the resonance condition for the elliptic instability mechanism acting in strained vortical flows. A numerical three-dimensional stability analysis of the experimental vortex pair revealed the same unstable mode, and comparison of wavelengths and growth rates with the values obtained experimentally from dye visualisations shows good agreement. Pairs of co-rotating vortices evolve in the form of a double helix in the water channel. For flow configurations that do not lead to merging of the two vortices over the length of the test section, the same type of short-wave perturbations could be observed. Quantitative measurements of wavelength and growth rate, and comparison with previous theoretical predictions, again identify them as an elliptic instability mode. The short-wave instability modes for vortices with axial flow are different from the one previously found in

pairs without axial flow, which exhibits an azimuthal variation with wave number $m = 1$.

4.1 Introduction

The dynamics of a pair of vortices has been the object of a large number of studies in the last three decades, and with the development of new experimental techniques and increasing computer capabilities for numerical studies, the investigation of this flow has recently gained new impetus. The continued interest in this flow is, to a great extent, due to its relevance to the problem of aircraft trailing wakes, whose far field is primarily composed of a counter-rotating vortex pair. For large modern aircraft, these vortices can reach considerable strengths and represent a danger for following aircraft, especially smaller ones, due to the rolling moment and downwash they induce. Therefore, a need exists to alleviate this danger by accelerating the decay of the wake. One approach is to try to take advantage of the natural "cooperative" instabilities that can occur in a vortex system. To reach this goal, solid knowledge about the characteristics of the instabilities is needed. Numerous international projects, listed, *e.g.*, by Gerz, Holzäpfel & Darracq (2002), were developed to investigate the problem. In addition to this practical aspect, the vortex pair also represents one of the simplest flow configurations for the detailed study of elementary vortex interactions, which may yield useful information for the understanding of the dynamics of more complex transitional or turbulent flows.

The first cooperative instability to be discovered in a vortex pair is a long-wavelength wavy instability, that occurs in a counter-rotating vortex pair : the so-called Crow instability. It can be observed in the sky behind aircraft flying at high altitude, when the wake vortices are visualised by condensation (see, e.g., the photographs shown in Scorer & Davenport, 1970; Tombach, 1973; Jacob, 1995). Some laboratory observations can be found in Sarpkaya (1983); Liu (1992); Thomas & Auerbach (1994). The first theoretical analysis of this phenomenon was made by Crow (1970). He showed that the mutual interaction of the two vortices can lead to an amplification of displacement perturbations, whose axial wavelength is typically several times the initial vortex separation distance. The sinusoidal vortex displacements are symmetric with respect to the mid-plane between the two vortices, and they lie in planes inclined approximately at 45° with respect to the line joining the vortices. The origin of this instability is linked to the balance between the stabilising effect of self-induced rotation of the perturbations and the destabilising influence of the strain field that each vortex induces at the location of its neighbour. It was shown by Kelvin (1880), that a sinusoidal perturbation of a single vortex filament does not grow in time, but rotates around the vortex. In the presence of a second vortex, it can happen that the circumferential component of the velocity field induced by this vortex at the location of the first perturbed filament exactly cancels the self-induced rotation of the latter. The perturbation then remains in a stationary plane and is "pulled apart" by the radial component of the strain (which is also induced by the second vortex), leading to an exponential growth of its amplitude. A good description of this mechanism and its relation to Kelvin's waves can be found in Widnall, Bliss & Tsai (1974).

Many subsequent studies, mostly theoretical and numerical, have illustrated and completed the work of Crow (1970). In particular, the effects of axial flow and arbitrary (axisymmetric) vorticity distributions in the vortices on the stability characteristics were analysed by Moore & Saffman (1973), and Klein, Majda & Damodaran (1995). Extensions of Crow's analysis towards systems of more than two vortices, representative of the near or extended near wake behind a transport aircraft (possibly with various flap configurations), have also been carried out. The volume of papers in Crouch & Jacquin (2005), which follows the reviews by Spalart (1998), Rossow (1999) and Gerz *et al.* (2002), comprises several of these studies. Although numerical simulations (Rennich & Lele, 1997) seem to confirm the validity of Crow's theory quite closely in the early stages of the instability, a precise experimental verification is still lacking. The few quantitative results from experiments (Sarpkaya, 1983; Thomas & Auerbach, 1994; Devenport *et al.*, 1997), as well as observations from full-scale flight tests (Scorer & Davenport, 1970), show qualitative agreement with theoretical predictions. However, no closer comparison was made. In this paper, we try to compare Crow's inviscid theory with experimental results, concerning the wavelength and the growth rate of the long-wave instability in a pair of counter-rotating vortices with axial flow.

Short-wave instability, known as elliptic instability, is another cooperative instability that can be observed on a vortex subject to the influence of another one. Unlike Crow's instability, whose wavelength is about eight times the vortex separation distance (Crow, 1970), its typical wavelength scales with the radius of the vortex. It is called "elliptic instability" since it propagates on an elliptically deformed vortex. This instability can occur in counter-rotating as well as co-rotating configurations, contrary to Crow's instability which is inhibited by the rotation of the strain (Jimenez, 1975). Since the theory of Crow (1970) is based on the hypothesis of vortex filaments, which means that the vortices are considered as lines, Crow's work only applies for long-wavelength instability. A short-wavelength mechanism such as the elliptic instability has to be explained using different considerations. This was done by Moore & Saffman (1975) who analysed linearly the stability of a finite-core vortex (with a small axial flow), deformed elliptically by the presence of a strain field, in an attempt to explain the unstable vortex rings visualised by Widnall & Sullivan (1973). The same analysis was carried out by Tsai & Widnall (1976). They confirmed Widnall's proposed mechanism (Widnall *et al.*, 1974) and concluded that the strain could resonate with two (neutral) Kelvin modes of the vortex, and lead to the exponential growth of a perturbation : the mechanism of the elliptic instability was discovered.

Later on, the numerical simulations of Pierrehumbert (1986) and the Floquet analysis of Bayly (1986) pulled the elliptic instability back into light. They showed that a two-dimensional inviscid flow with elliptical streamlines is unstable with respect to three-dimensional perturbations, in the short-wavelength limit. Landman & Saffman (1987) extended these results to viscous flows, arguing that the presence of viscosity imposes a minimum wavelength for the unstable perturbation.Waleffe (1990) linked the inertial wave approach to the Kelvin mode approach. He analysed the stability of a rotating flow in an ellitiptical container and showed that a combination of plane waves can lead to localised disturbances whose growth rates match with those given by the unbounded theory.

An overall picture of the elliptical instability was given in the review of Kers-

well (2002). Concerning vortex pairs, the review mostly recalled theoretical and numerical work. Surprisingly, before the results of Leweke & Williamson (1998) who studied the elliptic instability in a pair of counter-rotating vortices, very few quantitative comparisons between predictions and experimental results had been performed. On vortex rings, impressively precise short-wave instability visualisations were presented by Krutzsch (1939).They show that the centre line of the vortex is displaced in the direction opposite to the direction of displacement of peripheral streamlines. This is typical of the elliptic instability in a pair of vortices without axial flow. A short-wave instability was also observed by Maxworthy (1972) and Widnall & Sullivan (1973). Malkus (1989) explored the nonlinear aspects of the instability in an elliptic flow bounded by an elliptical rotating cylinder. Using the same setup, Eloy, Le Gal & Le Dizès (2000) confirmed some elements of the theory presented by Waleffe (1990). Lacaze, Le Gal & Le Dizès (2004, 2005*b*) extended these results to the flow inside an elliptically deformed rotating sphere.

Thomas & Auerbach (1994) generated two parallel asymmetric vortices by rotating a sharp edge plate in a water tank. On top of the long-wave instability described by Crow (1970), they were able to visualise a short-wave instability, though the theoretical prediction of Widnall *et al.* (1974) did not seem to match the experimental results. A more rigorous and precise study carried out by Leweke & Williamson (1998) on the same vortex system, lead to an unambiguous conclusion : the experimental wavelength and growthrate of the short-wave instability observed are in agreement with the theoretical predictions of Tsai & Widnall (1976) and Waleffe (1990). This work was extended by Meunier & Leweke (2001, 2005) to co-rotating vortices. Numerical work of Billant, Brancher & Chomaz (1999) and Laporte & Corjon (2000) confirmed the conclusions of Leweke & Williamson (1998). So far, the theoretical predictions concerned uniform elliptical vortices (Waleffe, 1990). To extend the results to more realistic configurations, Le Dizès & Laporte (2002) obtained an expression for the growthrate of the elliptic instability in a pair of co- and counter-rotating Gaussian vortices, depending on global parameters of the flow. They validated their results by Direct Normal Simulations (DNS) and Large-Eddy Simulations. They identified unstable bands corresponding to different axial wavenumber ranges. Each band is due to the resonance of the strain field (induced by the other vortex) with two Kelvin modes[1] for which the azimuthal wavenumber m and the frequency ω are such that $m = \pm 1$ and $\omega = 0$. This is in agreement with the experimental investigations of Leweke & Williamson (1998) and Meunier & Leweke (2001), and the numerical work of Sipp & Jacquin (2003). Some studies (see, *e.g.*, Fabre, 2002; Fabre & Jacquin, 2004*a*) characterised the short-wave instability on vortices more representative of aircraft wakes.

All previous studies were performed on vortices without axial flow, except the early study of Moore & Saffman (1975). The first step to fill this gap was taken by Fabre, Cossu & Jacquin (2000), who discused the convective and absolute aspect of the instability on a pair of Rankine vortices in a uniform axial flow field, subject to a weak strain. Lacaze, Birbaud & Le Dizès (2005*a*) analysed the stability of a Rankine vortex with an axial velocity core in a stationnary strain.

[1]Though the denomination "Kelvin modes" (Kelvin, 1880) strictly applies to the inviscid normal modes associated with the rotation of the fluid in a stable vortex, we also use the terminology in the viscous case, as frequently done in the literature.

They discovered that, contrary to the case without axial flow, some Kelvin modes with high azimuthal symmetry orders and non-zero frequencies, could resonate, leading to the instability of the system. The same conclusions were drawn for a Gaussian vortex by Lacaze, Ryan & Le Dizès (2007). For parallel vortices, this corresponds to the counter-rotating case. Recently, these results were numerically extended to the co-rotating case by Roy, Schaeffer, Le Dizès & Thompson (2008*b*).

Experimental references concerning the elliptic instability in a vortex with axial flow are rare. Some visualisations of a short wave phenomenon in the wake of an aircraft can be found in Scorer & Davenport (1970), Jacob (1995) and Bristol *et al.* (2004). Similar observations were reported by Chen, Jacob & Savaş (1999) and Ortega, Bristol & Savaş (2003) who studied a four-vortex system generated by a flapped wing in a towing tank. The only quantitative data were presented by Devenport, Zsoldos & Vogel (1997) and Devenport, Vogel & Zsoldos (1999). They investigated counter- and co-rotating vortices generated by two symmetrical wings in a wind-tunnel. Some peaks in the velocity spectrum measured by hot-wire anemometry seem to be related to the elliptic instability.

In this paper, results are presented concerning experimental co- and counter-rotating vortex pairs with axial flow, that prove the presence of the elliptic instability. In particular, we analyse the spatio-temporal structure of a short-wavelength perturbation and relate this to the elliptic instability. More specifically, the axial wavelength, the azimuthal wavenumber and the growthrate of the unstable mode are obtained experimentally for a pair of counter-rotating vortices and compared with numerical results. First results of this study can be found in Roy *et al.* (2008*a*). The spatial characteristics of the unstable mode observed on a co-rotating pair are also given and compared to numerical predictions.

4.2 Experimental setup

4.2.1 Facility

The facility used for the experiments is a recirculating water channel with a free surface. It has a test section of dimensions 37 cm (width) $\times$ 50 cm (height) $\times$ 150 cm (length). The free–stream velocity U_∞ can be chosen in the range 5–100 cm/s. The turbulence intensities associated with the streamwise and transverse velocity components are approximately 1.5% and 0.6%, respectively. The bottom and side walls of the test section are made out of glass. An additional glass window downstream of the test section on the wall normal to the stream allows visual access to the flow inside the test section from five different directions. A schematic of the test section is shown in figure 4.1.

4.2.2 Vortex generating wings

Two NACA0012 rectangular half-wings with a chord $c = 10$ cm made of polyvinyl chloride, were placed tip to tip in the free–stream of the water channel. They had a round tip with a varying tip diameter equal to the local thickness of the wing. The wings were mounted vertically at the upstream end of the test section. The first half-wing, with a 15 cm span, was fixed on a U-frame positionned along the side and bottom boundaries of the channel. It was possible to change the angle

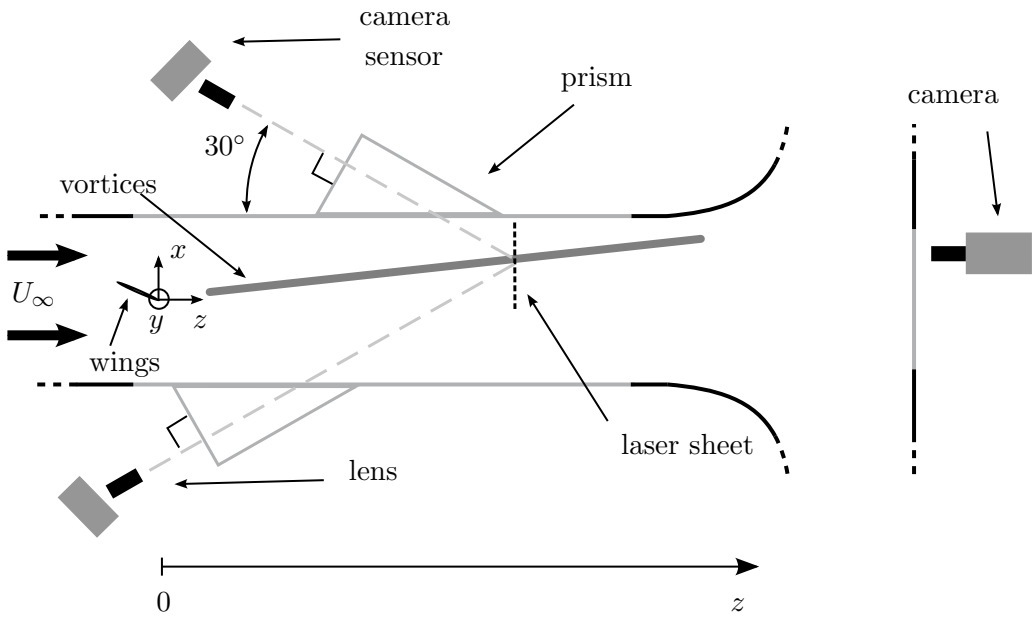

FIG. 4.1 – Top view of the water channel test section showing the stereo-PIV setup in a counter-rotating configuration. The tilt angle between the camera sensor and the lens is exaggerated to point out the use of a Scheimpflug mount.

of attack of both wings. The second wing was fixed to a support outside the water, and traversed the free surface. The setup is illustrated in figure 4.2(a). A similar kind of setup was used by Devenport *et al.* (1997, 1999).

When a rectangular wing is placed in a uniform stream, it is now well known that a "wing-tip" vortex is generated (see, *e.g.*, Mason & Marchman, 1972; Baker, Barker, Bofah & Saffman, 1974; Thompson, 1975; Singh & Uberoi, 1976; Katz & Bueno Galdo, 1989; Green & Acosta, 1991; Devenport, Rife, Liapis & Follin, 1996). The sign of the circulation depends on the sign of the angle of attack of the wing. With one vortex being generated by each wing, one can generate a counter- or co-rotating vortex pair by imposing independently the angle of attack of both wings. Another advantage of this setup, compared to, *e.g.*, a flapped wing, is the possibility to translate the top wing along its span axis. The spanwise position of the vortex is close to the wing-tip and mostly depends on the wing-tip shape (Hoerner, 1965). Therefore, translating the top wing implies changing the separation distance b between the two vortices. The three degrees of freedom of the setup were widely utilised in the exploration phase of the study, the aim being to find an unstable flow, exhibiting the elliptic instability. The origin O of the frame of reference $\{O, x, y, z\}$ chosen for our study is the middle point of the line linking the wing tips. The z axis points in the free–stream direction and the y axis is parallel to the vertical direction, pointing up. The orthonormal frame is completed by the x axis in the horizontal transverse direction.

4.2.3 Flow visualisation

A dye injection system allowed the visualisation of the vortices. A small pipe network was machined inside the U-frame and the wings to allow the injection of

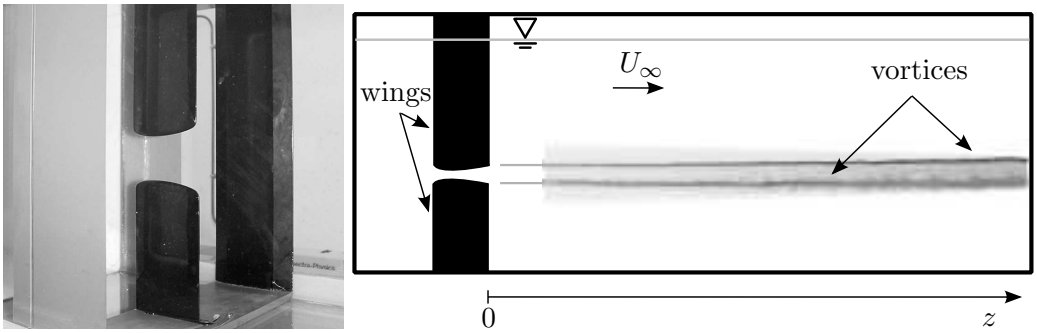

FIG. 4.2 – (a) Photo of the two half-wings in the water channel. (b) Side view of the water channel test section, showing the wings and the resulting vortices in a counter-rotating configuration.

fluorescent dye (aqueous solution of fluorescein). The injection holes were located close to the wing tip. Different injection holes were available ; depending on the configuration of the wings, the most appropriate ones were selected. The injection was ensured by a pressure difference. Special care was taken to make sure that this did not perturb the flow.

The dye injected in the flow was illuminated in volume by an argon ion laser (model Stabilite 2017 from Spectra Physics) coupled to an optical fibre with a spherical lens. The laser was oriented in the axis of the vortices through the downstream visualisation window presented in figure 4.1. Side view photos of the vortices were taken with a camera (Nikon D200) looking through the side walls of the channel test section. When a high acquisition frame rate was needed, a monochrome high-speed video camera (Vision Research Phantom V5) was used. Some visualisations of the vortices were taken in a plane normal to the free–stream. In that case, the optical fibre was coupled to a cylindrical lens, the resulting laser sheet being oriented from bottom to top. The D200 or Phantom camera was then looking through the downstream visualisation window.

4.2.4 Velocity measurements

All velocity measurements were made using stereoscopic particle image velocimetry (Stereo-PIV). This technique allows the measurement of three velocity components in a plane. Successful implementations of this method are presented, *e.g.*, by Willert (1997), Alkislar, Krothapali & Lourenco (2003) and Carlier & Stanislas (2005). A Nd-YAG pulsed laser was positioned underneath the test section, at the desired distance from the wing, generating a 3 mm thick vertical light sheet (see figure 4.1). The flow was seeded with silver-coated particles (Dantec), whose size (100 μm diameter) was small compared to the characteristic scale of the vortex (diameter typically of the order of 1 cm). Pictures of the particles in the laser sheet were taken with two high-resolution digital cameras (Roper Redlake, 4000 pixels $\times$ 2672 pixels). Each camera was placed on one side of the test section (see figure 4.1), viewing the laser plane in a direction forming a 30° angle with the free–stream. The camera sensor and the lens were mounted in a Scheimpflug setup (Scheimpflug, 1904). To conserve the orthogonality between the cameras' line of sight and the air-liquid interface, water-filled glass prisms were fixed on

the test section side walls (see figure 4.1). This reduces the distortion entailed by the non-orthogonal angle of sight. In addition, the small gaps between the prisms and the channel side walls were filled with water to alleviate the reflection of the light at the air-glass interfaces. An overview of the Stereo-PIV technique coupled with the use of prisms and Scheimpflug mounts can be found in Prasad & Jensen (1995) and Zang & Prasad (1997). The computing algorithm used to process the images is based on a two–dimensional cross–correlation PIV code developed by Meunier & Leweke (2003), which was successfully used in previous experimental studies on vortex flows (see, *e.g.*, Meunier & Leweke, 2005; Boulanger, Meunier & Le Dizès, 2007, 2008).

4.2.5 Parameters of the flow

For each vortex, a Reynolds number Γ/ν, based on the total circulation, is defined. Another parameter is the non-dimensional core size a/b, where a is the vorticity radius (defined later) and b the vortex separation distance. a/b gives a measure of the interactions between the vortices. The axial flow parameter $W_0 = (U_0 - U\infty)2\pi a/\Gamma$, where U_0 is the axial velocity at the centre of the vortex and U_∞ is the free–stream velocity, compares the axial velocity defect on the vortex axis with a characteristic azimuthal velocity. We also introduce a_w/a, the ratio between the radial scale a_w of the axial velocity profile and the core radius a.

4.3 Counter-rotating vortex pair

In this part, we focus on the three-dimensional instabilities of a pair of counter-rotating vortices. After an exploration of different parameter ranges, one configuration was chosen for a more detailed analysis. First, we describe the experimental base flow measured in the water channel with the Stereo-PIV technique. After a brief analysis of the long-wavelength Crow instability, we present visualisations of a short-wavelength instability mode of the vortices. In order to make the link between this observation and the elliptic instability theory, we estimate the growthrate, the wavelength, and the azimuthal wavenumber of the observed instability mode. Visualisations and Proper Orthogonal Decomposition (POD) techniques are used to extract the spatial structure and the temporal dependence of the instability mode. These data are compared with results of a numerical stability analysis of the experimental base flow.

4.3.1 Three-dimensional base flow

The wings were positioned in the counter-rotating configuration, in the middle of the water channel section. Both angles of attack were equal to 8.5°. The wing tips were 3 cm apart. The free–stream, approximately equal to 56 cm/s (see below). Two vortices were generated at the wing tips. The top vortex circulation was positive so that the vortex pair translated in the positive y direction by mutual induction. In the following, indices 1 and 2 refer to the top and bottom vortices, respectively. Stereo-PIV measurements were performed in two planes normal to the axis of the water channel, located at $z/c = 5.6$ and $z/c = 9.4$. For each plane,

300 three-dimensional velocity fields were obtained using the procedure described in 4.2.4.

The mean axial vorticity (ζ) and axial velocity (U) distributions at $z/c = 5.6$ are presented in figure 4.3. The axial velocity field presents a large deficit in the vicinity of the vortices. Residuals of the velocity defects behind the main parts of the wings can also be identified, to the left of the vortex cores. Driven by their respective vortices, the wake of the two half-wings is advected in the vicinity of the middle of the vortex pair. The axial velocity distribution in the vortex core is therefore strongly non-axisymmetric. This fact is reinforced by the presence of a small axial velocity excess located about 1 cm away from the top vortex, in the top-left direction (see figure 4.3). A small symmetrical decrease of the axial velocity can be observed close to the bottom vortex, which is difficult to explain. Though the axial velocity fields presented by Devenport *et al.* (1997), who used the same half-wing setup in a wind-tunnel, did not exhibit any velocity excess, a rapid increase of the axial velocity can be found in approximately the same position relatively to the vortex pair.

The stretching direction of the average axial velocity distribution in the vortex cores is approximately normal to the stretching direction of the average axial vorticity distribution, shown in figure 4.3).The elongation of the time-averaged vorticity distribution is mainly due to the motion of the vortices in time, in a preferred direction. To characterise this motion, the location of the vortices was determined for each of the 300 individual fields at $z/c = 5.6$ and $z/c = 9.4$. This was done by fitting the measured two–dimensional velocity field with the two–dimensional field of a pair of axisymmetric counter-rotating Gaussian vortices. The free parameters of this fit were, for each vortex, the total circulation, the Gaussian radius and the coordinates of the vortex centres in the (O, x, y) plane. In order to characterise the vortex motion, the eigenvalues a_M^2 and a_m^2 ($a_M > a_m$) of the covariance matrix of the vortex positions were computed. The eigenvector corresponding to a_M^2 is the direction in which the variance of the vortex position projection is maximised. The normal direction minimises the variance a_m^2. Physically, the direction corresponding to the a_M eigenvector is the preferred direction of motion of the vortex. We can illustrate this graphically by an ellipse centred on the average position of the vortex, of major and minor axes a_M and a_m, oriented accordingly to the respective eigenvectors. The preferred direction of motion is characterised by the angle α formed by the line joining the average positions of the vortices and the preferred direction of motion of one vortex (see figure 4.4). For each vortex, the values obtained for α, a_M and a_m are listed in table 4.1. Two physical mechanisms can explain the increase of a_m and a_M with z. The first one can be linked to the dynamics of a single vortex. The same trend was observed by Devenport *et al.* (1996) who used hot-wire anemometry to estimate the amplitude of the lateral motion of a single trailing vortex, the so-called "vortex meandering" (Roy & Leweke, 2008). This phenomenon, is currently not fully understood ; a probable explanation is related to transient growth of perturbations triggered by random external noise (Antkowiak & Brancher, 2004; Fontane *et al.*, 2008; Roy & Leweke, 2008). The development of the Crow instability is the second factor leading to an increase of a_M and a_m, as the amplitude of the long sinusoidal deformations of the vortices increases. This aspect of the flow is discussed in section 4.3.2. The mean separation distance b between the vortices increases by 10% bet-

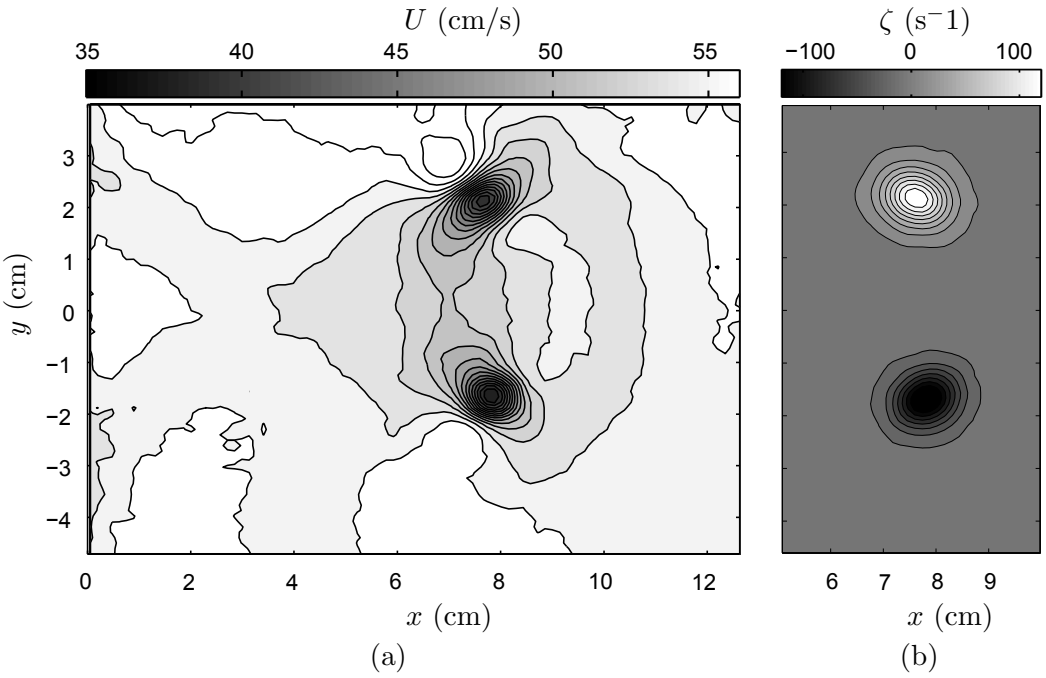

FIG. 4.3 – Average axial velocity U and axial vorticity ξ, for $z/c = 0.56$.

ween $z/c = 5.6$ and $z/c = 9.4$. The same trend was observed by Devenport *et al.* (1996).

The transverse displacement of the vortices due to vortex meandering and Crow instability has an effect on the fields presented in figure 4.3 : the size of the vortex cores are overestimated, especially in the preferred direction of motion, and the axial velocity in the centre of the vortices is underestimated. It is possible to minimise this effect by taking advantage of the knowledge of the vortex positions before averaging the fields. Each field is translated so that the centre of one vortex centre lies in its previously computed mean position, before averageing the fields. The operation is then repeated for the second vortex.

For each vortex, the total circulation Γ was estimated by integrating the velocity on a rectangular contour surrounding the vortex. The contour was chosen as large as possible to take into account as much vorticity as possible. One side of the contour was the centre line separating the two vortices. The values obtained show that the top vortex was stronger than the bottom vortex (see table 4.1). This difference in circulation entails a rotation of the pair around the vorticity centre. The point vortex model provides an estimation of the angular velocity of the vortex pair $(\Gamma_1 + \Gamma_2)/2\pi b^2 = 2.8°/\text{s}$ (computed for $b = 4$ cm) which is coherent with the experimentally determined value $3.1°/\text{s}$. The experimental translation velocity of the pair, 6.4 cm/s, is also in good agreement with the translation velocity $\Gamma/2\pi b = 6.2$ cm/s of two point vortices of opposite circulation $\Gamma = 157$ cm^2/s, with a separation distance $b = 4$ cm.

The vorticity profiles were evaluated by computing the azimuthal average of the mean vorticity field obtained by the recentering method described above. It was fitted with a Gaussian function

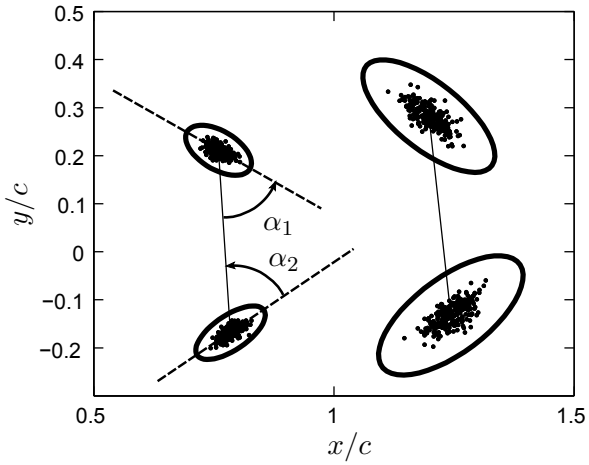

FIG. 4.4 – Vortex positions for $z/c = 5.6$ (left) and $z/c = 9.4$ (right). Each dot represents one position of the vortex extracted from one velocity field. A solid line links the mean positions of the top and bottom vortices. For each vortex, an ellipse of half-axes a_M and a_m (see table 4.1), oriented in the preferred direction of motion, is plotted. a_M and a_m are magnified by a factor of 5.

		$z/c = 5.6$		$z/c = 9.4$	
		top vortex	bottom vortex	top vortex	bottom vortex
α	°	55.5	59.6	45.1	59.4
a_m	cm	0.08	0.07	0.14	0.16
a_M	cm	0.15	0.17	0.33	0.36
Γ	cm^2/s	160	-155	160	-156
a	cm	0.56	0.54	0.60	0.61
b	cm	3.81		4.18	
a_w	cm	0.49	0.46	0.56	0.52
Γ/ν		17000	-16500	17000	-16700
a/b		0.147	0.142	0.143	0.146
a_w/a		0.88	0.85	0.93	0.85
W_0		-0.41	0.43	-0.47	0.49

TAB. 4.1 – Parameters of the base flow extracted from the Stereo-PIV measurements.

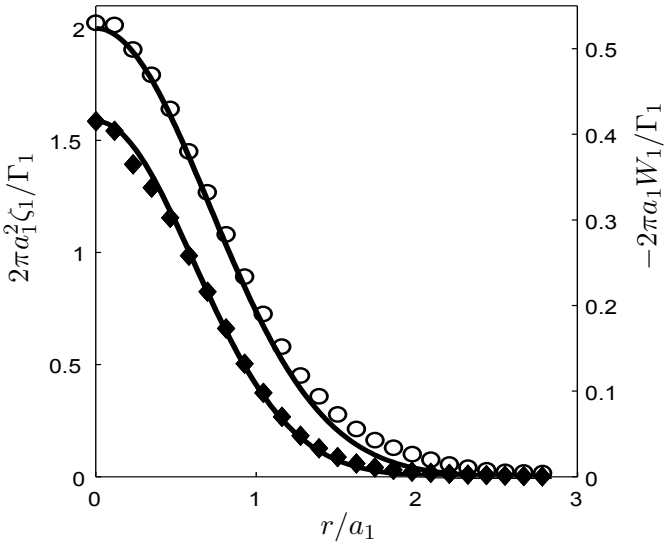

FIG. 4.5 – Azimuthally averaged vorticity ξ (circles) and axial velocity defect W (diamonds) profiles for the top vortex, at $z/c = 5.6$. The experimental data are fitted with Gaussian functions (solid lines).

$$\zeta(r) = \frac{\Gamma}{\pi a^2} \exp -r^2/a^2, \tag{4.1}$$

to extract a vorticity radius a. As shown in figure 4.5 for the top vortex (index 1), the Gaussian function matches well the experimental data. A slight local underestimation of the vorticity is only observed around the radial position $r/a = 1.8$. Since the circulation was imposed during the fit, it only implies a small error on the spatial distribution of the vorticity but the overall vorticity is correctly represented.

For each vortex, U_∞ is defined as the value of the axial velocity profile at $r/a = 3$. By subtracting U_∞ from the axisymmetric axial velocity profile, we define the axial velocity defect profile W. U_0 is the axial velocity at the centre of the vortex. As the vorticity, W is fitted to a Gaussian function (see relation (4.2) and figure 4.5), the axial velocity radius a_w being the only free parameter.

$$W(r) = U_0 \exp -r^2/a_w^2. \tag{4.2}$$

The match is excellent. The values of all vortex parameters are listed in table 4.1. We note an increase of the radius a much faster than what viscous diffusion would suggest at this Reynolds number. At $z/c = 9.4$, the flow is highly turbulent, subject to vortex meandering and Crow instability. In these conditions, the determination of the vortex centre in individual PIV measurements is subject to errors and uncertainties, which lead to a spurious broadening of the average fields, despite the use of the recentering method.

4.3.2 Crow instability

In this section, the long-wavelength instability occurring in a counter-rotating vortex pair is described, since it is a major characteristic of the investigated flow.

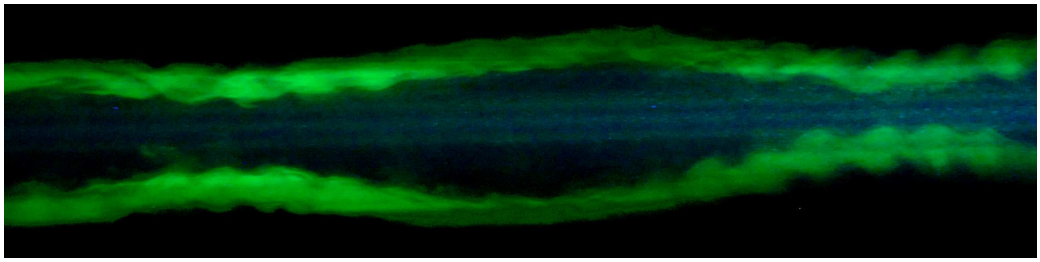

FIG. 4.6 – Visualisation of the Crow instability of a pair of counter-rotating vortices with axial core flow. The short-wavelength oscillation corresponding to the elliptic instability is also visible. The field viex is approximately 7 cm × 24 cm

Theoretical elements will be recalled and compared with the experimental results.

As shown by the visualisation presented in figure 4.6, the vortices are subject to the long-wavelength instability. This phenomenon was first analysed by Crow (1970). He considered two parallel line vortices of equal and opposite circulations, whose dynamics are determined by Biot-Savart induction. The velocity induced at a given point on one of the vortices can be split up into two main parts : (1) the flow field induced by the other vortex, where the corresponding Biot-Savart integral can be calculated in a straightforward way, and (2) the self-induced motion, which must be calculated using an appropriate cut-off length to avoid the divergence of the Biot-Savart integral. An arbitrary perturbation of the initially straight and parallel vortex lines can be decomposed into a set of normal modes, which consist of plane sinusoidal displacements parameterised by their axial wavelength λ_c, their orientation with respect to the line joining the initial vortices, and their symmetry : either symmetric with respect to the central plane of the pair, as exhibited by the mode in figures, or antisymmetric, whereby the perturbation of one vortex is shifted by half a wavelength in the axial direction compared to the corresponding symmetric mode.

The stability of these perturbations is governed by the interaction of three effects on a given vortex, which are all of the same order of magnitude. (1) The motion induced by the unperturbed other vortex. In the frame of reference moving with the vortex pair, the flow induced by one vortex at the location of the other unperturbed position is to first order a plane stagnation point flow, with maximum stretching in the 45° direction (Widnall *et al.*, 1974). (2) The motion induced by the *perturbations* of the other vortex. To first order, this also yields a linear flow field in the vicinity of the other vortex centre, but with a more complicated angular dependence. (3) The self-induced motion, which, for the kind of perturbations considered here, consists of a pure rotation of the perturbation plane (Kelvin, 1880) without growth of the amplitude, i.e., a third type of flow depending linearly on the spatial coordinates measured from the unperturbed given vortex position.

In the following, we concentrate on the symmetric perturbation modes of the vortex pair, since the anti-symmetric ones turn out to be stable. Following Crow (1970), an expression for the growth rate σ_c of the (symmetric) perturbations can be obtained, which depends on the wave number $k_c = 2\pi/\lambda_c$ of the modes (λ_c is the axial wavelength), and on the core radius a of the vortices. In this analysis, the vortices are essentially treated as filaments without internal structure, which allows

the use of Biot-Savart-type integrals to obtain the equations of motion for points on the vortices. The core radius enters in the evaluation of the self-induced velocity of each filament : it is related to the cut-off length to be used in the corresponding integral. The numerical relation between the two was established by considering a Rankine vortex model, i.e., vortices with constant vorticity inside a tube of radius a_e and zero vorticity outside (Crow, 1970). (It will be recalled below, from Widnall *et al.* (1971) and others, that, for the long-wavelength dynamics, a vortex with arbitrary vorticity distribution can always be replaced by a Rankine vortex with an "equivalent" core size a_e, which can be calculated).

The result for the non-dimensional growth rate $\sigma_c^* = \sigma_c \cdot (2\pi b^2/\Gamma)$ is

$$(\sigma_c^*)^2 = \left[1 - (k_c b)^2 K_o(k_c b) - k_c b\, K_1(k_c b) - \frac{\eta}{(a_e/b)^2}\right]\left[1 + k_c b\, K_1(k_c b) + \frac{\eta}{(a_e/b)^2}\right], \tag{4.3}$$

where the K_i $(i = 0, 1)$ are modified Bessel functions of the second kind and of order i. η is the self-induced angular velocity of a sinusoidally perturbed vortex filament, whose plane is known to rotate around the axis given by the unperturbed straight vortex. η is non-dimensional, it is normalised using the angular velocity of the fluid at the centre of the vortex, which is equal to half the vorticity there.

The exact dispersion relation for all for sinusoidal displacement perturbations of azimuthal wave number $m = 1$ (often also called "bending wave") of a Rankine vortex can be deduced from Kelvin's (1880) original work. It is a solution of the following implicit equation :

$$\frac{1}{\beta a_e}\frac{J_1'(\beta a_e)}{J_1(\beta a_e)} + \frac{1}{k_c a_e}\left[\frac{K_1'(k_c a_e)}{K_1(k_c a_e)} + \frac{\sqrt{\beta^2 + k_c^2}}{\beta^2}\right] = 0, \tag{4.4}$$

where J_1 is the Bessel function of the first kind, and K_1 the modified Bessel function of the second kind, both of order 1. The prime ($'$) denotes a derivative, and the parameter β is related to the rotation rate through

$$\eta = 1 - \frac{2k_c}{\sqrt{\beta^2 + k_c^2}}. \tag{4.5}$$

In practice, for a given $k_c a_e$, (4.4) is solved numerically for βa_e, and $\eta(k_c a_e)$ is found by (4.5). Due to the oscillatory nature of J_1, equation (4.4) is verified for an infinity of values βa_e for each $k_c a_e$. The pure displacement perturbations considered here are associated with the one value verifying $0 < \beta a_e < j_1$, where $j_1 \approx 3.8317$ is the smallest root of J_1. The other values represent more complicated perturbation modes with internal core deformations.

The self-induced dynamics of vortices with arbitrary (axisymmetric) velocity profiles was analysed by Widnall *et al.* (1971), and subsequently by Moore & Saffman (1973), Leibovich *et al.* (1986), and Klein & Knio (1995), in the limit of long wavelengths. It can be deduced from this work that a vortex with azimuthal and axial velocity distributions $v_\phi(r)$ and $v_z(r)$ evolving on a characteristic radial scale a, exhibits the same self-induced dynamics as an equivalent Rankine vortex, having the same circulation Γ and a core radius

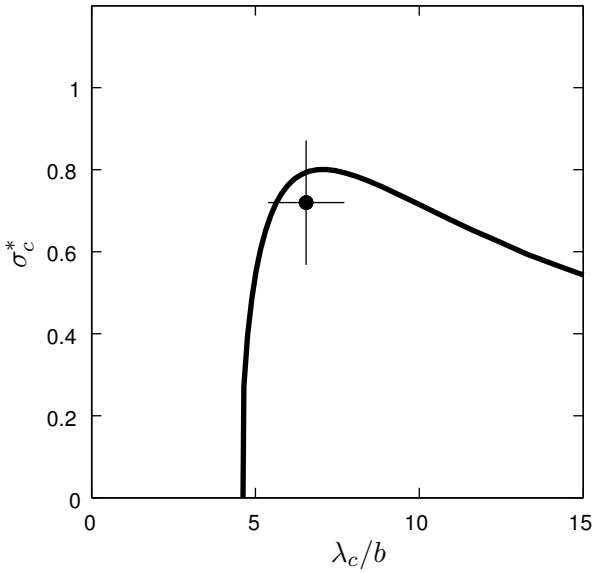

FIG. 4.7 – Growthrate of Crow instability as function of wavelength. The solid line is the theoretical growthrate σ_c, evaluated with (4.3). The dot is the experimental result.

$$a_e = a \cdot \exp\left[\frac{1}{4} - A + C\right]. \tag{4.6}$$

A and C are integral parameters characterising the velocity profiles; they are given by

$$A = \lim_{r\to\infty}\left[\frac{4\pi^2}{\Gamma^2}\int_0^r \overline{r}v_\phi^2(\overline{r})d\overline{r} - \ln\frac{r}{a}\right], \tag{4.7}$$

$$C = \frac{8\pi^2}{\Gamma^2}\int_0^\infty \overline{r}v_z^2(\overline{r})d\overline{r}. \tag{4.8}$$

Using the Gaussian functions modelling the top vortex profiles, we can theoretically determine A and C for the top vortex by means of (4.7) and (4.8). Numerically, we obtain $A_1 \approx -0.0580$ and $C_1 \approx 0.0639$. Therefore,

$$a_e \approx 1.4575a. \tag{4.9}$$

Using (4.3)–(4.5), we can obtain a prediction for the growthrate of the long-wavelength instability in our pair of counter-rotating vortices.

The experimental wavelength λ_c was measured by taking the average of 200 measurements on visualisations obtained at $z/c = 9.2$. We find $\lambda_c/b = 6.55$, with an standard deviation of 0.6. An estimation of the experimental growthrate σ_c can be obtained by comparing the amplitude of a_M for the top vortex, between $z/c = 5.6$ and $z/c = 9.4$, with an estimated uncertainly of $\pm 20\%$. Experimentally, we find

$$\begin{array}{l}\lambda_c/b = 6.55 \pm 0.60 \\ \sigma_c^* = 0.72 \pm 0.14\end{array} \text{ (experimental)}. \tag{4.10}$$

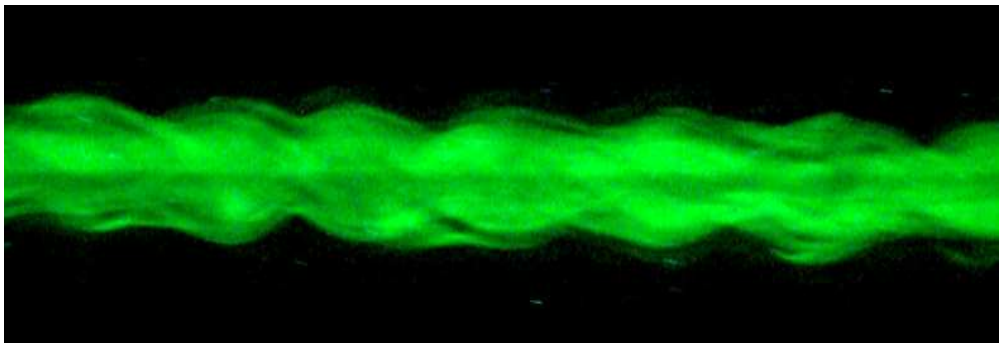

(a)

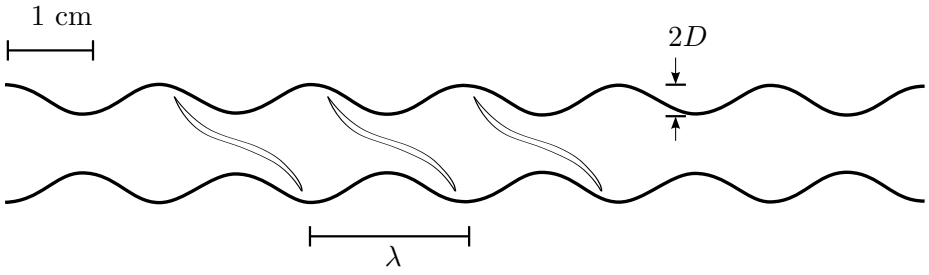

(b)

FIG. 4.8 – (a) Visualisation of the elliptic instability on the top vortex vortex. (b) Schematic showing the characteristic scales.

Figure 4.7 compares the theoretical prediction with the experimental measurement. The agreement between the two results is very good. The theoretical maximum growth rate and corresponding wavelength, determined from (4.3), are :

$$\begin{matrix} \frac{\lambda_c}{b} = 7.07 \\ \sigma_c^* = 0.80 \end{matrix} \text{ (theoretical).} \tag{4.11}$$

4.3.3 Elliptic instability

Theoretical aspects

The theory of the elliptic instability is based on linear normal modes. Following this formalism, the perturbation mode velocity fields $\mathbf{u}'$ and pressure field p' are written as

$$(\mathbf{u}', p') = [\mathbf{u}(r), p(r)] \exp(ikz + im\theta - i\omega t), \tag{4.12}$$

where k and m are the axial and azimuthal wavenumbers and ω is the frequency. For the case of a Rankine vortex without axial flow, the linear normal modes solutions of the relevant dispersion relation $D(k, m, n) = 0$, are the so-called Kelvin modes. For each azimuthal wavenumber m, there exists an infinity of branches in the (k, ω) plane, that are solutions of the dispersion relation. To classify these branches, the label n is commonly used. It corresponds to the number of zeros of the radial velocity u_r, in the interval $0 < r < a$. Arendt, Fritts & Andreassen (1997) showed that Kelvin modes form a basis for the perturbations localised in the vortex core. This means that any perturbation in the core of a Rankine vortex can be expressed by a combination Kelvin modes. Moore & Saffman (1975) and

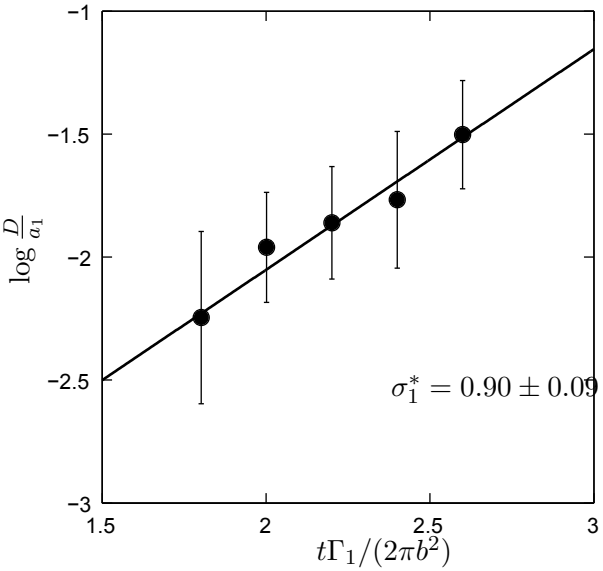

FIG. 4.9 – Amplitude of the oscillations measured for different streamwise position. The circles represent the experimental data. The linear regression symbolised by the solid line leads to the growthrate σ_1.

Tsai & Widnall (1976), who were not aware of this property, nevertheless used Kelvin modes to identify the mechanism of the elliptic instability. They studied a vortex with finite core size immersed in a weak strain field of second-order azimuthal symmetry. They showed that the strain field could resonate with two Kelvin modes of azimuthal wave numbers $m_1 = 1$ and $m_2 = -1$.

These results can be generalised for higher azimuthal wave numbers (Eloy & Le Dizès, 2001). The general resonance condition coupling the strain with two Kelvin modes with (k_1, m_1, ω_1) and (k_2, m_2, ω_2), reads :

$$\begin{pmatrix} k_1 \\ m_1 \\ \omega_1 \end{pmatrix} - \begin{pmatrix} k_2 \\ m_2 \\ \omega_2 \end{pmatrix} = \begin{pmatrix} 0 \\ 2 \\ 0 \end{pmatrix} \tag{4.13}$$

Two Kelvin waves can therefore resonate with the strain if their axial wavenumber and frequency are equal and their azimuthal wavenumbers differ by 2. Eloy & Le Dizès (2001) showed that for the case $m_1 = -1, m_2 = 1$, the growthrate is maximised when the labels n of the two Kelvin modes are equal. The instability mode is in this case called *principal* and can be identified by the triplet (m_1, m_2, n).

These results were later extended to vortices with continuous vorticity profiles. Le Dizès & Laporte (2002) give an expression for the growthrate in a pair of Gaussian vortices (co- and counter-rotating) without axial flow. They found that the most unstable modes are necessarily a combination of two Kelvin modes of azimuthal wavenumbers -1 and 1. This is coherent with the experimental results of Leweke & Williamson (1998) who studied the instability in a pair of counter-rotating vortices and observed an unstable periodic displacement of the vortex centres.

Lacaze *et al.* (2007) studied the instability of a Batchelor vortex in a stationary strain field. As for the counter-rotating case, they found that the triadic resonance

of the two Kelvin modes with the strain field was still leading to instability. Interestingly, they show that when the axial velocity amplitude increases, the $(-1, 1)$ modes get damped. There exists a value of the axial flow parameter W_0, above which the modes $(-1, 1)$ are not the most unstable. Instead, modes with a more complex spatial structure, such as $(-2, 0)$ can be observed.

Experimental observations

It can be seen in figure 4.6, that a short-wavelength core oscillation is present on top of the Crow instability. The aim of this part is to analyse in detail this perturbation. We focus here on the top vortex.

To observe the perturbation more closely, the laser beam was oriented in the upstream direction through the visualisation window (see figure 4.1). Fluorescein dye was injected into the top vortex and illuminated by the laser beam, and a camera was placed on the side of the test section, aiming at the vortex in the y direction. Figure 4.8(a) shows a periodic perturbation propagating on the top vortex. It is symmetric with respect to the axis of the vortex. The well-organised structure that can be seen in figure 4.8(a) was not observable on all frames. Only 80 frames (of 300 taken) could be analysed for $z/c = 9.0$ to extract a wavelength λ_1. Averaging the 30 values of the wavelengths measured, we obtain $\lambda_1 = 1.60$ cm with a standard deviation of 0.15 cm. The axial wavenumber $k_1 a_1 = 2.21 \pm 0.14$.

In order to estimate the growthrate of these short-wavelength oscillations, measurements of the amplitude D of the perturbation defined in figure 4.8(b), were performed at $z/c = 7.2$, 7.8, 8.4, 9.0 and 9.7, on the top vortex. At each streamwise position, 200 frames were recorded. 20 of them, showing the instability, were selected and processed. The growthrate σ_1 is then estimated by a linear regression, taking into account the 100 amplitudes measured (see figure 4.9). We find

$$\sigma_1^* = \sigma_1 \frac{2\pi b^2}{\Gamma_1} = 0.9 \pm 0.09, \tag{4.14}$$

with b and Γ_1 taking the value corresponding to $z/c = 5.6$ (see table 4.1). The uncertainty on the measurements of the amplitude D is high : typically, the standard deviation reaches 30% of the mean value. This is due to the fact that the Crow instability is fully developed at this downstream location, generating a high variance of the separation distance b. Nevertheless, the resulting uncertainty[2] of the growthrate σ_1 is only 7%.

To link these experimental results with a known instability mechanism, a linear stability analysis was performed numerically using the full–spectral code presented in Roy *et al.* (2008*b*). The base flow investigated was chosen to be very similar to the flow measured at $z/c = 5.6$. At this location, the roll-up phase of the vorticity sheet is terminated and the amplitude of Crow's instability and of vortex meandering are still reasonably small. The short-wavelength perturbation is not visible so close to the wings. However, the wavelength selction is expected to occur in this region. The base flow to be analysed was generated by solving the two–dimensional Navier–Stokes equations, starting from two axisymmetric vortices with Gaussian

[2]The evaluation of the uncertainty on the computation of σ_1^* results directly from the least square analysis. It is described, *e.g.*, by Taylor (1997).

	$z/c = 5.6$	numerical flow
a_1/b	0.147	0.147
a_2/b	0.142	0.147
a_{w1}/a_1	0.88	0.88
a_{w2}/a_2	0.85	0.88
Γ_1/ν	17000	16800
Γ_2/ν	-16500	-16800
W_{01}	-0.41	-0.41
W_{02}	0.43	0.41
$\sigma 2\pi b^2/\Gamma$	0.90	0.96
k_m	2.21	1.75

TAB. 4.2 – Parameters of the experimental and numerical flow.

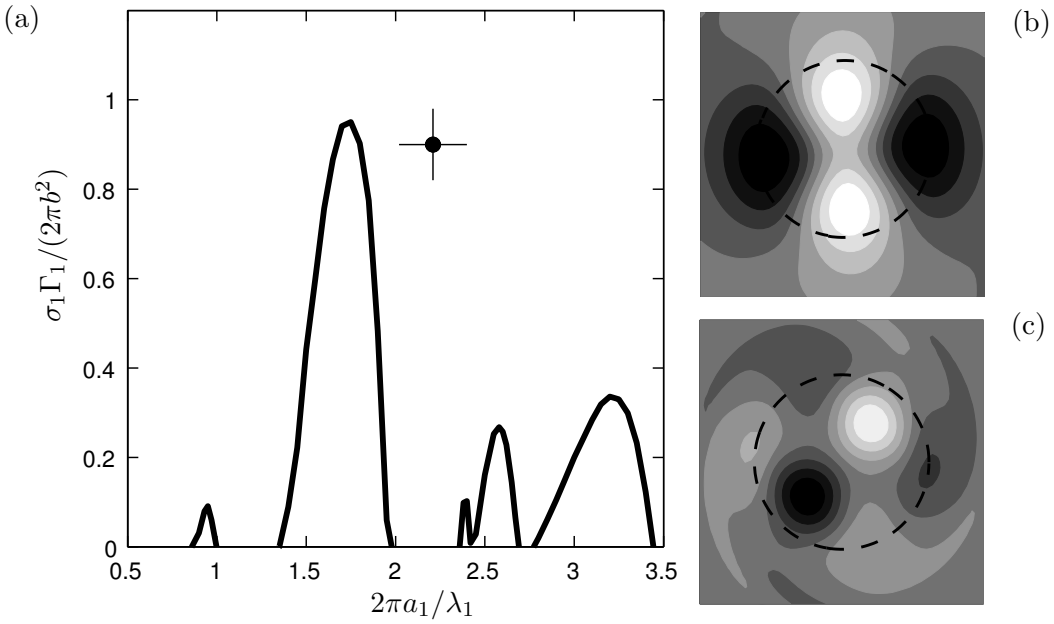

FIG. 4.10 – (a) Non-dimensional growthrate as function of axial wavenumber. The solid line represents the numerical result. The dot symbolises the experimental point. The mode structure corresponding to $k_1 a_1 = 1.75$ and 3.2 are presented in (b) and (c).

vorticity profiles and circulation Γ. After a short period of oscillation during which the vortices relax to adapt to their mutually induced strain, a quasi–steady mean state is reached (see Le Dizès & Verga, 2002). The flow obtained is a quasi–solution of Euler's equations. It is then possible to stop the diffusion process and perform a stability analysis of the flow with respect to the three-dimensional perturbations. The vorticity radius a of the flow is measured by fitting the velocity field with the two–dimensional velocity field of a pair of axisymmetric vortices. The axial velocity is introduced artificially by the relation

$$U_c(\theta, r) = W_0 \frac{\Gamma}{2\pi a} \left[\frac{\xi_c(\theta, r)}{\xi_c(0, 0)} \right]^{a^2/a_w^2}, \tag{4.15}$$

where $U_c(\theta, r)$ and $\xi_c(\theta, r)$ are the two–dimensional fields of axial vorticity and axial velocity in the cylindrical frame centred on each vortex. The parameters of the numerical base flow are presented in table 4.2. The numerical growthrate is plotted in figure 4.10(a) as function of axial wavenumber. The most unstable zone, located around $k_1 a_1 = 1.75$, corresponds to the elliptic instability. It was identified as the mode $(0, 2, 1)$ (see 4.3.3). The spatial structure of this mode is presented in figure 4.10(b). This unstable mode was theoretically predicted by Lacaze *et al.* (2007) in a pair of counter-rotating Gaussian vortices. The second–order azimuthal symmetry of this mode is coherent with the structure of the experimental perturbation observed, which is symmetric with respect to the vortex axis. The second most unstable zone, around $k_1 a_1 = 3.2$, has an azimuthal symmetry of the third order, as shown in 4.10(c), and is therefore not a candidate to match the visualisations. The difference between the non–dimensional wavenumber k_m corresponding to the largest growthrate and the experimental wavenumber $k_1 a_1$ is 20%. This discrepancy is most likely due to the difficulty of identifying the base flow responsible for the wavelength selection. Indeed, the wavelength of the instability is determined by the conditions corresponding to the early stages of the flow. Practically, this means that the location $z/c = 5.6$, at which the base flow was measured, might already be too far downstream of the wing. A more upstream position would yield a smaller vorticity radius a_1 (the radius between $z/c = 5.6$ and $z/c = 9.4$ increased by 7%). Also, considering the mode $(0, -2, 1)$ for $W_0 > 0$, k_m increases with $|W_0|$, as shown by Lacaze *et al.* (2007) and Roy *et al.* (2008*b*). Underestimating U_∞ would therefore lower the wavenumber. The value of the experimental growthrate matches correctly the numerical one, given the experimental uncertainty.

Further details of the spatial structure of the instability were obtained from a different set of visualisations, with a laser sheet oriented vertically, normal to the free–stream. Images of the top vortex were taken through the visualisation window presented in figure 4.1, in a direction normal to the laser sheet ; figure 4.11(a) shows an example. The Phantom high–speed camera was used to acquire 4000 frames at a rate of 300 Hz. The next step involved the so–called Proper Orthogonal Decomposition (POD) of this visualisation image series. Reviews of the POD method can be found in Berkooz, Holmes & Lumley (1993) and Liang, Lee, Lim, Lin, Lee & Wu (2002). A didactic approach is shown in Chatterjee (2000). In a previous study on the dynamics of a single wing tip vortex, it was shown that, concerning the qualitative spatial structure, POD of a series of dye

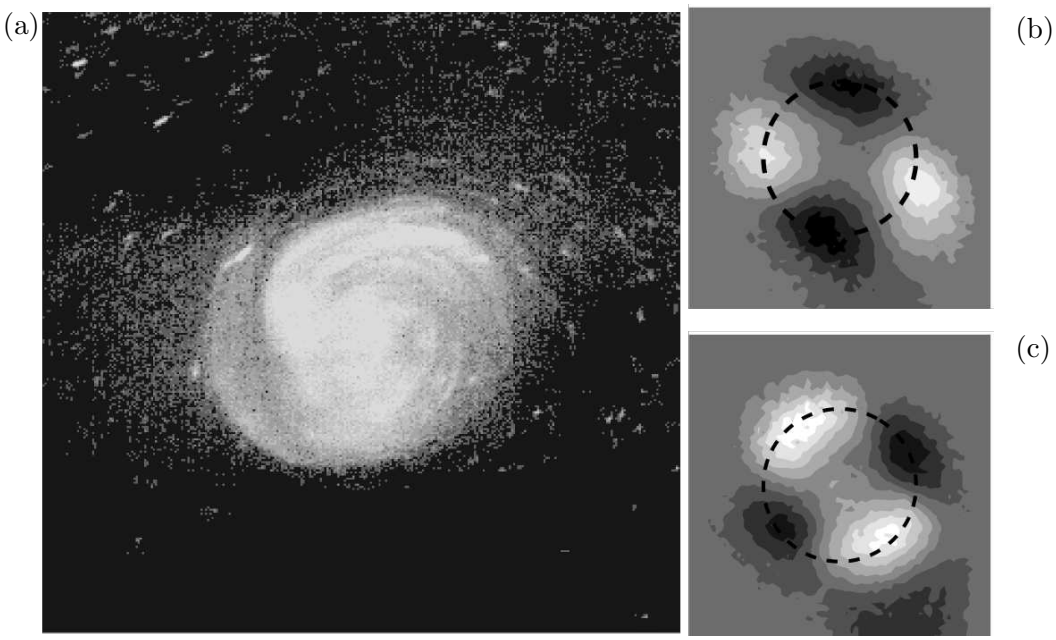

FIG. 4.11 – (a) Example of a visualisation used to perform the POD analysis on the light intensity. (b) Mode 5 and (c) mode 6 of the POD analysis. The dotted line is a circle of radius a_1.

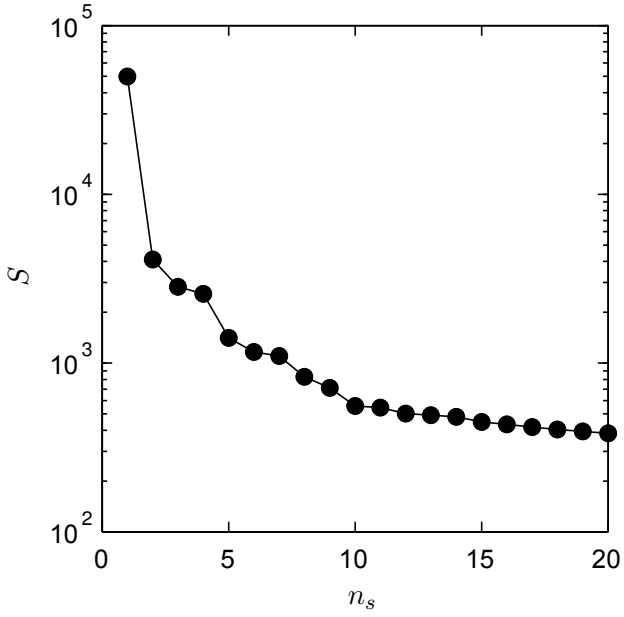

FIG. 4.12 – Singular values S computed from the light intensity of 4000 pictures of the top vortex.

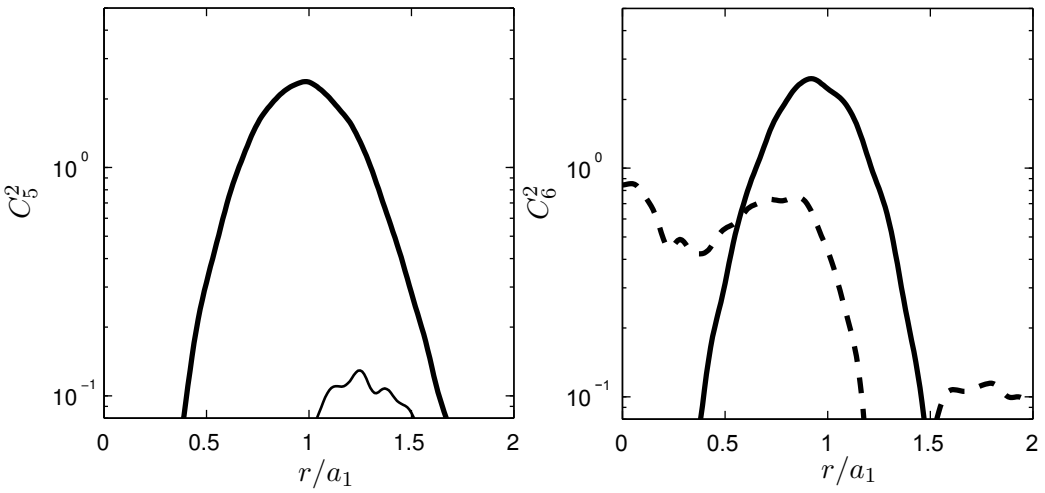

FIG. 4.13 – The squares of the Fourier coefficients C_5 and C_6 are plotted for mode 5 and 6, as a function of r. The solid, thin and dashed lines correspond to $m = 2$,$m = 3$ and $m = 0$. The other branches for which $m < 10$ are too weak to appear on the figures.

images gave identical results as a POD of vorticity fields, which is physically more relevant (Roy & Leweke, 2008, see also the Appendix). In the present study, the dye POD was used for its ease of implementation, in order to extract the mean features of the short–wave instability.

The method used for our decomposition can be explained as follows : the 8000 pixels of each frame were aligned to form one column of a matrix F. A singular value decomposition of F, which is of the form,

$$F = \tilde{U}\Sigma\tilde{V}, \tag{4.16}$$

was then performed. In equation (4.16), the diagonal elements S of Σ are the singular values of F, arranged in decreasing order. All other elements of Σ are zero. The columns of $\tilde{U}$ are the corresponding singular vectors. They are orthonormal and form a basis for the original frames. This basis is optimal in the least-square sense. For any integer $n_i \leq 4000$, it is not possible to find a basis in which the approximation of the frame series is better than the approximation with the first n_i singular vectors. We call n_s the rank of a singular value in the decreasing hierarchy. The first singular values of F are presented in figure 4.12[3], showing, as expected, a decrease of the variance (or energy) of the modes with increasing rank. For our study, we focus on the modes number 5 and 6, M_5 and M_6, whose singular values are approximately equal. They are presented on figure 4.11(b) and 4.11(c). A second-order azimuthal symmetry can be visually identified. To analyse precisely their azimuthal dependence, for each mode, a Fourier decomposition was accomplished on the azimuthal direction for each radial position r. For each value of the wavenumber $|m|$, we obtain the Fourier coefficients as functions of

[3]Since the POD was performed on the light intensity values, the units of the singular values presented in figure 4.12, as well as the Fourier coefficient and the power spectral densities presented in figures 4.13 and 4.15, are not physically relevant.

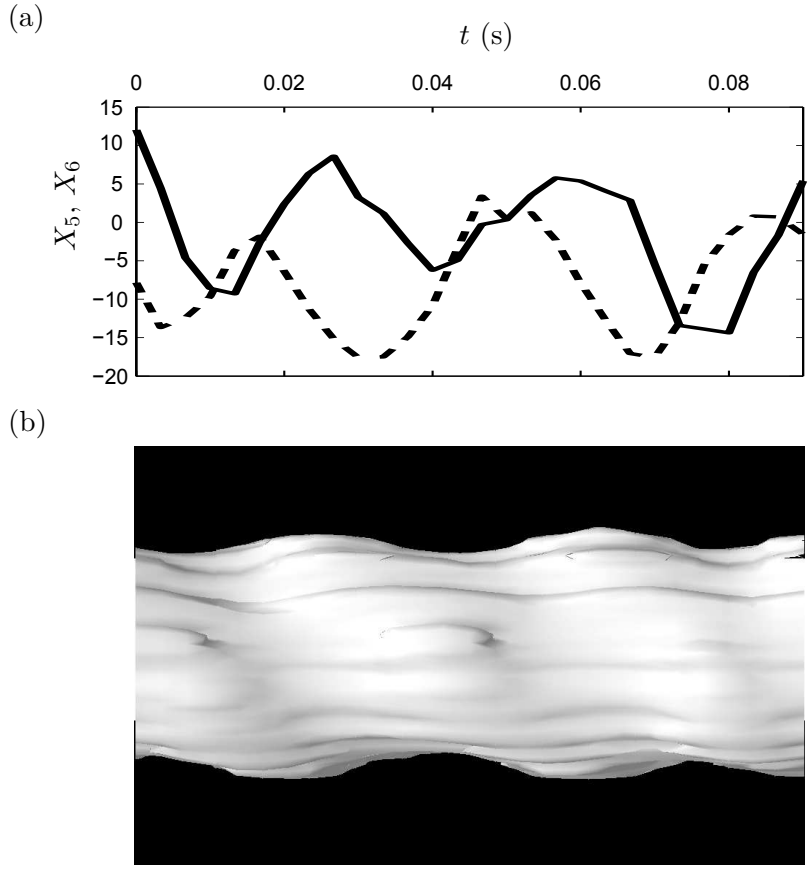

FIG. 4.14 – (a) Projection of the frames on the modes 5 (solid line) and 6 (dashed line). (b) Spatio-temporal reconstitution of the initial field using only the components of the mode 1, 5 and 6. One field corresponding to one instant, the spatio-temporal field is reconstituted by putting side by side the two–dimensional fields.

r. The results of these computations are shown in figure 4.13. In figure 4.13(a), since no other branch reaches the order of magnitude of the branch $|m| = 2$, M_5 can be considered as a pure spatial wave with an azimuthal wavenumber $|m| = 2$. Similarly, figure 4.13(b) shows two dominant branches at the highest order revealing the coupling of two spatial waves of azimuthal wavenumber $m = 0$ and $|m| = 2$. M_6 can therefore be considered as the superposition of two azimuthal waves. The presence of the $m = 0$ component is revealed in figure 4.11(c) by the amplitude at the centre that does not fall down to zero. We can write

$$M_5 = \hat{A}(r)\sin(2\theta + \phi_0) \tag{4.17a}$$

$$\tilde{M}_6 = M_6 - \hat{C}(r) = \hat{B}(r)\sin(2\theta + \phi_0 + 2\phi), \tag{4.17b}$$

where $\hat{A}$, $\hat{B}$ and $\hat{C}$ are radial functions and ϕ is the phase difference between M_5 and $\tilde{M}_6$, the $|m| = 2$ component of M_6.

We can show that a travelling wave $Y = \hat{Y}\sin(2\theta + \omega_f t)$ expressed in the (M_5, M_6) basis must read :

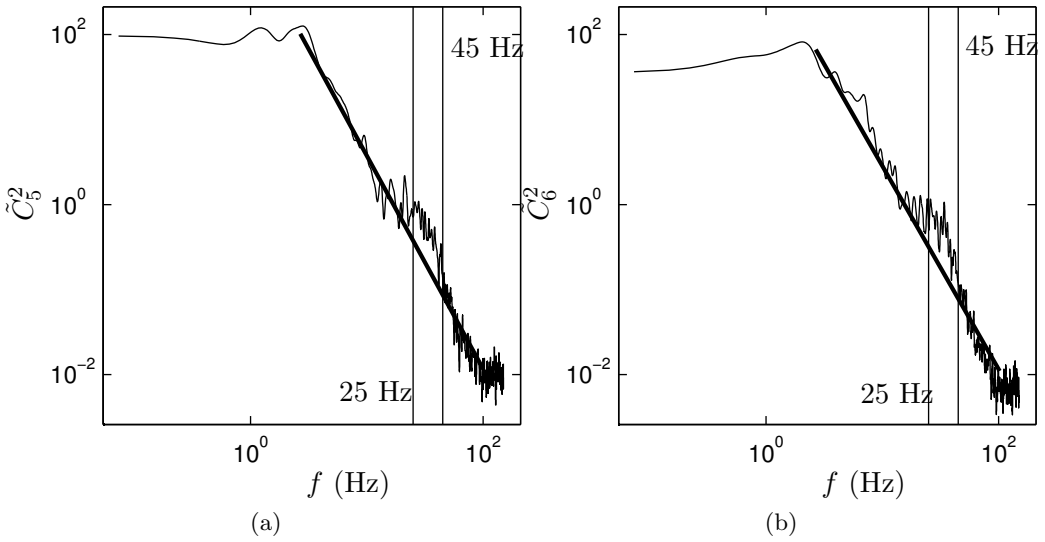

FIG. 4.15 – (a) Power spectral density P_5 of the coordinates of all the frames on mode 5. The solid line is a represent the average slope of P_5. The two vertical lines delimit a zone in which the distance between P_5 and the line of average slope is maximal. (b) Same as (a) on mode 6.

$$Y = \frac{\hat{Y}}{\hat{A}} \frac{\sin(-\phi_0 - \phi + \pi + \omega_f t)}{\sin(\phi)} M_5 + \frac{\hat{Y}}{\hat{B}} \frac{\sin(-\phi_0 + \omega t)}{\sin(\phi)} \tilde{M}_6 \tag{4.18}$$

In (4.18), the factors of M_5 and $\tilde{M}_6$ are the coordinates of Y. Experimentally, it is possible to extract the projection X_5 and X_6 of the frames on M_5 and M_6. This is illustrated in figure 4.14, for about 0.1 second. At the order, X_5 and X_6 can be seen as periodic, with a constant phase difference χ, a similar amplitude $\hat{X}$ and a zero mean-value. They can be approximately modeled by

$$X_5 = \hat{X}(r) \sin(\omega_f t + \chi_0) \tag{4.19a}$$

and

$$X_6 = \hat{X}(r) \sin(\omega_f t + \chi + \chi_0), \tag{4.19b}$$

According to equation (4.18), if X_5 and X_6 are to be associated with the coordinates of a travelling wave in the $(M_5, \tilde{M}_6)$ space, their relative phase difference must be such that $\chi = \phi \pm \pi$. Experimentally, we can measure the angular phase difference $\tilde{\phi}$ between M_5 and M_6 by a cross-correlation. We find $\tilde{\phi} = 45.00°$ so $\phi = 2\tilde{\phi} = 0.5\pi$. By measuring the temporal shift τ of X_6 relatively to X_5, and their period T, we obtain $\chi = 2 * \pi\tau/T = 0.58\pi$. Given the approximation on the measure of τ due to the low temporal resolution of X_5, we can conclude that X_5 and X_6 are good candidates to be the coordinates in $(M_5, \tilde{M}_6)$ of a spatio-temporal travelling wave. This is illustrated and confirmed by the figure 4.14(b). It shows the spatio-temporal reconstruction of the field formed by putting side by side the successive projections of the frames on the modes 1, 5 and 6. Mode 1 can be considered as the mean field composed by averaging all the light intensity of the frames. Figure 4.14(b) shows a double-helix structure, typical of a second-order azimuthal

symmetry wave. The $m = 0$ component of M_6 just adds a periodic axisymmetric deformation to the helix, hardly visible on figure 4.14(b). Using the correspondence between the vorticity and the light intensity of the frames demonstrated in the Appendix, we can extend these conclusions to the vorticity field. A physical interpertation can be to consider perturbation field of the total field presented in 4.14(b), as the superposition of two Kelvin modes of pulsation ω_f with different azimuthal wavenumbers $m = 0$ and $|m| = 2$.

We are now wish to make a link between these conclusions and the elliptic instability theory. A first step is to measure ω_f more accurately. To do so, a Fourier analysis of the coordinates, in (M_5, M_6), of all the frames acquired, is achieved. The corresponding power spectral densities P_5 and P_6 are plotted in figure 4.15. A low frequency peak can be clearly seen for P_5 and P_6. This is due to the Crow instability coupled with the meandering phenomenon. These two mechanisms impose a translation of the vortex that can be modeled by an $m = 1$ perturbation, but their high energetic levels also pollute the more complex modes. A frequency range of more interest is found between 25 Hz and 45 Hz. As can be seen in figure 4.15, it corresponds to the zone where the distance between P_5 and the linear approximation of P_5 in the middle range frequency, is maximal. The same applies to P_6. This gives the approximation $\omega_f/2\pi = (35 \pm 10)$ Hz. Non-dimensionalising by $2\pi b^2/\Gamma_1$, we find

$$90 < \omega_f^* < 160. \tag{4.20}$$

The non-dimensional pulsation of a spatial double-helix of wavelength λ_1, translating without any rotation at the velocity U_1 is equal to 135. This is the same order of magnitude as ω_f^*. It is consistant with the pulsation value obtained numerically which is one order smaller (see table 4.2). The spatio-temporal reconstruction presented in 4.14, can therefore be interprated as purely spatial by making the transformation $t \to -U_{\infty 1}t$. Since λ_1 is positive, we can then conclude on the positive sign of m by inspecting the angular velocity phase of the wave. The equivalent axial wavelength λ_f reads

$$\lambda_f = 2\pi U_{\infty 1}/\omega_f = 1.57, \tag{4.21}$$

which is very close (2%) to the value of λ_1 measured (1.60 cm).

We can now conclude on the identification of the elliptic instability in the present flow. We identified a periodic unstable perturbation. We decomposed this perturbation and showed that it was the result of the coupling of a spatial wave of azimuthal wavenumber $m = 2$ with an $m = 0$ (axisymmetric) wave. The difference between the two wavenumbers is equal to 2. This is typical of the elliptic instability (see 4.13). Despite a difference in the axial wavelength, the structure of the unstable mode as well as the growthrate we measured, are consistent with those of the most unstable mode obtained numerically by analysing the stability of the experimental base flow.

4.4 Co-rotating vortex pair

In this chapter, we investigate the stability of a co-rotating vortex pair with axial core flow. Such pairs were generated in the water channel by changing the sign

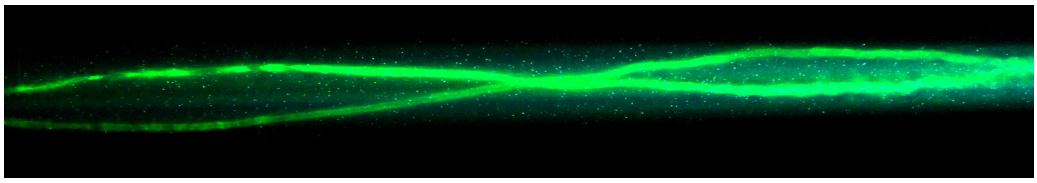

FIG. 4.16 – Side view of the co-rotating vortex pair. The field of view is approximately 8 cm × 50 cm.

of the angle of attack of one of the wings, with respect to the configuration used in the previous section. The values of free-stream velocity and angles of attack, as well as the relative position of the two airfoils, were varied until a short-wavelength perturbation could be observed on the vortices. One such configuration was then selected for a more detailed analysis. It consisted of the two wings being offset in the horizontal direction (x), with tips of their trailing edges located at the same vertical position (y). The angle of attack was 8° for both wings, and the tips were separated by 2.5 cm in the x-direction. The free-stream velocity was near 65 cm/s, resulting in a chord-based Reynolds number of about 70000.

4.4.1 Characteristics of the three-dimensional base flow

Figure 16 shows a side view of a dye visualisation of the co-rotating vortex pair. Mutual induction of the two vortices induces a rotation of the pair as it moves downstream (towards the right) in the channel, which produces the double helix configuration visible in figure 4.16.

Following the procedure described for the counter-rotating pair, 300 velocity fields were measured at $z/c = 9.0$, using Stereo-PIV. The same recentering method was used to remove the effect of the vortex motion on the time-averaged velocity fields. Figure 4.17 shows a reconstruction of the total mean field. For negative values of x (to the left of the middle plane), the fields were recentered relatively to the top vortex and then averaged. The same was made relatively to the bottom vortex to compute the rest of the field. Considering one vortex, the stretching direction of the average vorticity distribution follows approximately the principal direction of the strain field induced by the other vortex. Considering the axial velocity distribution, the stretching direction is governed by the main part of the wake of the wing, which spirals around the vortices. For each vortex, the total circulation was estimated by integrating the velocity field on a closed rectangular contour surrounding the vortex, as for the counter-rotating case. The vortices were found to be, to a good approximation, equal in strength.

To model the azimuthally averaged azimuthal velocity profile U_θ, contrary to the counter-rotating case, Gaussian functions did not lead to acceptable results. Instead, following the approach of Fabre & Jacquin (2004*a*), the measured profile U_θ was fitted to their VM2 vortex model, according to :

$$U_\theta = \frac{\Gamma}{2\pi} \frac{\rho_2^{\gamma-1}}{\rho_1^{\gamma+1}} \frac{r}{[1+(1/\rho_1)^4]^{(1+\gamma)/4}\,[1+(1/\rho_2)^4]^{(1-\gamma)/4}} \tag{4.22}$$

where ρ_1 and ρ_2 correspond to two different characteristic radii of the vortex. ρ_1 delimits the inner viscous core containing most of the vorticity, and ρ_2 defines the

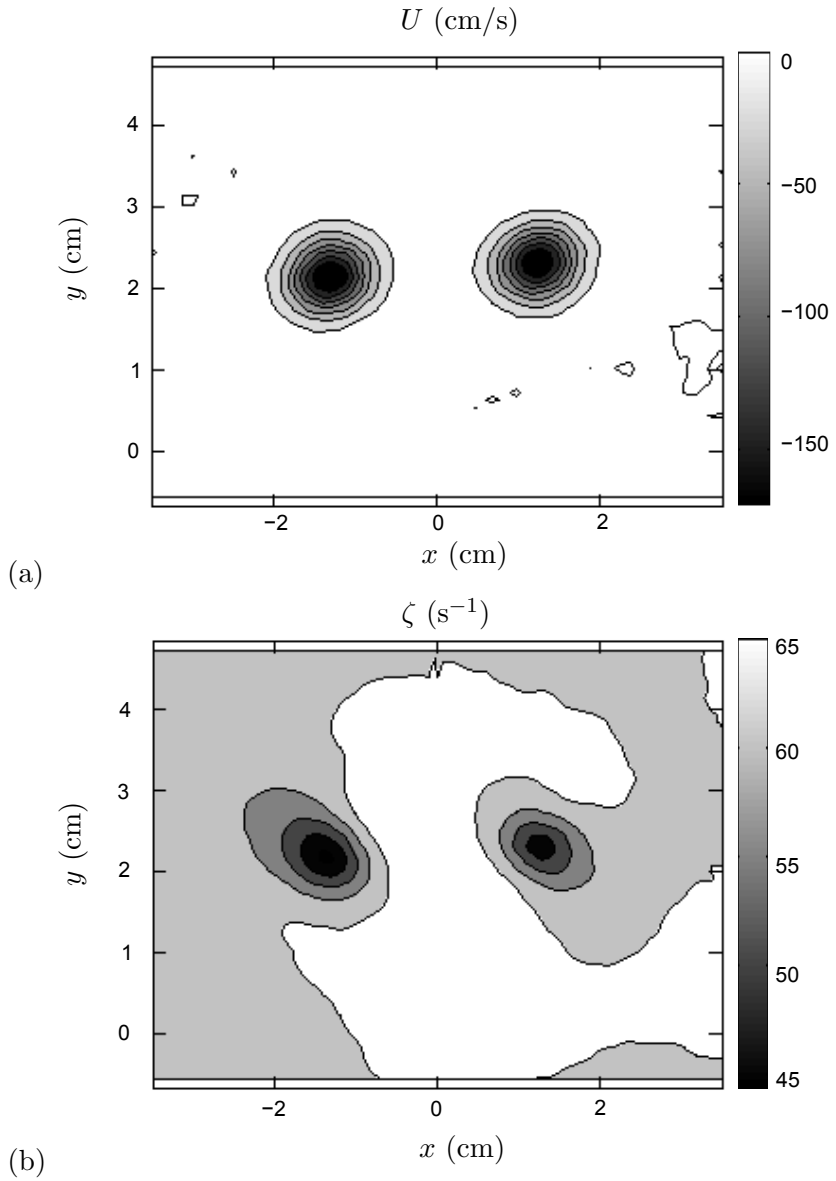

FIG. 4.17 – Reconstituted time-averaged vorticity (a) and axial velocity (b) fields at $z/c = 9.0$. . The top vortex is now on the left.

		top vortex	bottom vortex
Γ	cm^2/s	-169	-170
ρ_1	cm	0.45	0.44
ρ_2	cm	2.14	2.30
ϕ		0.62	0.59
a_W	cm	0.47	0.46
b	cm	2.69	
Γ/ν		18000	18100
ρ_1/b		0.17	0.16
a_w/ρ_1		1.04	1.05
W_0		0.33	0.29

TAB. 4.3 – Parameters of the base flow extracted from Stereo-PIV measurements. The azimuthally averaged azimuthal velocity profile was fitted with a VM2 model defined by 4.22. Indices 1 and 2 refer to the upper and lower vortex, respectively

.

region containing all of the circulation. For many types of wing tip vortices, ρ_2 is significantly larger than ρ_1. The match is excellent, as shown in figure 4.18(a). The parameters obtained for each vortex are listed in table 4.4.1. The two vortices are very similar to each other. Similarly to the counter-rotating case, U_∞ is defined as the value of the axial velocity profile at $r/\rho_1 = 3$. The non-dimensional parameter W_0 is in this case equal to $W_0 = (U_0 - U_\infty)2\pi\rho_1/\Gamma$. W was very well fitted with by a Gaussian function (see figure 4.18). W_{01} is observed to be 12% greater than W_{02}. This difference is mainly due to a higher axial velocity defect in the centre of the top vortex compared to the bottom vortex, since the top wing is longer than the bottom wing.

In order to characterise the evolution of the vortex positions with downstream distance z, a laser sheet oriented in a direction normal to the free–stream was placed at $z/c = 1.7, 4.8, 7, 8.8$ and 9.8. Dye was injected at both wing tips. For each streamwise location, 6000 frames showing vortices were acquired. For every frame, each vortex was localised by computing the centre of mass of the light intensity. Averaging the coordinates obtained for each z/c gives a reliable estimation of the vortex positions in the (x, y) plane. This is illustrated in figure 4.19. It is clear that the vortex pair moves upward as z/c increases. A possible explanation for this behavior could lie in the large–scale background flow (rotation), induced by the wings inside the test section, which may entrain the vortex system away from its initial $x - y$ position.

The separation distance b evolved approximately linearly with z/c, varying from $b = 4.2$ cm at $z/c = 4.8$, to $b = 2.4$ cm at $z/c = 9.8$. A similar linear evolution was observed for the angle ϑ between the line joining the average position of the vortices and the x–axis, as shown in figure 4.20. This is a sign that the merging process has not yet begun (Meunier & Leweke, 2005).

4.4.2 Elliptic instability

Following the procedure used for the counter-rotating pair, fluorescein dye was injected into the top vortex, illuminated in volume in a direction parallel to the

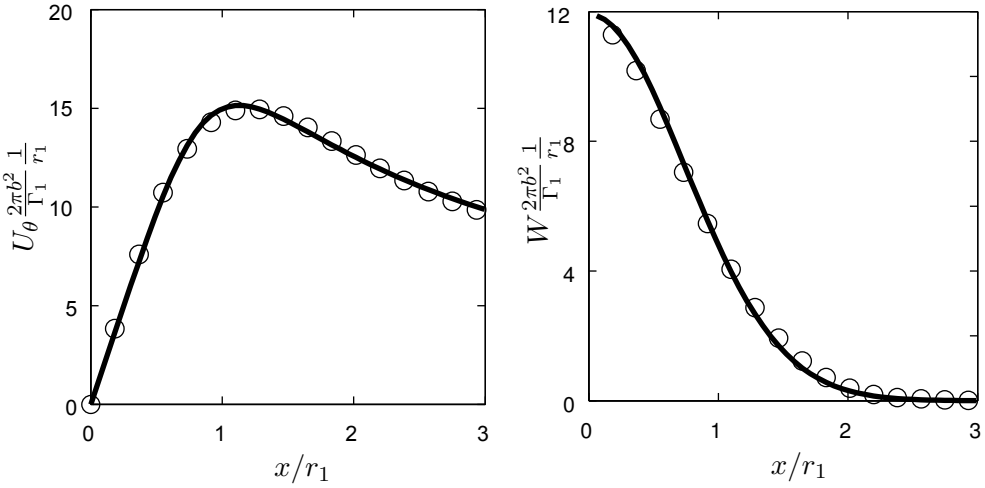

FIG. 4.18 – (a) : Azimuthally averaged azimuthal velocity profile for the top vortex $U_{\theta 1}$, as a function of the radius r. the experimental point are symbolised by dots. The solid line is the corresponding to the VM2 model. (b) : Same as (a) for the axial velocity defect W_1 fitted to a Gaussian function.

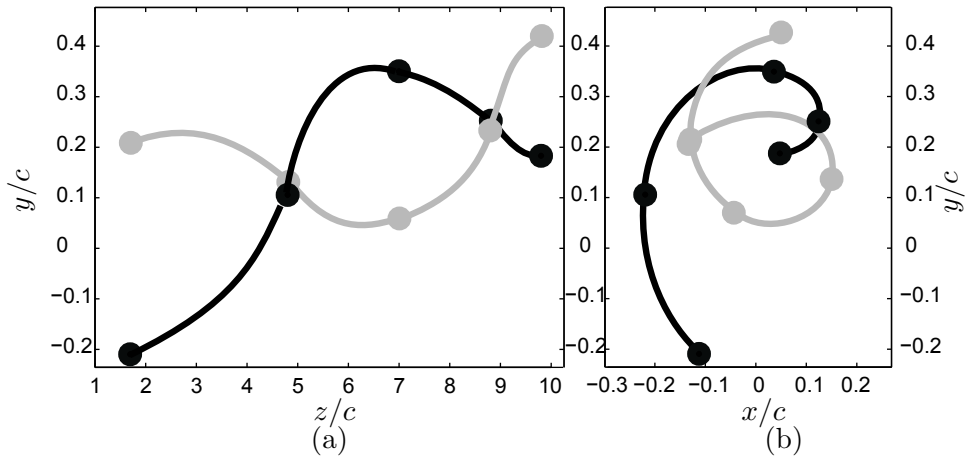

FIG. 4.19 – Position of the vortices in the (z, y) plane (a) and (x, y) plane (b). The scales of x and y axis are the same, contrary to the z axis.

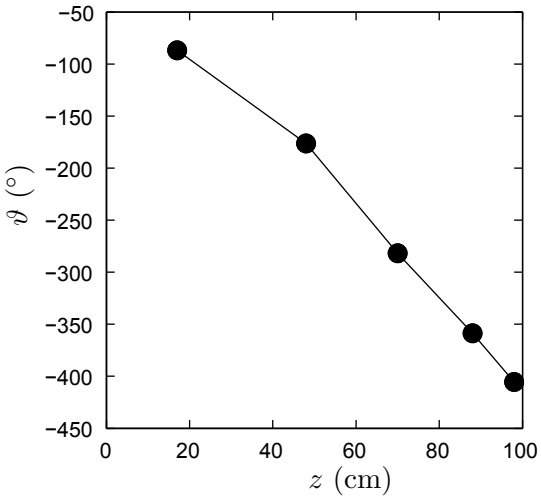

FIG. 4.20 – Angle ϑ formed by the wing tip axis and the line linking the average position of the vortices, as a function of the streamwise position z/c.

free–stream. At $z/c = 9.5$, 200 frames of the top vortex were captured. 15 of them, exhibited a short–wave perturbation with axial wavelength λ, an example is shown in figure 4.21. Averaging the values measured, we find

$$\lambda_1 = (1.09 \pm 0.12) \text{ cm}. \tag{4.23}$$

which corresponds to the non-dimensional axial wavenumber

$$k\rho_1 = 2\pi\rho_1/\lambda_1 = 2.59 \pm 0.36. \tag{4.24}$$

Since this value is about twice the vorticity radius ρ_1, it scales with the elliptic instability expectations. The perturbation is symmetric with respect to the axis of the vortex. This implies an even order of azimuthal symmetry. Since it was not visible upstream of $z/c \approx 9$, this perturbation is unstable and was triggered by the flow.

The theory of the elliptic instability presented in 4.3.3 for counter-rotating vortices (stationary strain field), also applies to co-rotating vortices. The rotation of the mutually induced strain field at the rate Ω changes the resonance condition (4.13) to

$$\begin{pmatrix} k_1 \\ m_1 \\ w_1 \end{pmatrix} - \begin{pmatrix} k_2 \\ m_2 \\ w_2 \end{pmatrix} = \begin{pmatrix} 0 \\ 2 \\ \Omega \end{pmatrix}. \tag{4.25}$$

Following these conditions, if the growing perturbation we observed was to be related to the elliptic instability, it would necessarily be the result of a resonance between Kelvin modes with $m_1 = 0$ and $|m_2| = 2$ or $|m_1| = 2$ and $|m_2| = 4$. Higher-order mode combinations would hardly be visible experimentally, local minima being partially hidden by maxima shifted by an angle of $\pi/4$, in the azimuthal direction. Figure 4.22 qualitatively compares the wavelength obtained in the experiment to the numerical results of Roy *et al.* (2008*b*) who studied the elliptic instability in a pair of Gaussian co-rotating vortices with axial flow. The

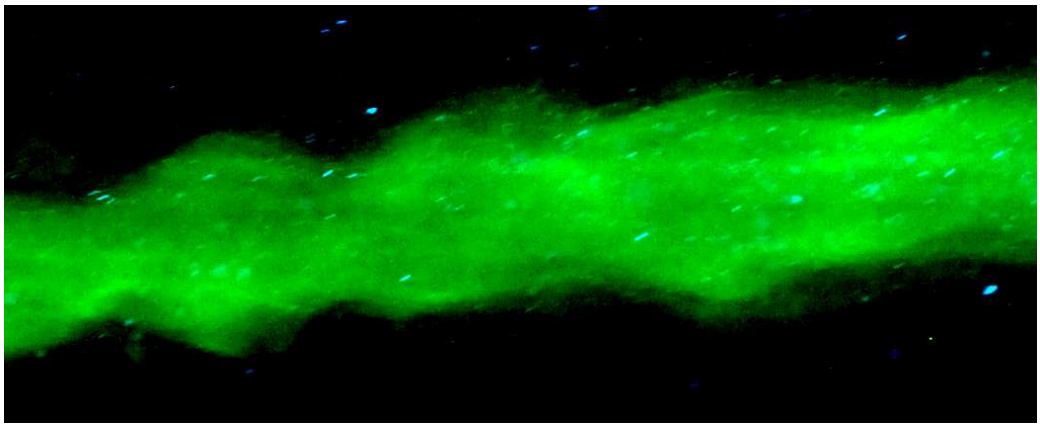

FIG. 4.21 – Visualisation of the instability propagating on the top vortex at $z/c = 9.5$. The field of view is approximately 2 cm $\times$ 4 cm.

experimental point is close to the mode $(0, -2, 2)$. For the value of W_0 measured experimentally, this mode is the most unstable one. The spatial structure of this mode is consistent with our observations. Given the fact that the base flow analysed is different in the two studies, the comparison remains qualitative, but it suggests that the $(0, -2, 2)$ mode is likely to be the cause of the instability observed experimentally.

4.5 Conclusions

In this paper, we have presented experimental results concerning the short-wavelength elliptic instability of a pair of co- and counter-rotating vortices with an axial velocity core. This instability was previously observed clearly only in vortex pairs without axial flow (Leweke & Williamson, 1998; Meunier & Leweke, 2005). It was demonstrated here to persist with the addition of the axial velocity. Dye visualisations and stereoscopic particle image velocimetry measurements allowed to extract qualitative an quantitative information on the spatial structure of the instability mode observed.

The axial wavelength of the short–wave instability was measured experimentally from dye visualisations of the vortex pairs. For the counter–rotating case, it was found to be in good agreement with the results of a linear stability analysis performed numerically on the experimental base flow. The discrepancies can be explained by the difficulty to determine the base flow responsible for the wavelength selection. The instability is observable at a given downstream position, where its amplitude is high enough to be noticed, but it was also on the vortex upstream of this position. The exact location where it was initiated, *i.e.*where it is selected, difficult to determine.

For the counter-rotating case, the experimental growth rate of the instability was determined from measurements of the amplitude at different downstream locations. The result matches very well with the numerical growth rate of the most unstable mode the elliptic instability.

To investigate in detail the spatial structure of the observed unstable mode, a

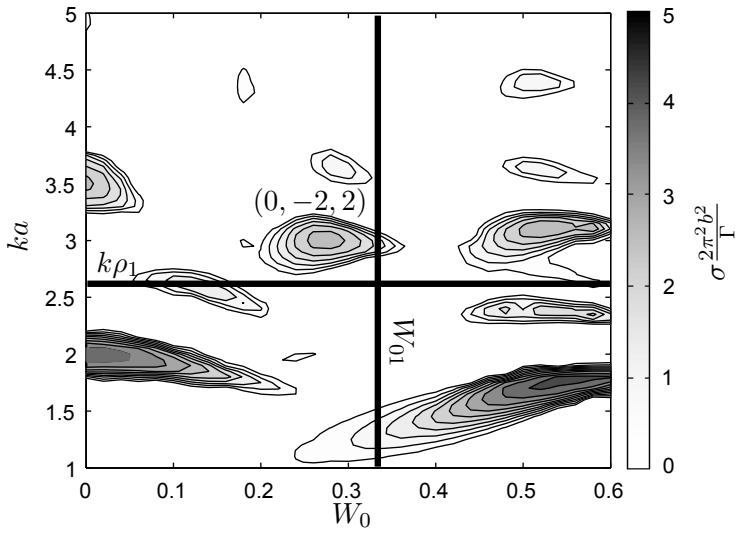

FIG. 4.22 – Contours of instability growth rate in the (W_0, ka) plane for $a/b = 0.14$ and $\Gamma/\nu = 88000$. This figure concerning a pair of co-rotating Gaussian vortices with axial core flow, was taken from Roy *et al.* (2008*b*).

Proper Orthogonal Decomposition based on dye visualisations of the top vortex was carried out. It revealed the superposition of two three-dimensional waves of similar magnitude, that can be related to Kelvin modes, both periodic in the axial direction. The first wave was axisymmetric, corresponding to an azimuthal wavenumber $m = 0$; the second one had a second order azimuthal symmetry ($m = 2$). The difference of 2 in the azimuthal wavenumber is typical of the elliptic instability in a vortex pair. Moreover, the azimuthal symmetry of the two waves corresponds exactly to the azimuthal symmetry of the two Kelvin modes resonating to form the most unstable mode obtained from numerical stability analysis.

In summary, we have, in this study, presented clear evidence of a short–wavelength three–dimensional instability, developing in counter- and co- rotating vortex pairs with axial flow jet flow in their cores. The spatial structure of the unstable perturbation is characterised by an azimuthal wavenumber $m = 2$, resulting in a double–helix structure of the perturbed vortex core. This is different from the short–wave instability modes previously observed on vortices without axial flow, which had an azimuthal variation with $m = \pm 1$. Qualitative and quantitative comparison of the experimental results with theoretical/numerical stability analysis have clearly identified this phenomenon as an elliptic instability of the vortex cores, caused by the mutually induced strain of the vortices.

The authors wish to thank S. Le Dizès for many helpful discussions during the course of this study. This work was supported by the European Commission under Contract no. AST4-CT-2005-012238 (FAR-Wake).

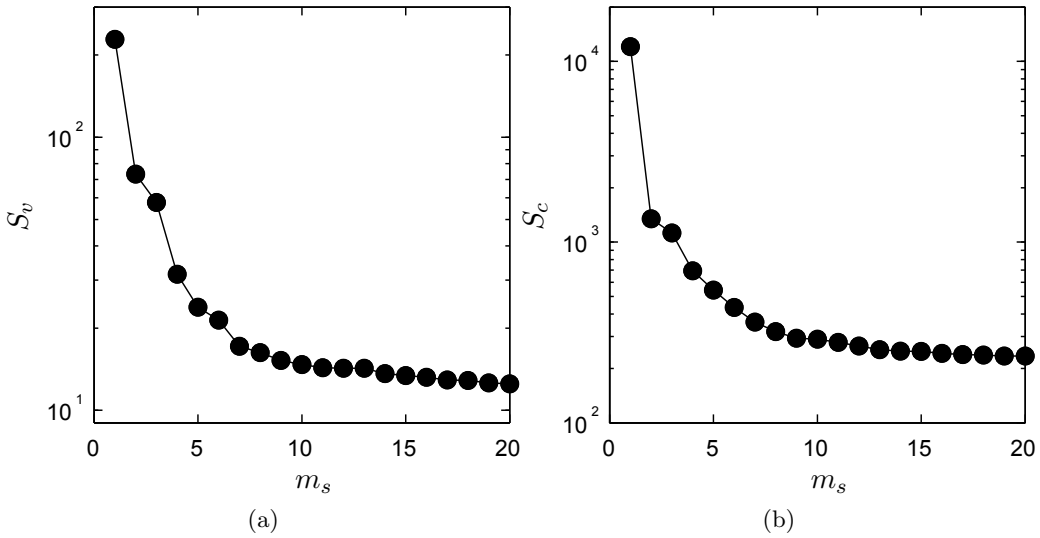

FIG. 4.23 – Comparison of the distributions of the first twenty singular values computed from the vorticity fields (S_v), and from the dye intensity in the frames (S_c).

cU_∞/ν	Γ/ν	ρ_2/ρ_1	γ	a_w/ρ_1	W_0
4660000	8700	5.52	0.48	1.31	0.27

TAB. 4.4 – Parameters of the base flow extracted from the Stereo-PIV measurements.

4.6 Relation between vorticity and dye POD modes

In this part, we demonstrate that the modes extracted by Proper Orthogonal Decomposition or POD (Berkooz *et al.*, 1993; Chatterjee, 2000; Liang *et al.*, 2002) on the vorticity field of a single vortex, show the same basic characteristics of the modes extracted by a POD on the light intensity of the frames where the vortex can be spotted by a dye patch.

For this work, presented in Roy & Leweke (2008), the same setup as described in §4.2 was used. Only the bottom wing, which can be seen in figure 4.2(b), was conserved in the water channel, to generate a single tip vortex in the free–stream. The angle of attack was fixed to 6° and the free–stream velocity to 46.6 cm/s. 400 Stereo-PIV measurements were performed to extract the three components of the velocity in a plan normal to the free–stream at $z/c = 11.2$. Following the recentring method presented in §4.3.1, the axisymmetric azimuthal velocity profile U_θ was fitted by the two–scale vortex model, VM2 defined by (4.22). The match is excellent. The axial velocity defect profile was fitted to a Gaussian function. The flow was characterised by the non-dimensional parameters listed in table 4.4.

The best way to compare accurately the results of the POD analysis on the vorticity and the light intensity is to run the POD on the same instantaneous flow for the two procedures. To make this possible, in addition to the Dantec particles used previously for the Stereo-PIV measurements, some fluorescein was injected at the wing tip and advected with flow. At $z/c = 11.2$, an argon ion continuous laser

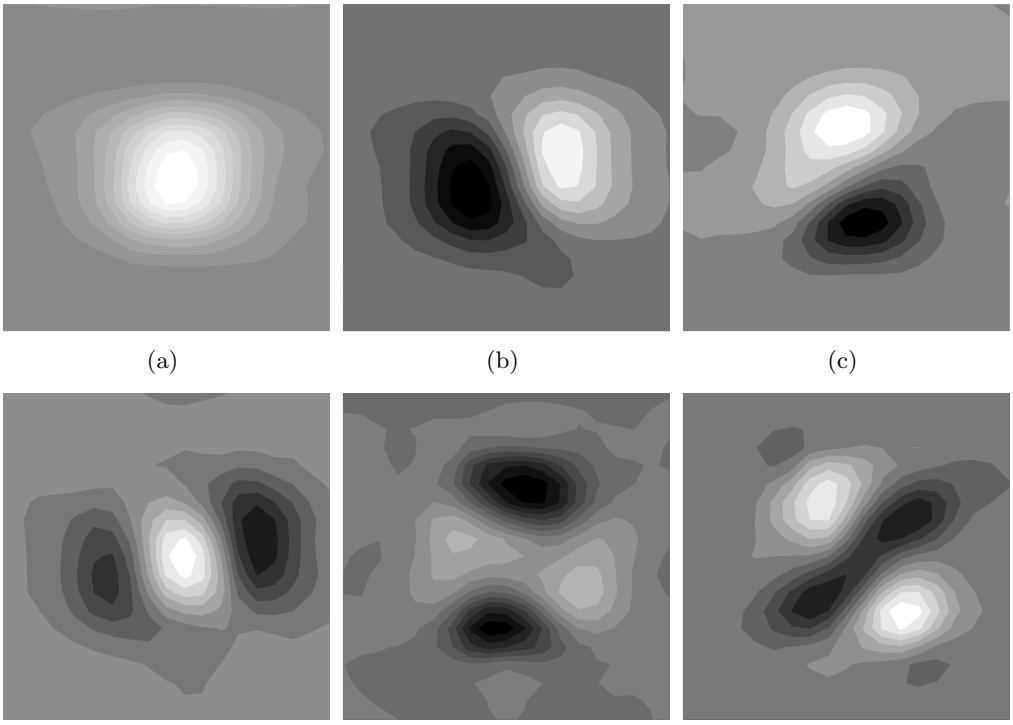

FIG. 4.24 – Modes computed by singular value decomposition of the vorticity field time series obtained by high-speed PIV for a single vortex (Re = 8700 and $W_0 = 0.27$). The six most energetic modes are shown.

illuminated the flow in a vertical plane normal to the free–stream. A cylindrical lens was used to focus the laser power on a small zone containing the vortex. A high–speed video camera was positionned at the end of the test section, watching the laser plane through the visualisation window presented in figure 4.1. For a duration of 8 seconds, 16000 images were recorded at an acquisition rate of 2000 Hz. The acquisition rate was fixed by the PIV requirement. On each frame, the particles seeding the flow and a dye patch similar to the one presented on figure 4.11 were visible. The light intensity level reflected by the particles was higher than the dye patch allowing the measure of the two component velocity field using planar PIV. For each frame, the vorticity was computed. The POD procedure based on singular value decomposition described in §4.3.3 was followed to extract the set of optimal modes for the vorticity and the light intensity. The singular values are presented in figure 4.23. The corresponding modes can be found in figures 4.24 and 4.25. The dimensions of the zone plotted in all the modes presented in figures 4.24 and 4.25, and the scale of the axes are the same. Also, the colour scale is symmetric with respect to 0, from black to white. Figures 4.23(a) and 4.23(b) look qualitatively alike. The singular values, which can be seen as the energy of the corresponding singular vector, rapidly decrease with the increasing order. The first mode corresponds to the mean field. In both cases, they show an axisymmetric zone (to the first order) around which the relative magnitude always has the same sign. The energy of this mode is much higher than the others. Modes 2 and 3 are,

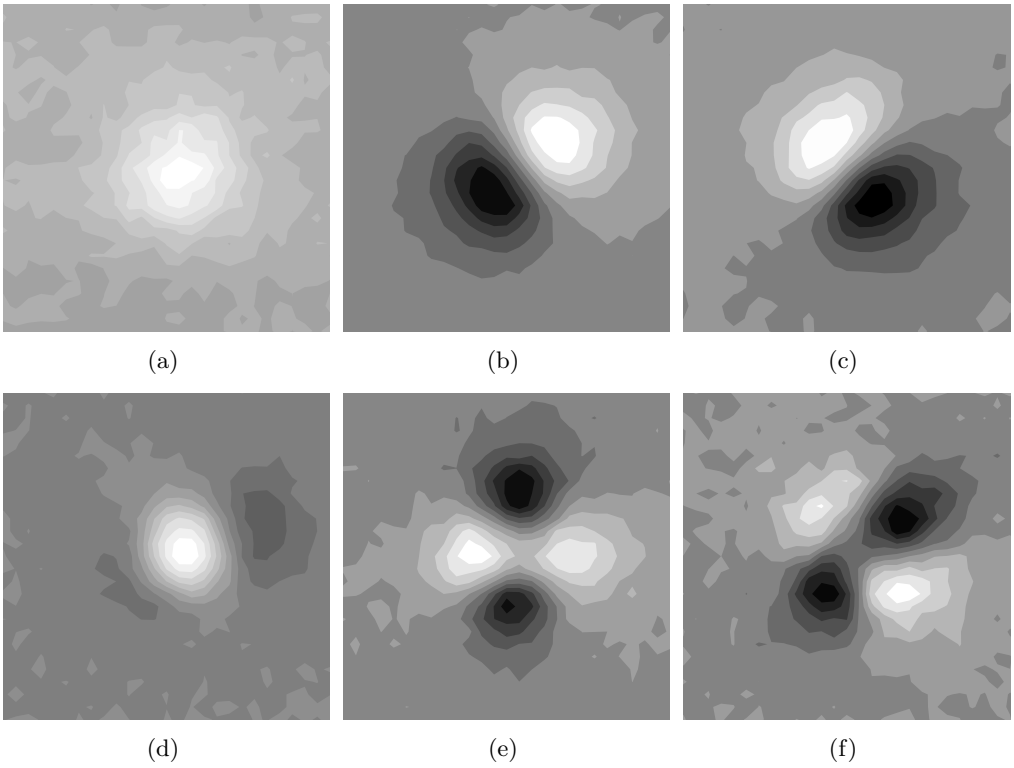

FIG. 4.25 – Same as figure 4.24, but obtained from dye intensity time series.

in both cases, associated with a global displacement of the vortex in the plane. They can be seen as a pure azimuthal wave of wavenumber $m = 1$. The only difference that can be noticed is a small tilt of the dye modes compared to the vorticity modes. This can be explained by the fact that the preferred direction of motion of the vortex is not very sharply defined as shown by Roy & Leweke (2008) for this flow. Nevertheless, the relative orientation of modes 2 and 3 remains constant at 90°. In figure 4.23(a) and 4.23(b), modes 2 and 3 form a doublet of similar energy, well separated from the rest of the modes. Both vorticity and dye POD identify the vortex displacement as the most energetic perturbation. Modes 4, 5 and 6 also look very similar. They all seem to result from the combination of $m = 2$ and $m = 0$ waves. Their absolute and relative directions are similar. The vorticity modes 4, 5 and 6 are slightly more isolated in the singular value hierarchy than the dye modes. They form a triplet that is easily visible in figure 4.23(a). Nevertheless, the rank of the modes is the same.

As a conclusion, the match between vorticity and light intensity modes obtained by POD is excellent. The same spatial structures were revealed in both cases. Furthemore, the hierarchy in the energy levels is conserved. This leads to the powerful conclusion that a POD analysis can be performed on dye visualisations to obtain information on the vorticity modes.

Chapitre 5

Vortex meandering

Ce chapitre est constitué d'un rapport rédigé dans le cadre du projet Européen FAR-Wake. Il présente une étude expérimentale concernant le phénomène du *vortex meandering*. On caractérise tout d'abord le meandering en utilisant une approche statistique. On donne ensuite des éléments de comparaison entre les résultats expérimentaux et la théorie de la croissance transitoire d'une onde de nombre d'onde azimutal $m = 1$.

5.1 Introduction

Work Package 1 of the projet FAR-Wake deals with the dynamics and instabilities of single vortices and multiple-vortex systems. Task 1.1, entitled "Waves on vortices" focusses on phenomena related to the dynamics of a single vortex. The present study is part of Subtask 1.1.1 on "Vortex meandering".

In this work, the dynamics of a single vortex generated by a generic wing in a water channel are investigated. The objective is to obtain detailed qualitative and quantitative information concerning vortex meandering, that will allow a comparison and confrontation with the different theoretical analyses performed in the same Subtask by partners UPS-IMFT and UMA. Such comparisons are expected to shed further light on the physical origin of this previously unexplained phenomenon.

5.2 Facilities and setup

5.2.1 The water channel

The facility used for the experiments is a recirculating water channel with a free surface. It has a test section of dimensions 37 cm (width) $\times$ 50 cm (height) $\times$ 150 cm (length). The free stream velocity U_∞ can be chosen in the range 5–100 cm/s by setting the pump rotation frequency F_p. The turbulence intensities associated with the streamwise and transverse velocity components are approximately 1.5% and 0.6%, respectively. The bottom and side walls of the test section are made out of glass. In addition, a glass window was inserted downstream of the test section on the wall normal to the stream, thus allowing visual access to the flow inside

the test section from five different directions. A scheme of the test section can be found in figure 5.1.

5.2.2 The wing

In order to generate a single vortex, a rectangular NACA0012 half-wing with a chord $c = 10$ cm was placed in the upstream part of the test section. It was manufactured out of polyvinyl chloride and has a span of 15 cm. The edge at the wing tip was rounded, with a varying diameter equal to the local thickness of the wing. The wing was mounted vertically on a profiled U-frame positioned along the side and bottom walls of the channel (see figure 5.2), so that the tip reaches the middle of the channel cross section. The tip of the trailing edge was chosen to be the origin O of the frame of reference defined in figures 5.1 and 5.2. Oz is the streamwise direction, Ox and Oy are the horizontal and vertical transverse directions. In this frame, we denote U_x, U_y and U_z the three components of the velocity. It was possible to adjust the angle of attack α manually by rotating the wing around an axis parallel to the (vertical) span direction. A small pipe network was machined inside the U-frame and the wing to allow for the injection into the flow of fluorescent dye (aqueous solution of fluorescein) close to the wing tip, in order to visualize the lift-generated trailing vortex.

5.2.3 Visualization setup

An argon ion laser (model Stabilite 2017 from Spectra Physics) was coupled to an optical fibre to illuminate the dye injected into the flow in a vertical plane, from the bottom to the top of the test section. Several injection holes in the wing were tested to find the one for which the dye remains in a region as close as possible to the center of the vortex. Taking advantage of the downstream channel window, a monochrome high speed video camera (Phantom V5 from Vision Research) was positioned for viewing along the Oz direction, in order to capture cross-sectional images of the vortex (see figure 5.1). All visualisations were made with the laser light sheet located at a distance $z/c = 11.2$ from the trailing edge of the wing.

5.2.4 Stereoscopic Particle Image Velocimetry (stereo-PIV) setup

A stereo-PIV technique was developed, in order to measure the three-dimensional velocity field of the wing tip vortices. A Nd-YAG pulsed laser was positioned underneath the test section at the desired distance from the wing, generating a 3 mm thick vertical light sheet. The flow was seeded with silver-coated particles (Dantec), whose size (100 μm diameter) was small compared to the characteristic scale of the vortex (diameter typically of the order of 1 cm). Images were taken with two high-resolution digital cameras (Roper Redlake, 4000×2672 pixels^2), each viewing the laser sheet along a direction forming a 30° angle with the axis of the channel (see figure 5.1). In order to reduce the distortions arising when looking through a liquid layer, the orthogonality between the cameras' lines of sight and the air–liquid interface was established by placing water-filled prisms between the object plane and the recording lenses. Special care was taken to enforce the so-called Scheimpflug condition, which requires the object plane, the lens plane, and the image plane to intersect on a single line. This ensures a good focus on the

object plane by diminishing the depth-of-field restrictions. An overview of stereo-PIV techniques, coupled with the use of prisms and Scheimpflug mounts, can be found in Prasad & Jensen (1995) and Zang & Prasad (1997).

The computing algorithm used for the extraction of fluid displacement from particle image pairs is based on a 2–D cross-correlation PIV code developed by Meunier & Leweke (2003), which has been successfully used in previous experimental studies on vortex flows (Meunier & Leweke, 2005; Boulanger *et al.*, 2007).

5.3 Results

In order to investigate the dependence of vortex meandering on Reynolds number and axial velocity, nine flow configurations were studied, characterized by different combinations of the pump frequency (F_p = 25 Hz, 35 Hz, 45 Hz) and the angle of attack of the generating wing ($\alpha = 6°, 9°, 12°$). For each case, stereo-PIV measurements were performed at a downstream location $z/c = 11.2$, in order to extract the parameters describing the vortex flow. Using dye visualisations made at the same position, it was then possible to follow the position of the vortex center over a period of time and extract statistical data characterizing vortex meandering. Proper Orthogonal Decomposition (POD) analysis was also performed, in order to obtain the most energetic modes of the vortex motion. Subsequent spectral analysis yielded information about the frequencies and the corresponding characteristic wavelengths of the vortex deformation.

5.3.1 Base flow characterization

Stereo-PIV measurements

Stereo-PIV measurements were performed to measure three-component velocity fields. For each configuration, 400 such fields were computed, from image pairs recorded at a frequency of 0.5 Hz. Each field was then fitted to the velocity field of a Gaussian vortex, in order to localism the coordinates of the vortex center, which are among the fitting parameters. (This Gaussian fit was here *only* used for the purpose of center finding ; the *actual* shape of the velocity profile is discussed in the following section below.) The mean position of all fields was computed, and each individual field was then translated, so that the vortex was always located at the mean position. The velocity components were then averaged over the 400 fields. The process of 'recentering' each vortex allows a correct estimation of the mean vortex velocity field, since the lateral motion due to meandering does not interfere with the averaging process. Not correcting for the vortex motion would have lead to an underestimation of the vorticity and axial velocity defect at the center, and to an overestimation of the vortex radius.

Figures 5.3, 5.4 and 5.5 present the two-dimensional distributions of streamwise vorticity and axial velocity obtained for the nine configurations tested. Although the vortex is mainly axisymmetric, the wake of the wing can be observed in the axial velocity fields. A major source of error arises from the presence of bubbles appearing at the center of the vortex for high values of the Reynolds number. The low pressure at the center attracts air bubbles from the outside region. These bubbles appear on the frames captured by the cameras, forming a bright horizontal

line (in the Ox direction) going through the center of the vortex. This leads to erroneous values of the vorticity in a localized region around $y = 0$, since U_y is underestimated there. This is the case for all α at the highest pump speed ($F_p = 45$ Hz) and also for $\alpha = 12°$ at $F_p = 35$ Hz.

Vortex velocity profiles

A standard way to characterize a vortex is to compute the azimuthally averaged profiles of swirl and axial velocity components as function of the distance r from the vortex center. Comparison with analytical vortex models, using least-square fits, then allows the determination of the characteristic vortex parameters. For the cases with erroneous U_y measurements mentioned above, the velocities were not averaged over the full azimuth, but only on a vertical line (Oy direction) going through the center of the vortex. There, U_x is the only velocity component taken into account for the azimuthal velocity, allowing a correct estimation of this profile.

Axial velocity defect The freestream velocity U_∞ was obtained by taking the maximum of the two-dimensional axial velocity profile. The axial velocity defect is defined as the difference between U_∞ and the local axial velocity in the channel. The azimuthally averaged radial profile of this quantity, $W(r)$, represents the axial velocity profile in the frame of reference moving with the vortex. It was found that for the vortices generated with the present set-up, this profile could be very well fitted by a Gaussian distribution given by

$$W(r) = W_{r=0} \cdot e^{-(r/a_w)^2}, \tag{5.1}$$

where $W_{r=0}$ is the maximum axial velocity defect, measured at the center of the vortex. Using this value, least-square fitting of the measured profiles to (5.1) allows determination of the radius a_w characterizing the size of the axial velocity distribution. Figures 5.6–5.8 show in their right columns the measured profiles of axial velocity, as well as the Gaussian fits, for all configurations tested. The overall agreement is very good. The principal cause of mismatch is linked to the fact that the axial velocity field is not exactly axisymmetric outside the vortex core. For large radii, the presence of the wing wake has a major effect on the axisymmetric average ; it it responsible, e.g., for the bump observed in figure 5.5(d).

Azimuthal velocity The total circulation Γ of the vortex was computed by integrating the cross-sectional velocity on a closed contour surrounding the entire field of view of the PIV measurement, as shown in figures 5.3–5.5, in order to take into account as much vorticity as possible. An approach similar to the analysis of the axial velocity, using a Gaussian fit, was first tried on the azimuthally averaged vorticity profile, but it turned out not to be satisfactory. Instead, following the approach of Fabre & Jacquin (2004*a*), the azimuthal velocity profile U_θ was fitted with their VM2 vortex model, according to :

$$U_\theta = \frac{\Gamma}{2\pi} \cdot \frac{a_2^{\phi-1}}{a_1^{\phi+1}} \cdot \frac{r}{\left[1 + (r/a_1)^4\right]^{(1+\phi)/4} \left[1 + (r/a_2)^4\right]^{(1-\phi)/4}}. \tag{5.2}$$

In this model, two radii a_1 and a_2 are defined. a_1 corresponds to the radius up to which $U_\theta(r)$ can be considered roughly linear in r, and a_2 is the minimum radius of a disk centered on the vortex inside which all the vorticity is contained. A third parameter ϕ quantifies the evolution of U_θ between a_1 and a_2. This model was proposed based on theoretical arguments concerning the structure of trailing vortices. Figures 5.6–5.8 (left column) show that the match with the measured velocity profiles is very good.

From the dimensional quantities $U_\infty, \Gamma, a_1, a_2, \phi, W_{r=0}$ and a_w, obtained directly or by fitting from the measured velocity fields, the following non-dimensional parameters were calculated :

- the chord-based Reynolds number cU_∞/ν,
- the vortex Reynolds number $\mathrm{Re} = |\Gamma|/\nu$,
- the axial flow parameter (inverse swirl parameter) $W_0 = 2\pi a_1 W_{r=0}/\Gamma$,
- the ratio a_2/a_1 of external and internal radii of the vorticity distribution,
- the ratio a_w/a_1 between the radial scales of the axial velocity and the vorticity profiles.

The values of all dimensional and non-dimensional parameter for all nine configurations tested are listed in table 1.

α	°	6	6	6	9	9	9	12	12	12
F_p	Hz	25	35	45	25	35	45	25	35	45
U_∞	cm/s	46.6	67.0	90.8	46.4	67.0	91.1	46.3	67.2	90.7
$\lvert\Gamma\rvert$	cm^2/s	87	134	181	126	188	268	152	225	314
a_1	cm	0.48	0.46	0.52	0.55	0.54	0.59	0.64	0.61	0.68
a_2	cm	2.66	2.86	2.90	2.90	3.39	4.90	2.85	3.93	7.99
$W_{r=0}$	cm/s	7.8	11.9	24.5	11.1	17.6	32.6	12.0	18.9	34.3
a_W	cm	0.63	0.53	0.43	0.57	0.45	0.38	0.55	0.46	0.37
cU_∞/ν	10^6	4.66	6.70	9.17	4.66	6.70	9.07	4.63	6.80	9.16
$\lvert\Gamma\rvert/\nu$	10^4	0.87	1.34	1.81	1.27	1.88	2.68	1.52	2.25	3.15
a_2/a_1		5.52	6.17	5.55	5.34	6.30	8.24	4.47	6.42	11.7
ϕ		0.48	0.45	0.48	0.61	0.63	0.69	0.73	0.77	0.86
a_w/a_1		1.31	1.15	0.82	1.04	0.83	0.65	0.87	0.74	0.54
W_0		0.27	0.26	0.53	0.31	0.32	0.52	0.32	0.36	0.55
β	°	89	92	88	72	69	67	77	62	59
a_M	cm	0.36	0.34	0.31	0.33	0.32	0.28	0.35	0.30	0.27
a_m	cm	0.20	0.19	0.18	0.18	0.20	0.18	0.25	0.22	0.18
a_m/a_M		0.56	0.56	0.58	0.55	0.63	0.64	0.71	0.73	0.67

Tab. 5.1 – Vortex parameters for all configurations tested.

The linear dependence of the total circulation Γ versus the angle of attack α is presented in figure 5.9. A slight circulation drop is observed for the highest angle ($\alpha = 12°$), and in particular for $F_p = 25$ Hz, for which U_∞ is the smallest. This marks the limit between the linear regime and the stall regime, which, as shown below, can also be seen in the measurements of the amplitude of vortex

meandering.

5.3.2 Statistical analysis of vortex position

In order to track the lateral vortex position in the flow, dye visualizations were performed as described in section 5.2.3. For each flow listed in table 1, 16000 frames were taken at a rate of 300 Hz over a period of 54 seconds. An example of a visualization frame is shown in figure 5.10. The high acquisition rate allows a study of phenomena occurring over a wide range of frequencies. In this study, we restrict our analysis to low frequencies, focusing only on the long-wavelength (low-frequency) meandering of the vortex. On a given frame, the coordinates (x_c, y_c) of the vortex center were obtained by computing the "center of mass" based on the brightness (light intensity) of the image pixels. This approximation is based on the reasonable assumption that the dye distribution is centered on the vortex (symmetric with respect to the center), which depends on the adequate positioning of the dye injection holes on the wing. Figure 5.10 shows that this condition is satisfied fairly well.

In order to characterize the distribution of the transverse position of the vortex center, the eigenvalues a_M^2 and a_m^2 of the covariance matrix of x_c and y_c were computed. If we impose $a_M > a_m$, the two corresponding eigenvectors $\mathbf{v_M}$ and $\mathbf{v_m}$ give the directions in which the statistical dispersion is maximal and minimal, the eigenvalues being the corresponding variances in both directions. a_M and a_m can be considered as dispersion radii in the $\mathbf{v_M}$ and $\mathbf{v_m}$ direction. An angle β can be defined between the horizontal direction Ox and the direction of the major axis $\mathbf{v_M}$ of the vortex position distribution. A convenient way to illustrate these quantities is to plot the ellipse of radii a_M and a_m aligned in the principal directions $\mathbf{v_M}$ and $\mathbf{v_m}$. This is done in figures 5.11 and 5.13 for all configurations. For comparison, figure 5.11 also shows the vortex positions obtained from each individual frame.

The values of a_M, a_m and β are listed in table 1. Whereas the mean amplitude of displacement (given by a_M and a_m) remains well below the inner vortex core radius at this downstream distance (11.2 chords), large excursions exist, too, which frequently exceed two core radii. For low values of Re, the principal direction of the distribution is close to the vertical axis Oy. It corresponds to the direction of alignment of the wing. No convincing explanation for this correlation can be put forward at this point. As Re and W_0 increase, β decreases, tilting the distribution towards a direction normal to the wing. This rotation of the distribution with increasing Re is consistent with the observations of Devenport, Rife, Liapis & Follin (1996), although they did not compute the variances in the same way.

Figure 5.12 shows the evolution of a_M and a_m with α. These radii lie in the ranges $0.4a_1 < a_M < 0.75a_1$ and $0.26a_1 < a_m < 0.42a_1$, i.e. the characteristic amplitude of meandering at this downstream location is roughly 50% of the viscous inner core radius. The general behavior of the radii is to decrease with α. An exception to this rule is observed for $\alpha = 12°$ and $F_p = 25$ Hz. In this case, where the angle of attack is high and the velocity is low, the stall regime is reached. Zaman *et al.* (1989) showed that low frequency oscillations can be observed in the flow over an airfoil near stalling conditions. This phenomenon may lead to an additional perturbation of the vortex, resulting in higher vortex meandering amplitudes.

In order to estimate the statistical convergence of our results, figure 5.14(a) shows the evolution of the second moment S of a_M with the number of frames used. For all configurations, S gradually decreases and approaches an asymptotically constant limit. The slope ε of these curves is plotted in figure 5.14(b). For the sample size of 16000 frames, we find $|\varepsilon| < 4 \cdot 10^{-4}$ cm/(1000 frames).

5.3.3 Analysis of the vortex perturbation

The previous section focussed on the overall position of the vortex. In this section, the precise nature of the vortex perturbation, with respect to an axisymmetric straight reference flow, is investigated. First, the spatial structure of the perturbations will be described by determining the most energetic modes. Then, focussing on the first most energetic mode, corresponding to a lateral displacement, characteristic frequencies and wavelengths will be extracted from the measurements and compared to theoretical predictions.

Mode calculation

A common way to extract a set of modes characterizing the perturbation of a given base flow is to perform a singular value decomposition (or Proper Orthogonal Decomposition – POD Berkooz *et al.*, 1993) using a series of flow fields. In the case of a vortex, it is appropriate to use the vorticity distribution for this type of analysis.

The procedure is illustrated for the configuration with $\alpha = 6°$ and $F_p = 25$ Hz ($\mathrm{Re} = 8700, W_0 = 0.27$). The video camera was positioned as shown in figure 5.1 to perform high-speed planar (2D) PIV measurements at $z/c = 11.2$. For a duration of 8 seconds, 16000 particle images were recorded at an acquisition rate of 2000 Hz. The POD was then performed on the whole series of vorticity fields computed from these images. Through the singular value decomposition of a matrix containing all the fields, the perturbations were developed into an ordered set of orthogonal vectors (modes). The projection of the entire data onto the first vector has the highest energy (or variance), and this variance decreases with increasing order of the vectors. For the example chosen here, the relative energy of the first 20 modes is presented in figure 5.15(a). The corresponding spatial structure of the first 6 modes can be found in figure 5.16. (In this figure and others alike, all frames were plotted with a color scale centered on zero (black) ; since the frames represent eigenvectors, the notion of amplitude is not present.) The energy decrease is clearly visible but gets smaller with increasing mode number. The first mode can easily be linked to the mean (time-averaged) field. It represents an axisymmetric vortex. Modes 2 and 3, presented in figures 5.16(b) and 5.16(c), are centered on the vortex. They have an azimuthal symmetry of order 1, and represents a global lateral displacement of the vortex. The principal directions of the two modes form a 90° angle. A linear combination of both modes is therefore sufficient to account for vortex displacements in all directions of the plane. It is possible to associate modes 2 and 3 with a so-called Kelvin wave of azimuthal wavenumber $m = 1$. (see Fabre *et al.*, 2006, and references therein for a description of Kelvin waves). The associated energy has similar values for the two modes. They form a high-energy doublet easily noticeable in figure 5.15(a). This means that a large part of the

perturbation energy is used to displace the vortex, resulting in vortex meandering.

Mode 4 (figure 5.16(d)) has a second-order azimuthal symmetry. It describes an elliptic compression perturbation centered on the vortex. In terms of Kelvin waves, it can be interpreted as a combination of $m = 0$ and $m = 2$ waves. Modes 5 and 6 also have a second-order azimuthal symmetry. Both of them are similar to a Kelvin wave with $m = 2$. Nevertheless, contrarily to a pure $m = 2$ Kelvin wave, the center of the vortex is perturbed as well, revealing the influence of an $m = 0$ Kelvin wave. There is a $\pi/4$ phase difference between the two. Similarly to modes 2 and 3, a linear combination of modes 5 and 6 results in a perturbation with the same structure, but rotated by an amplitude depending on the relative contributions of each initial mode. Any angle of rotation can be obtained. It is possible to recover pure $m = 0$ and $m = 2$ Kelvin waves by a linear combination of modes 4, 5 and 6. This is consistent with the fact that the order or magnitude of their associated energies is the same, compared to the rest of the modes. Note that an increase of the number of fields might lead to the decoupling of the Kelvin modes directly by the singular value decomposition.

Although it is possible, with this method, to find modes with even higher spatial complexity ($m = 3$, $m = 4$, etc.), such modes of lower energy are not considered further in this study, their impact being less important.

One important goal of this analysis is to extract a frequency characterizing vortex meandering, related to a characteristic wavelength of this phenomenon via the free stream velocity. The idea is to compute the projection of the complete flow field onto the most energetic displacement mode, in order to obtain a scalar temporal series. A spectral analysis can then be performed to reach the above objective. The frequency of meandering, related to a long-wavelength deformation convected through the measurement plane, is expected to lie in an interval around 1 Hz in our set-up (this was confirmed by results shown below). A relatively long time interval is required for a given measurement, in order to resolve the fluctuation spectrum correctly in this low frequency range. On the other hand, the determination of vorticity fields requires PIV measurements, involving acquisition of two frames closely spaced in time. Due to hardware constraints and the particular requirements for PIV measurements and the subsequent POD and spectral analysis for the present experiments, it was not possible to obtain accurate vorticity fields over a time interval long enough for the spectral analysis.

An alternative method was tested, in which POD decomposition was performed from dye visualizations, using the light intensity field of the frames instead of the vorticity field. Contrary to PIV measurements, dye visualization only requires a single frame at a time, allowing much longer acquisition periods. In order to demonstrate the validity of such an approach, a comparison was performed between the results obtained with the vorticity field and those obtained with the light intensity distribution.

During the acquisitions of the PIV images leading to the results for the vorticity field in figures 5.15(a) and 5.16, the flow also contained a small amount of dye (such as in figure 5.10), since some dye from a previous visualization experiment was leaking in through the open injection holes. In this way, the same frames could be used to computed the POD on the dye distribution, leading to a direct comparison with the vorticity modes. The energy distribution obtained from the dye is presented in figure 5.15(b), and the spatial structure of the modes can be

found in figure 5.17. These figures are to be compared with figures 5.15(a) and 5.16. In figures 5.16 and 5.17, the modes are presented in the same order of energy content, and the axis scales are equal. The agreement between the two sets of results is extremely good, concerning the mode structure and spatial orientation. The fact that the sign is inverted for some modes is irrelevant, since the mode amplitude is arbitrary in this representation.

From this good agreement between the results obtained with vorticity and dye, we can draw the conclusion that the dye is a suitable marker of the flow structure, and that it can be used for POD analysis in the present case.

Meandering frequency and wavelength

For all configurations listed in table 1, the images used for calculating the statistics of the vortex center position in section 5.3.2 were used again for the perturbation mode decomposition and spectral analysis. As mentioned above, they were recorded with an acquisition rate of 300 Hz over a period of 54 seconds, which is long enough to resolve the fluctuations at low frequency correctly.

The results of this analysis are illustrated here for the case $\alpha = 9°$ and $F_p = 35$ Hz, i.e., Re = 18800 and $W_0 = 0.32$. The six most energetic modes describing the perturbation of the vortex in this configuration are presented in figure 5.18, whereas figure 5.19 shows the associated eigenvalues. The overall picture is similar to the one described in section 5.3.3, and the same comments apply. One clearly observes the mean field, the two displacements modes, and the three modes coupling $m = 0$ and $m = 2$ Kelvin waves. Since the objective is here the characterization of the overall vortex motion, emphasis is put on the most energetic perturbation "vector", the displacement mode 2 (figure 5.18(b)). The time-dependent projection of the visualization images on mode 2 is presented in figure 5.20 for a time interval of 7 seconds. As expected, the projection is centered on zero. It is possible to visually identify a period of approximatrely 1 second in this signal, synonymous to a 1 Hz frequency. It means that the vortex oscillates (on average) around the mean position (defined by mode 1, figure 5.18(a)) in the direction given by the orientation of mode 2.

Figures 5.22(c) and 5.22(d) present the power spectral density P versus the frequency f_m for the time signal in figure 5.20; on both a linear and logarithmic scale. In this particular case, it is difficult to extract from these plots a dominant frequency with a precision better than the one obtained visually from figure 5.20. Nevertheless, it is possible to identify a frequency $f_c \approx 1$ Hz above which the power spectral density decreases abruptly, following a power-law decay of slope -3.5 between $f_m = 1$ Hz and $f_m = 10$ Hz.

This behavior is also observed for all the other configurations, as shown in figures 5.21–5.23. In some cases (e.g., figures 5.22(a) and 5.23(c)), a peak is clearly visible, the power spectral density decreasing rapidly below f_c. For all configurations, $f_c \approx 1$ Hz appears to be a good estimation of the dominant meandering frequency at the fixed downstream position $z/c = 11/2$ in the present set-up. However, conclusions on the evolution of f_c with Re or W_0 are difficult to draw, given the shape of the spectra obtained in this study.

The frequency f_m of vortex meandering measured at a fixed distance behind the wing can be related to the axial wavelength λ and wave number $k = 2\pi/\lambda$ of

the vortex deformation in the frame of reference moving with the vortex, using transformations involving the free stream velocity U_∞ : $\lambda = U_\infty/f_m$ and $k = 2\pi f_m/U_\infty$. Figure 5.24 shows the power spectral density as function of the non-dimensional wave number ka_1 for the three cases where a clear maximum can be identified in the spectrum. For all three, this maximum is located approximately at $ka_1 = 0.05$, corresponding to $\lambda \approx 120a_1$, i.e., the vortex displacement wavelength is more than two orders of magnitude larger than the inner vortex core radius, which represents indeed a very long-wavelength deformation. Similar values of k and λ are also observed for all other cases studied.

Comparison with theory – transient growth and optimal perturbation

Antkowiak & Brancher (2004) and Fontane, Brancher & Fabre (2008) have investigated the possibility of transient energy growth in a Lamb–Oseen (Gaussian) vortex without axial flow, and its excitation by random fluctuations (stochastic forcing). They found that transient growth indeed exists in this generic vortex flow, and that for long observation times (compared to the vortex turnover period) a long-wavelength translation mode dominates.

Despite the fact that in the present experiments the vorticity profile is not Gaussian, and that there exists an axial core velocity, an attempt is made to compare the results presented in the preceding sections with those of Brancher and co-workers. For this, the non-dimensional time τ corresponding to our observations needs to be determined. In the theoretical analysis, time t is non-dimensionalised by the angluar velocity Ω_o of the fluid at the vortex center, which is equal to half the vorticity there and given roughly by $\Gamma/(2\pi a_1^2)$. In the experiments, t is the time it takes the fluid to move from the trailing edge of the wing to the measurement plane : $t = z/U_\infty$. This leads to :

$$\tau = \Omega_o t = \frac{\Gamma}{2\pi a_1^2} \cdot \frac{z}{U_\infty} = \frac{1}{2\pi} \left(\frac{\Gamma}{cU_\infty} \right) \left(\frac{z}{c} \right) \left(\frac{a_1^2}{c} \right)^{-2}. \tag{5.3}$$

With the non-dimensional measurement location $z/c = 11.2$ and the values of the other parameters given in table 1, one finds that for all configurations tested the non-dimensional observation time is given by : $\tau = 150 \pm 10$.

For the Gaussian vortex without axial flow, Antkowiak & Brancher (2004) have calculated, for each non-dimensional wave number ka, where a is the vortex core radius, an optimal time τ_{opt}, for which the transient vortex perturbation at this ka is maximum. Figure 5.25 reproduces their diagram and extends it to include the present result (with $ka = ka_1 = 0.05$), obtained for a similar Reynolds number range. The agreement is very good, despite the differences in vortex structure, suggesting that these differences are probably not of high relevance in the context of vortex meandering. Figure 5.26, taken from Brancher *et al.* (2006) and showing the maximum gain of transient perturbations as function of wave number, also gives the structure of these perturbations. The low-wave number (large wavelength) branch close to the values measured in the experiments belongs indeed to a translation (or displacement mode) of the vortex, whose spatial structure at the optimal time is the same as the most energetic perturbation in the experimental observation, shown in figure 5.18(b).

This good agreement between the present experimental results and the theoretical work carried out by UPS-IMFT strongly suggests that the meandering phenomenon observed in the water channel is indeed the manifestation of an optimal growth of transient perturbations. The detailed measurements provided here would allow an even closer comparison with the transient growth predictions. A similar analysis to the one by Antkowiak & Brancher (2004) could be carried out, but using the actual measured velocity field, including axial flow, and producing a diagram with the growth factor as function of wave number at the non-dimensional time corresponding to the experimental measurement.

5.4 Summary and conclusion

The goal of this work was to provide detailed experimental data about vortex meandering. For this purpose, a single trailing vortex was generated in a water channel, using a half-wing. Nine configurations were tested, involving different free-stream velocities and angles of attack. The circulation-based Reynolds number varied in the range 8700–31500, and the axial velocity defect at the vortex center was between 27% and 55% of the maximum swirl velocity.

Detailed measurements of the three-dimensional vortex velocity profiles were carried out at 11.2 chord lengths behind the wing, involving stereo-PIV and recentering of individual PIV fields before averaging. The swirl velocity in the cross-sectional plane was found to correspond closely to the profile of the VM2 vortex model proposed by Fabre & Jacquin (2004*a*), whereas the axial velocity profile was to a good approximation Gaussian. The fitting parameters were given for all configurations.

The first part of the meandering analysis dealt with the statistics of the vortex center positions in the measurement plane. It was found that the amplitude of vortex displacement decreases with Reynolds number, in agreement with Devenport's Devenport *et al.* (1996) earlier findings. The meandering amplitude was found to be of the order of the core radius, and the principal directions of motion were identified.

In the second part, singular value decomposition (or Proper Orthogonal Decomposition - POD) analysis was carried out, using high-frequency vorticity data from PIV and dye visualisation images. After confirming that both of these inputs give similar results, long time series of dye visualizations were analyzed by POD. The most energetic perturbations were found to be displacement modes of the vortex. Spectral analysis of the projection of the time series on these displacement modes showed that they are characterized by low-frequency oscillations (at the fixed measurement position), corresponding to wavelengths in the frame of reference moving with the vortex that are two orders of magnitude larger than the vortex core radius.

Comparison was made with theoretical results concerning transient growth in a Gaussian vortex without axial flow, presented by Antkowiak & Brancher Antkowiak & Brancher (2004). Despite the differences in the vortex velocity profiles, good agreement was found, concerning mode structure and wavelength, between the present measurements and their optimal perturbation at the given observation time. This agreement strongly suggests that the meandering phenomenon observed

in the water channel can be explained by the transient growth of vortex perturbations, initiated by background noise in the flow or by turbulence in the wake of the wing. It is likely that this conclusion remains valid for other experimental facilities of similar type, such as wind tunnels.

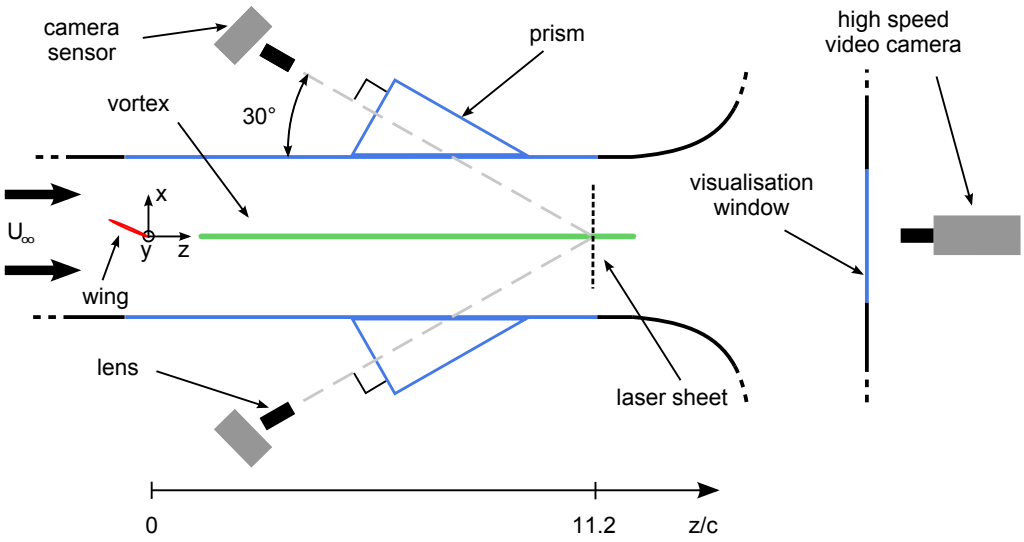

FIG. 5.1 – Schematic of the test section of the water channel, as seen from the top, showing the stereo-PIV and visualization set-ups. Glass windows are shown in blue. A laser (not represented) was placed underneath the channel, illuminating the flow in a vertical plane.

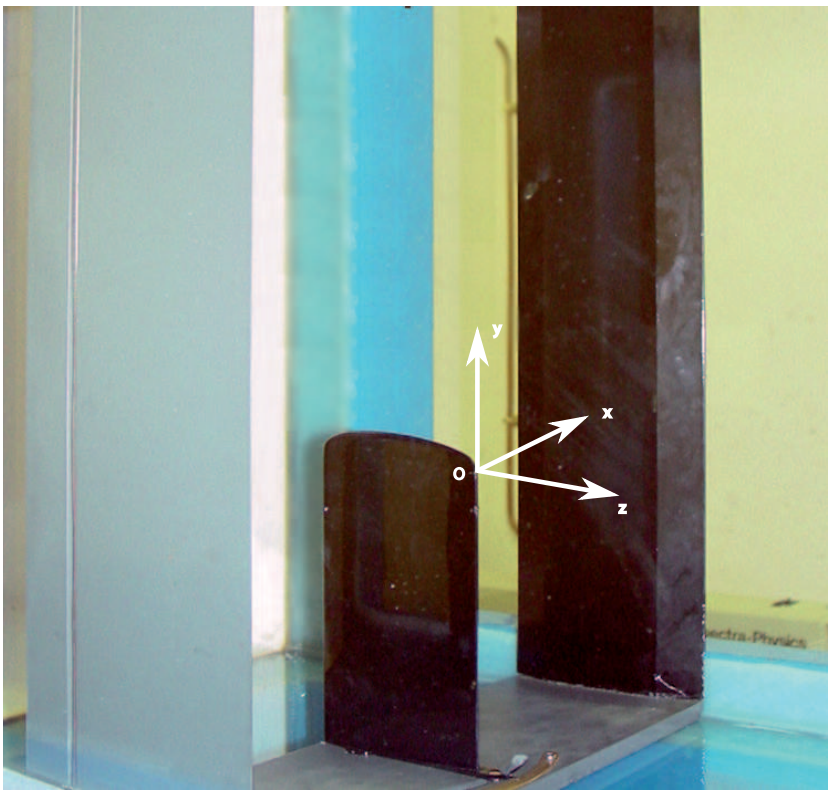

FIG. 5.2 – Wing set-up in the water channel.

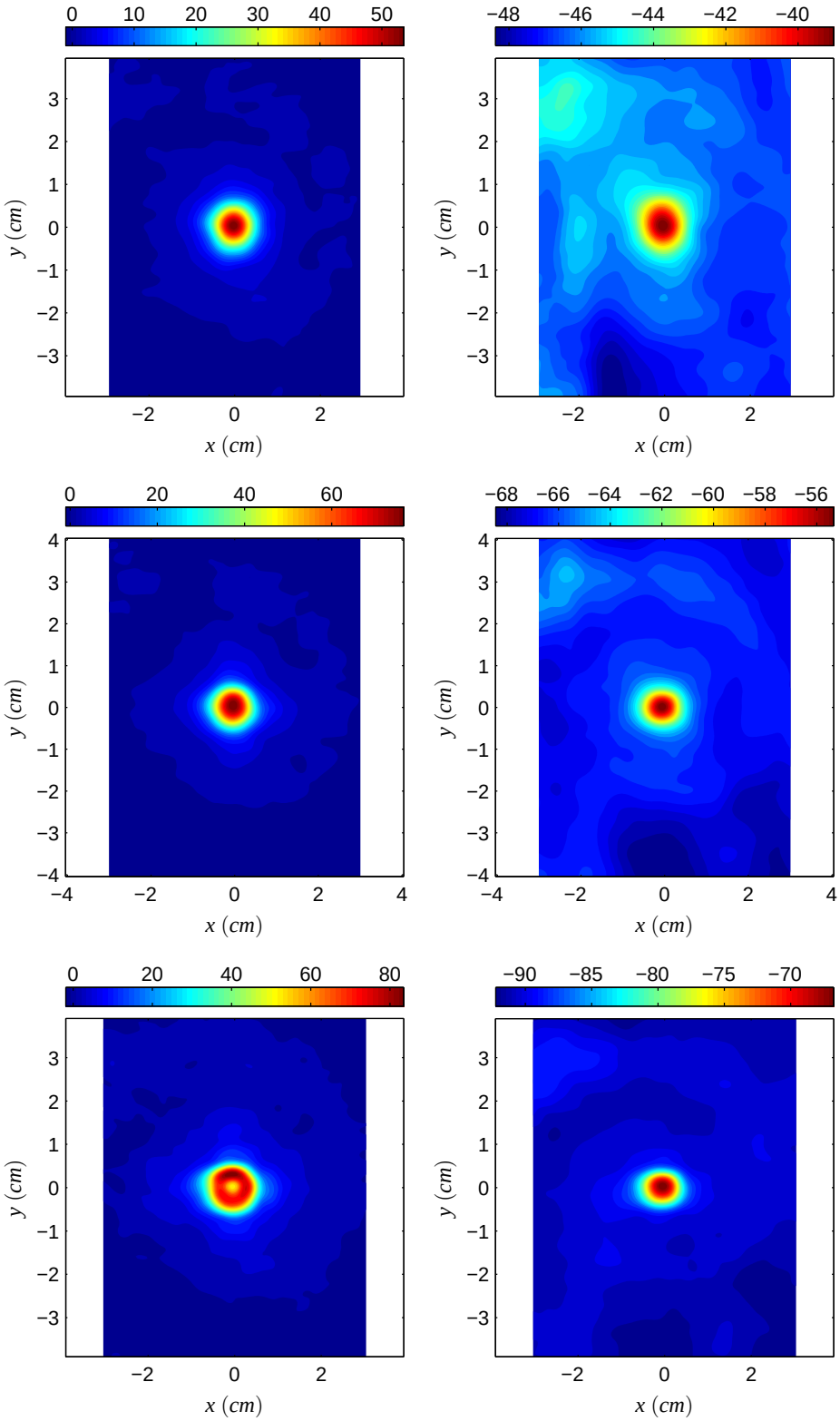

FIG. 5.3 – Two-dimensional distributions of vorticity [s^{-1}] (left column) and inverse axial velocity [cm/s] (right column), for $\alpha = 6°$ and $F_p = 25$ Hz, 35 Hz and 45 Hz (top to bottom).

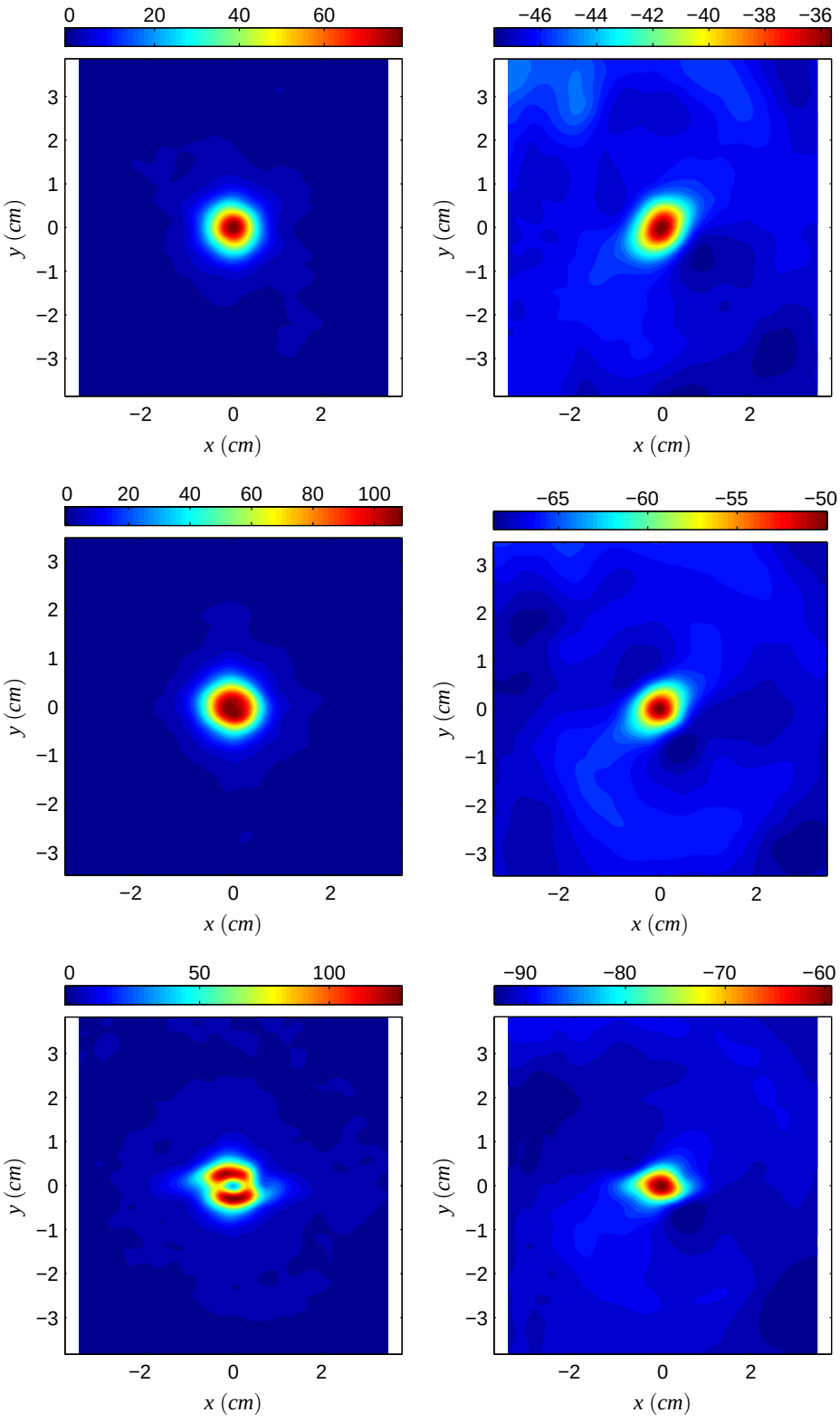

FIG. 5.4 – Same as figure 5.3, for $\alpha = 9°$.

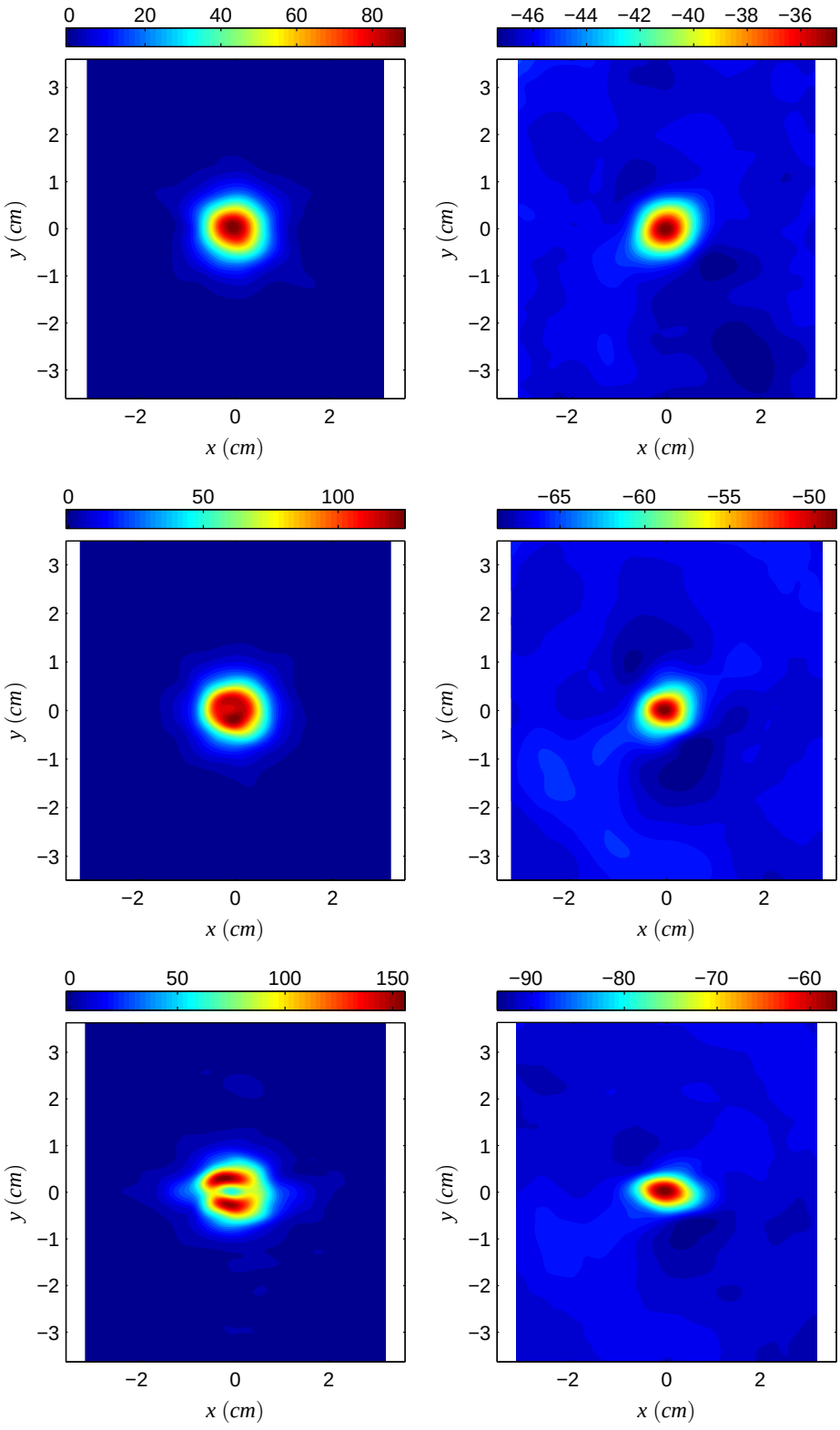

FIG. 5.5 – Same as figure 5.3, for $\alpha = 12°$.

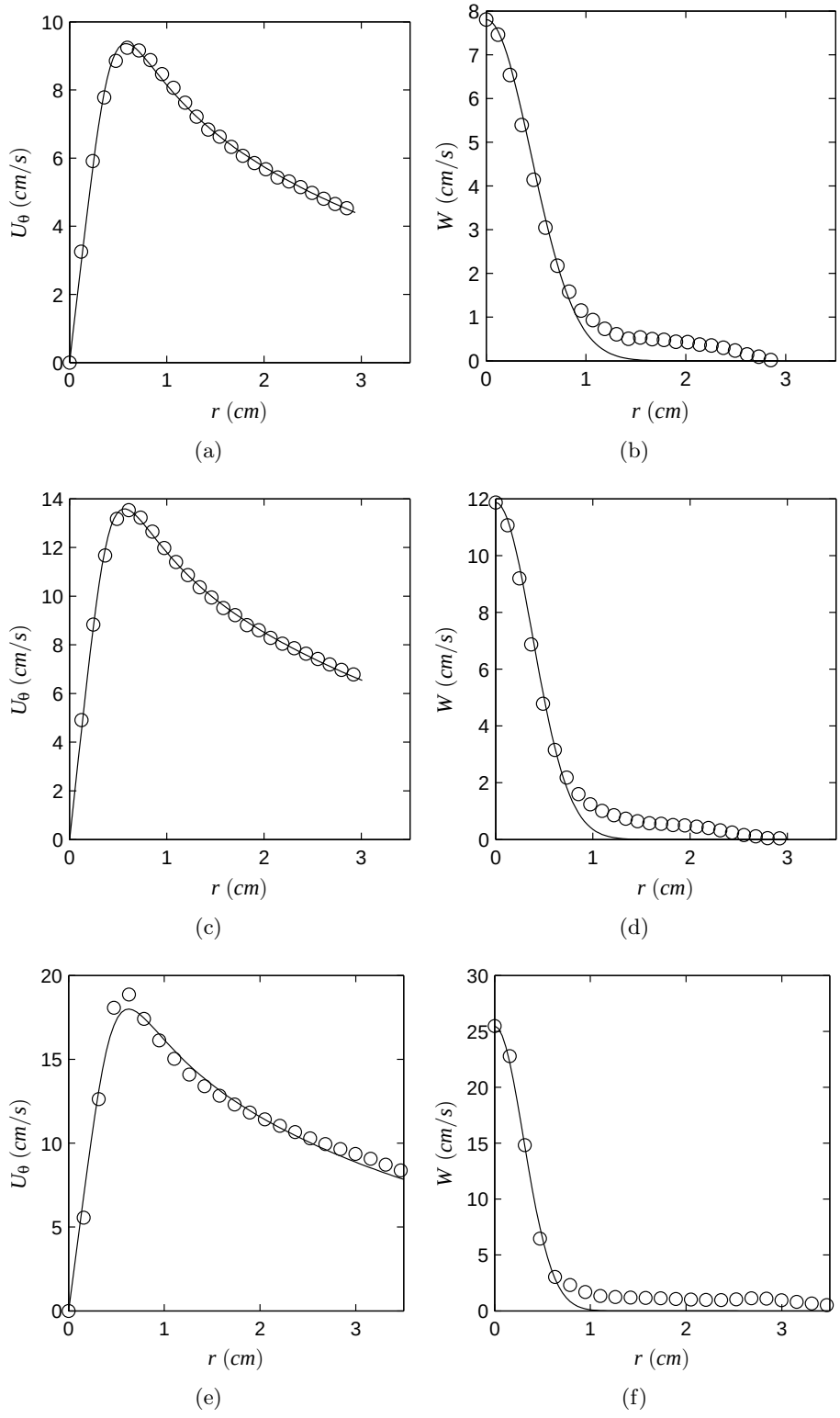

FIG. 5.6 – Azimuthally averaged radial profiles of swirl velocity (left column) and axial velocity (right column) for $\alpha = 6°$ and $F_p = 25$ Hz, 35 Hz and 45 Hz (from top to bottom). Circles represent experimental measurements, and lines are least-squares fits : VM2 model for U_θ, Gaussian for W.

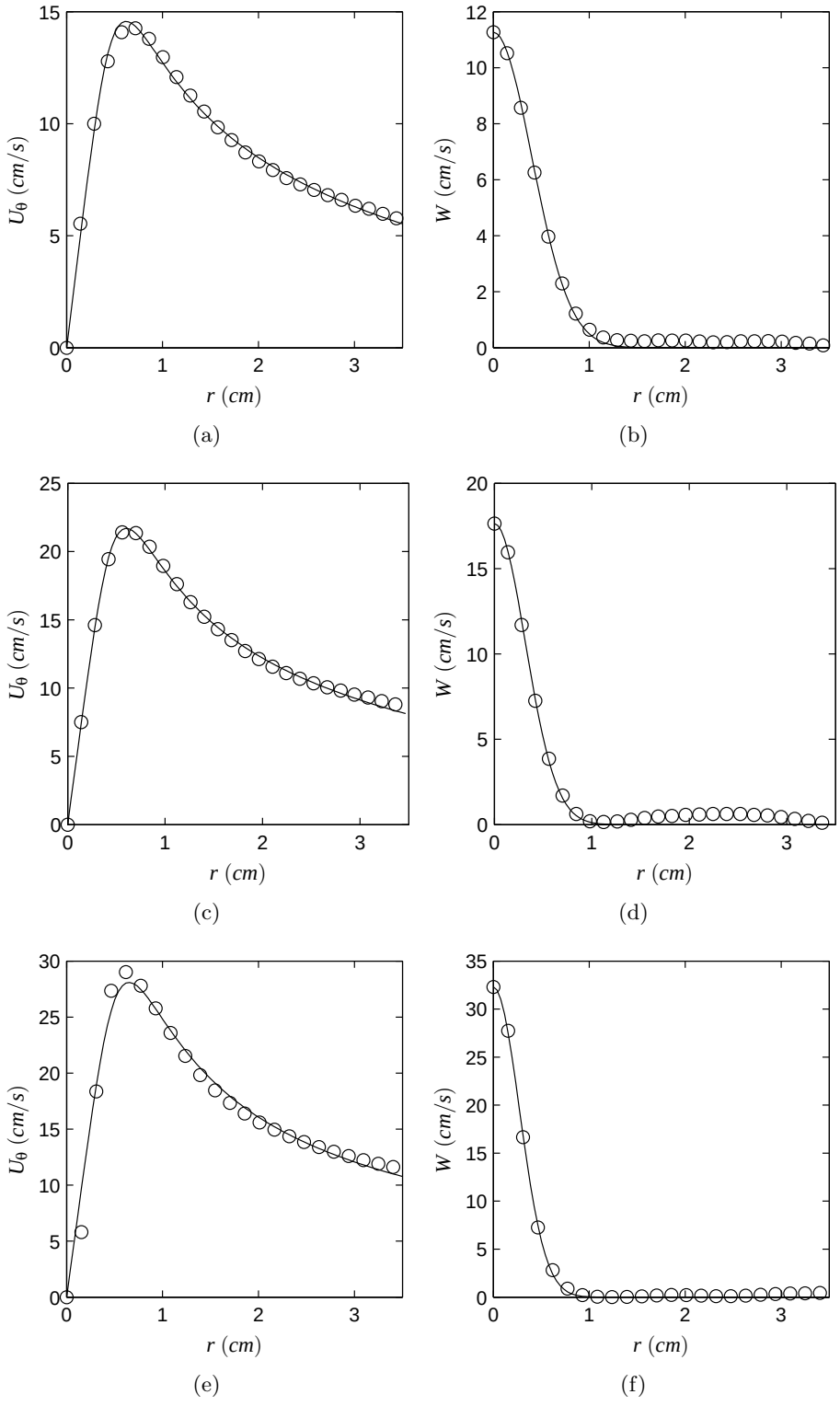

FIG. 5.7 – Same as figure 5.6, for $\alpha = 9°$.

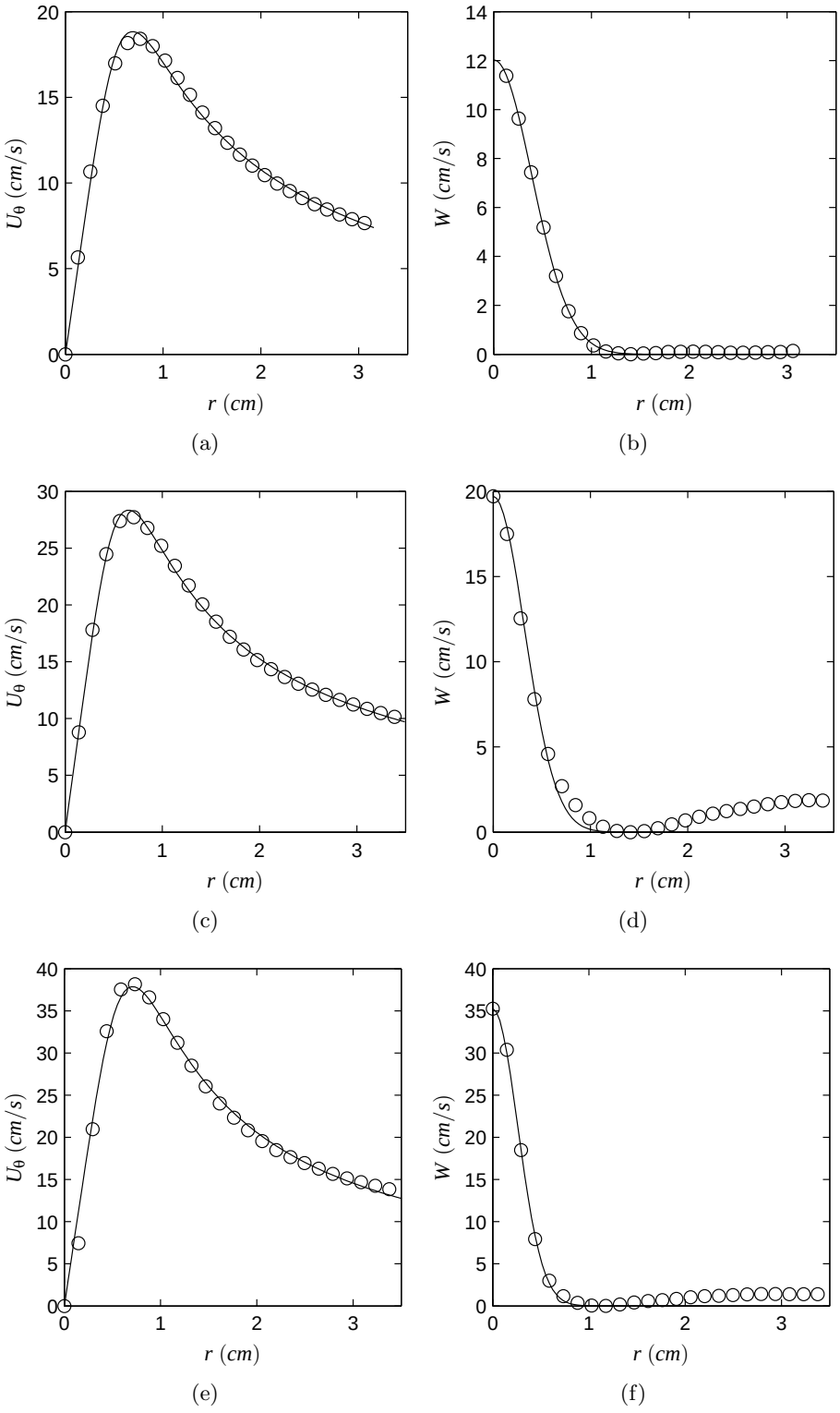

FIG. 5.8 – Same as figure 5.6, for $\alpha = 12°$.

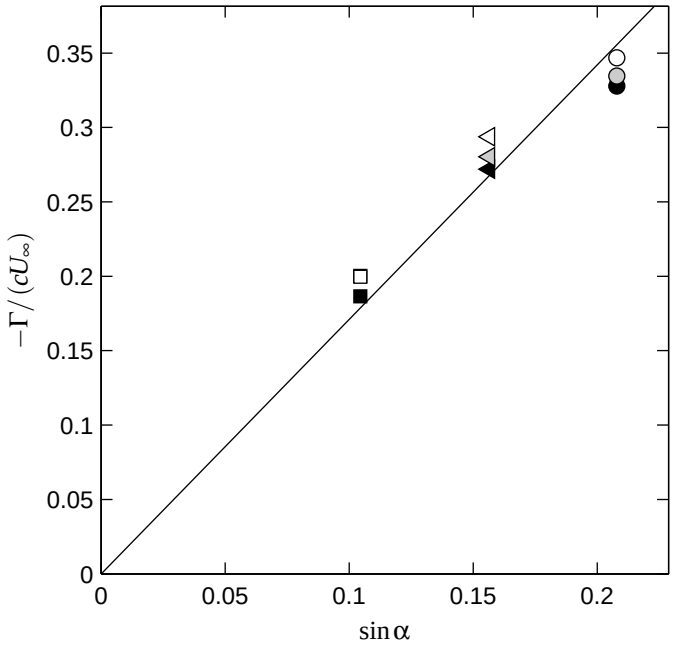

FIG. 5.9 – Variation of total vortex circulation with angle of attack. Circles, triangles and squares correspond to $\alpha = 6°$, 9° and 12°, respectively. Black, gray and white markers represent $F_p = 25$ Hz, 35 Hz and 45 Hz, respectively. The solid line represents a linear fit, yielding a slope $s = 1.71$.

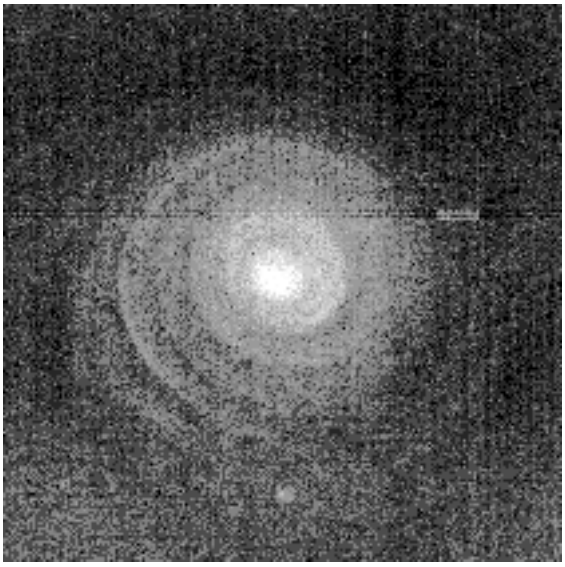

FIG. 5.10 – Example frame from the high-frequency dye visualization used for vortex position statistics and the singular value decomposition.

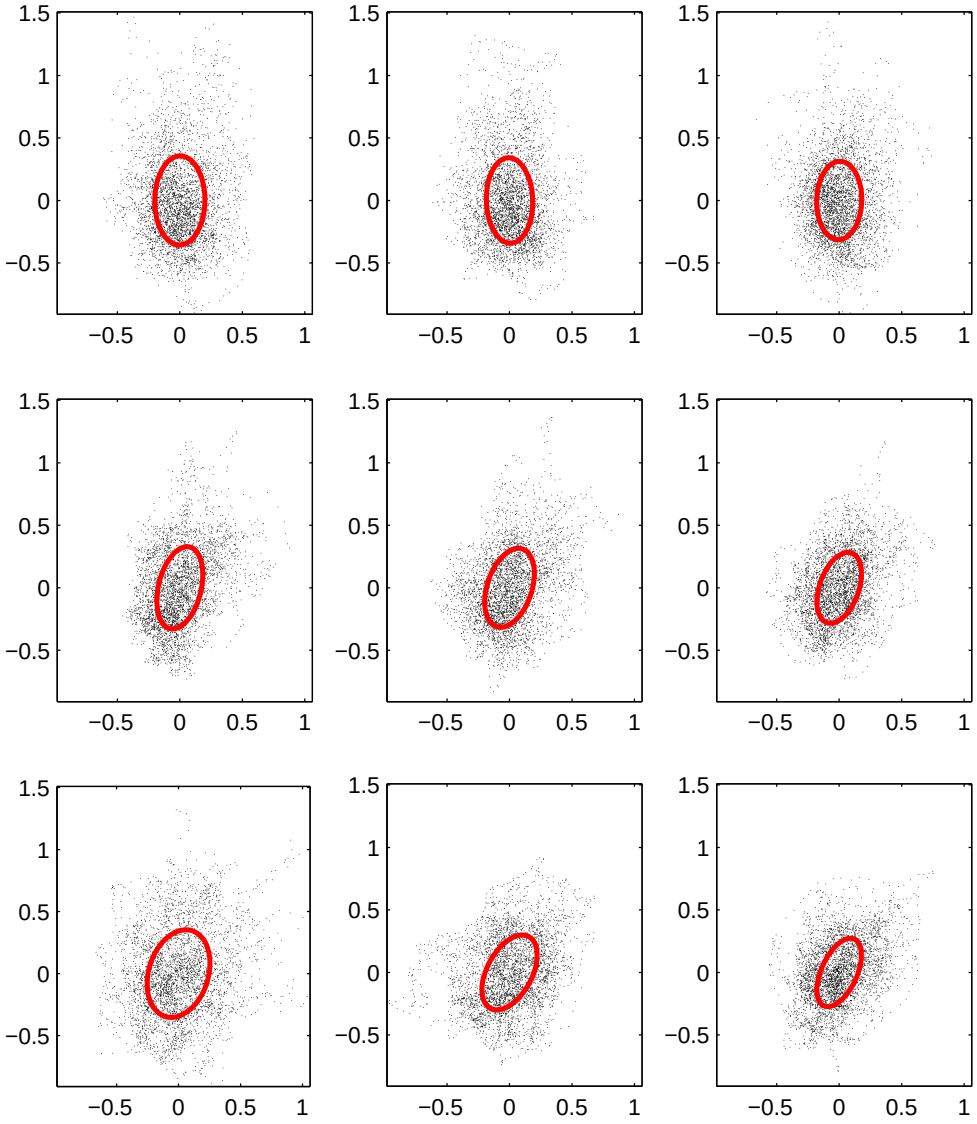

FIG. 5.11 – Distributions of the transverse vortex center positions at $z/c = 11.2$. Coordinates are centered on the mean position, and axes are in cm. $F_p = 25$ Hz, 35 Hz and 45 Hz (top to bottom) and $\alpha = 6°$, 9° and 12° (left to right). Axis units are cm. Each dot represents the position in one visualization frame. The red curve is an ellipse of radii a_M and a_m, whose major axis forms an angle β with the horizontal (see table 1).

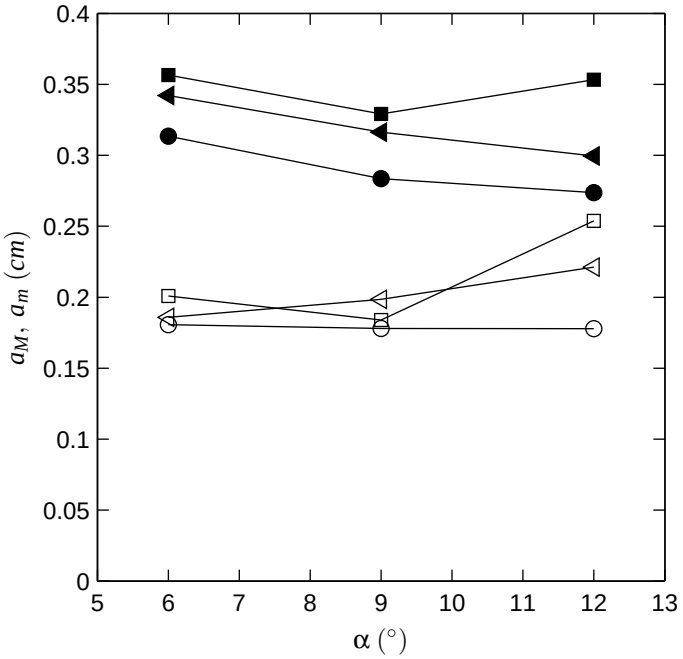

FIG. 5.12 – Radii a_M (solid symbols) and a_m (open symbols) as function of α. Squares, triangles and circles correspond to $F_p = 25$ Hz, 35 Hz and 45 Hz, respectively.

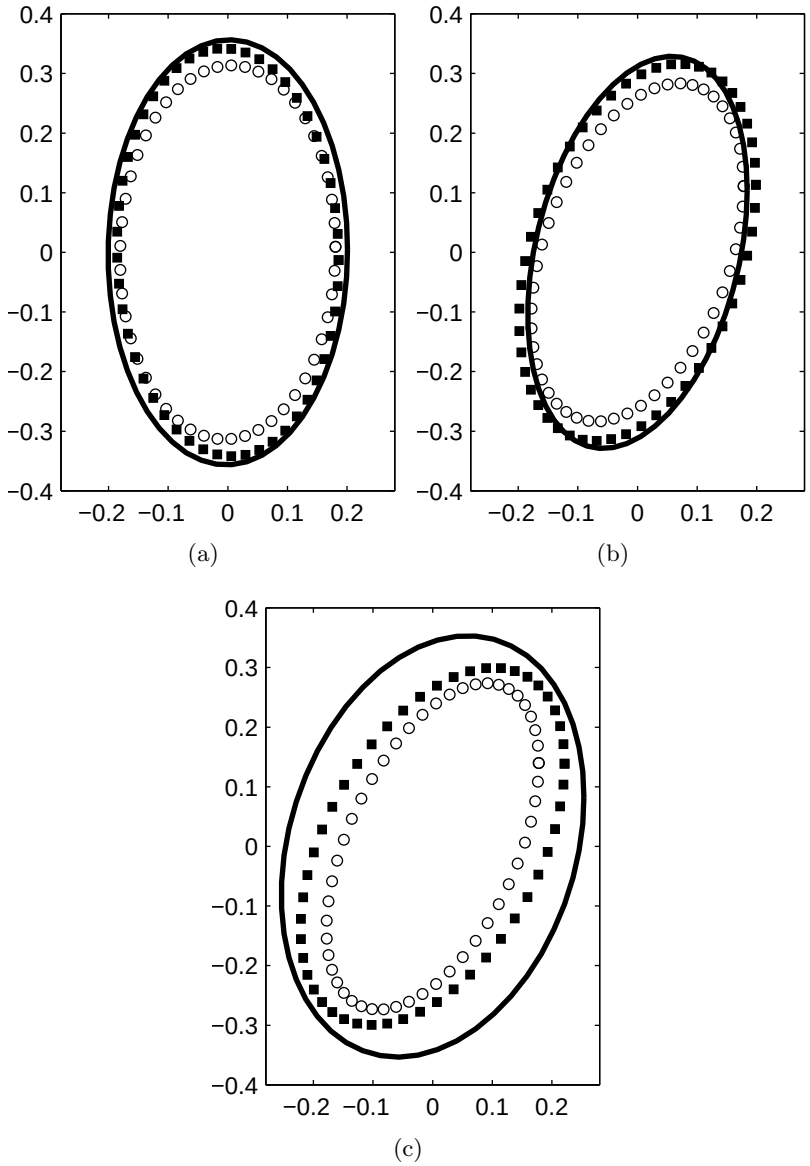

FIG. 5.13 – Ellipses associated with the distribution of the vortex centers for $\alpha = 6°$, $9°$ and $12°$. Solid lines, squares and circles correspond to $F_p = 25$ Hz, 35 Hz and 45 Hz, respectively. Axis units are cm.

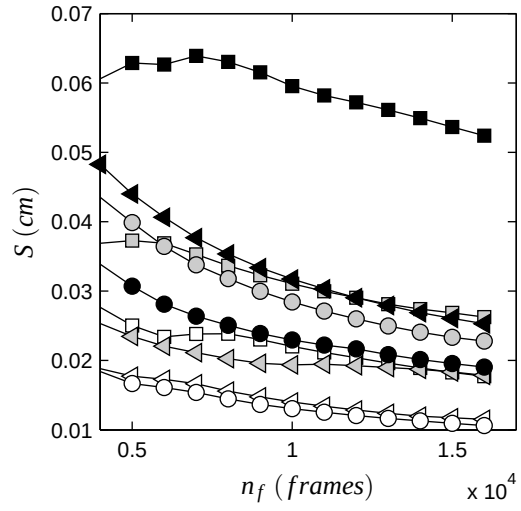

(a)

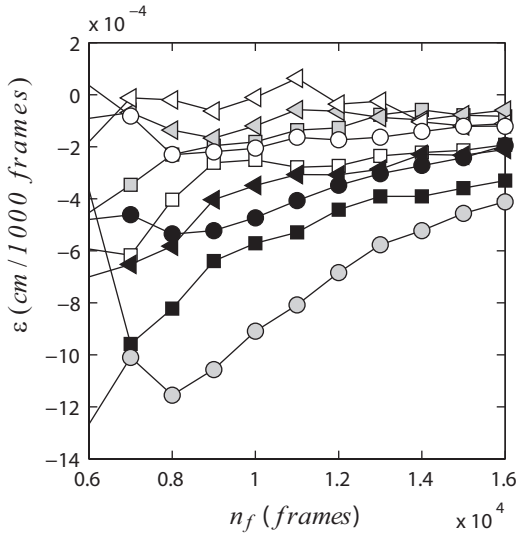

(b)

FIG. 5.14 – (a) The second moment S of the radius a_M as function of the number n_f of frames used for the calculations. (b) The slope ε of S as function of n_f. ε is computed every 1000 frames. White, gray and black markers represent $F_p = 25$ Hz, 35 Hz and 45 Hz, respectively. Squares, triangles and circles correspond to $\alpha = 6°$, 9° and 12°.

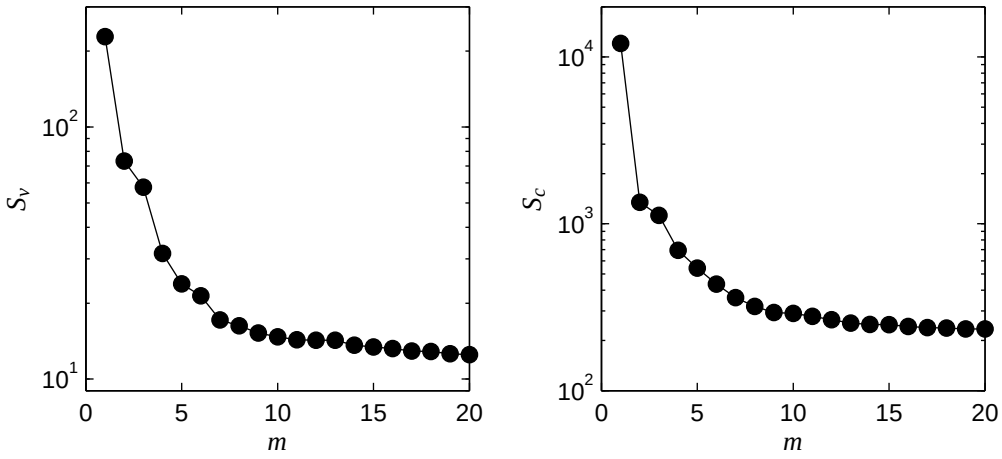

(a) (b)

FIG. 5.15 – Comparison of the distributions of the first twenty singular values computed from the vorticity fields (S_v), and from the dye intensity in the frames (S_c). $\alpha = 6^\circ$ and $F_p = 25$ Hz.

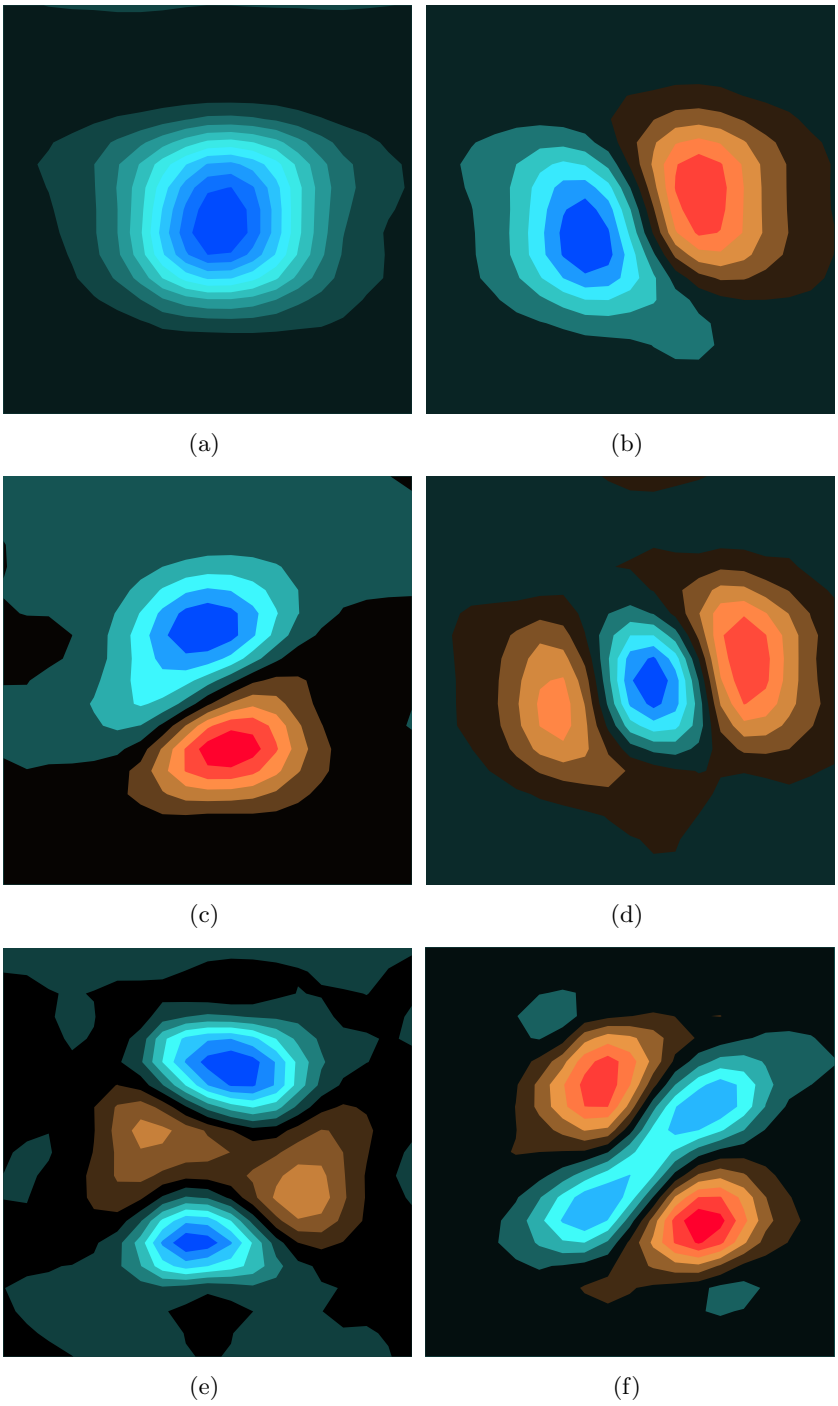

(a) (b) (c) (d) (e) (f)

FIG. 5.16 – Modes computed by singular value decomposition of the vorticity field time series obtained by high-speed PIV for $\alpha = 6°$ and $F_p = 25$ Hz (Re = 8700 and $W_0 = 0.27$). The six most energetic modes are shown.

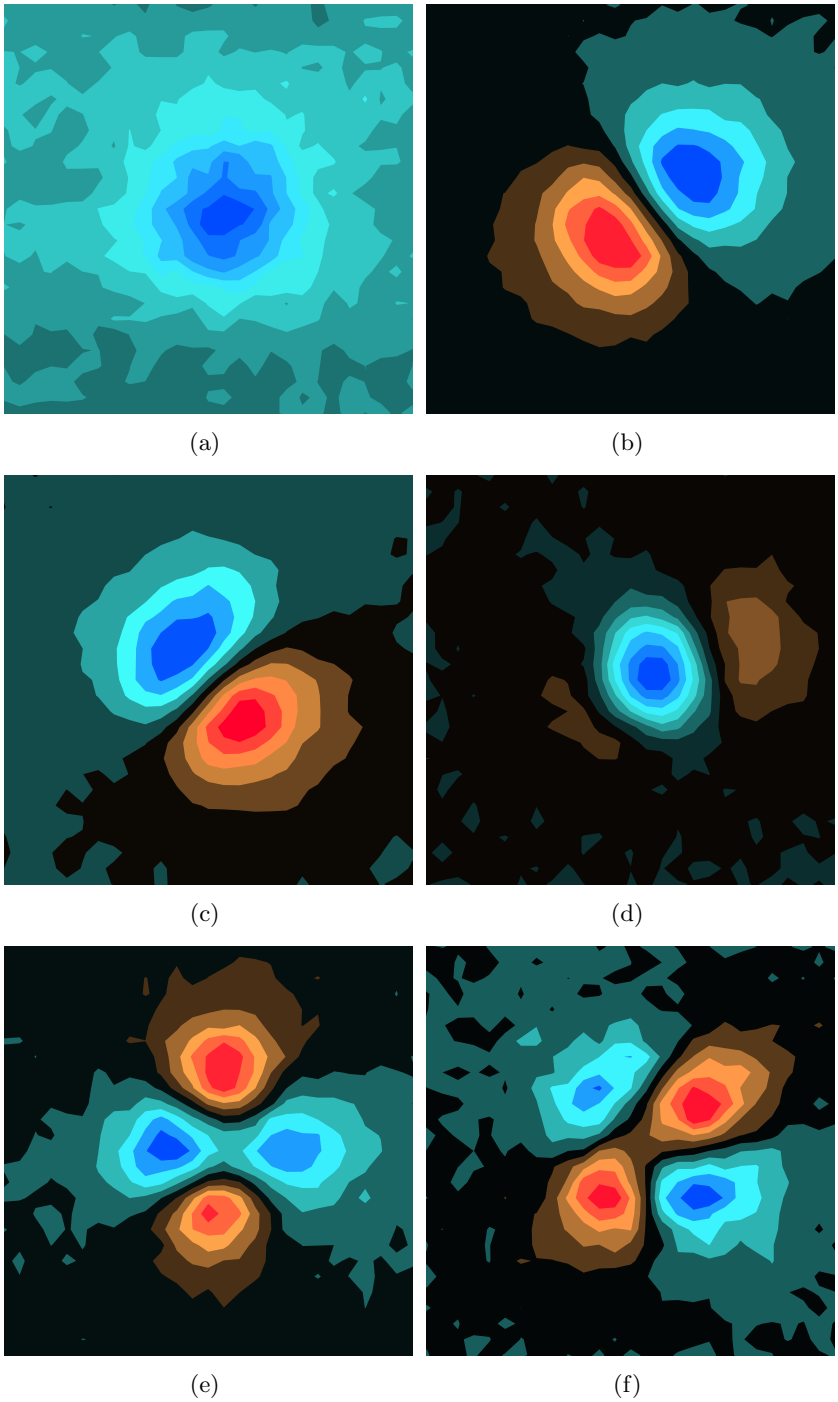

(a) (b) (c) (d) (e) (f)

FIG. 5.17 – Same as figure 5.16, but obtained from dye intensity time series.

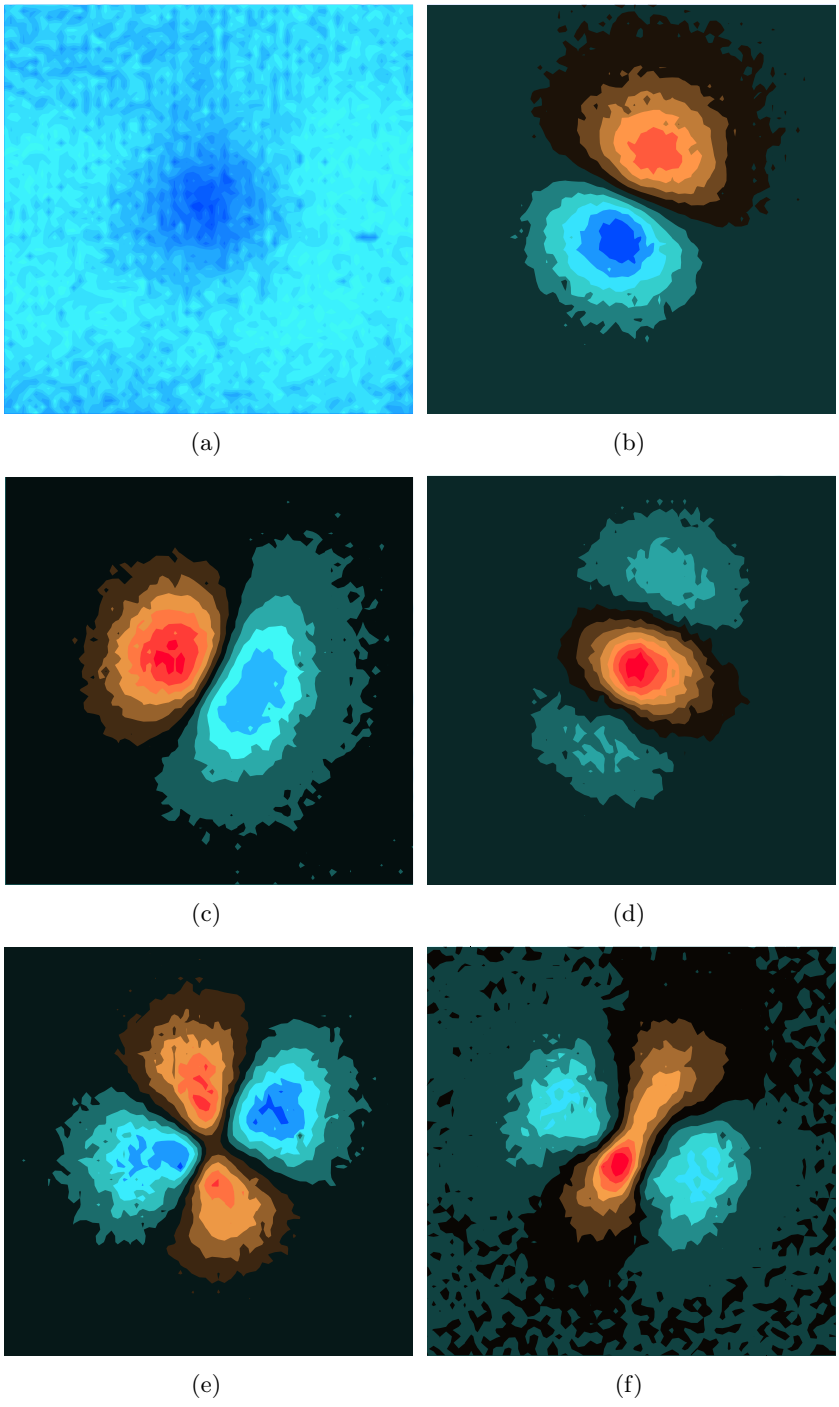

(a) (b) (c) (d) (e) (f)

FIG. 5.18 – Modes computed by singular value decomposition of the dye intensity time series for $\alpha = 9°$ and $F_p = 35$ Hz (Re = 18800 and $W_0 = 0.32$). The six most energetic modes are shown.

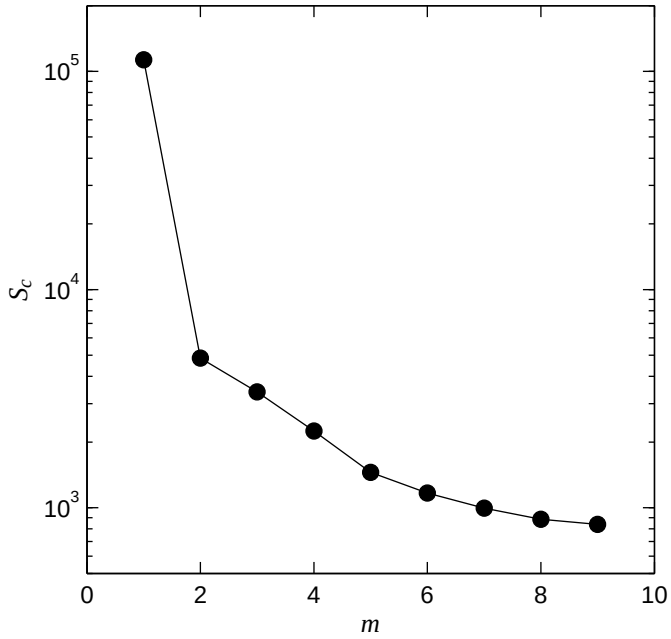

FIG. 5.19 – Singular value distribution of the most energetic modes for $\alpha = 9°$ and $F_p = 35$ Hz (Re = 18800 and $W_0 = 0.32$).

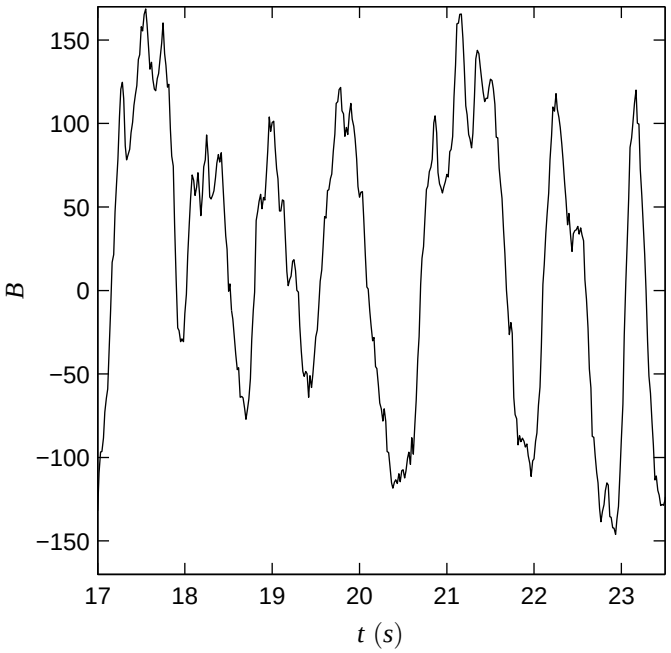

FIG. 5.20 – Temporal evolution of the projection of the dye images on mode 2 for $\alpha = 9°$ and $F_p = 35$ Hz (Re = 18800 and $W_0 = 0.32$).

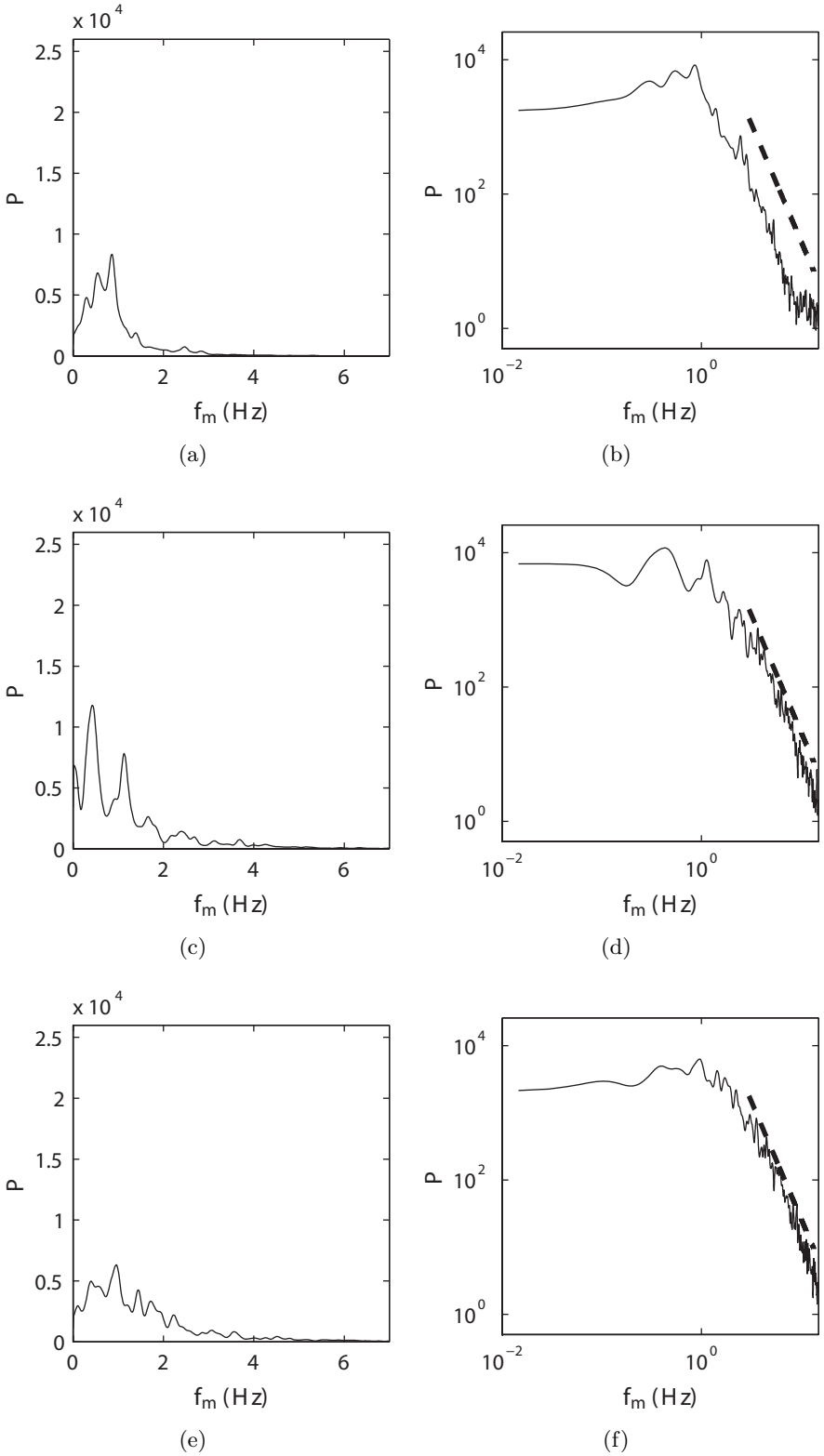

FIG. 5.21 – Power spectral density P of the projection of the dye image series on mode 2, as function of the frequency f_m, for $\alpha = 6°$ and $F_p = 25$ Hz, 35 Hz and 45 Hz (top to bottom). The slope of the dashed line is -3.5.

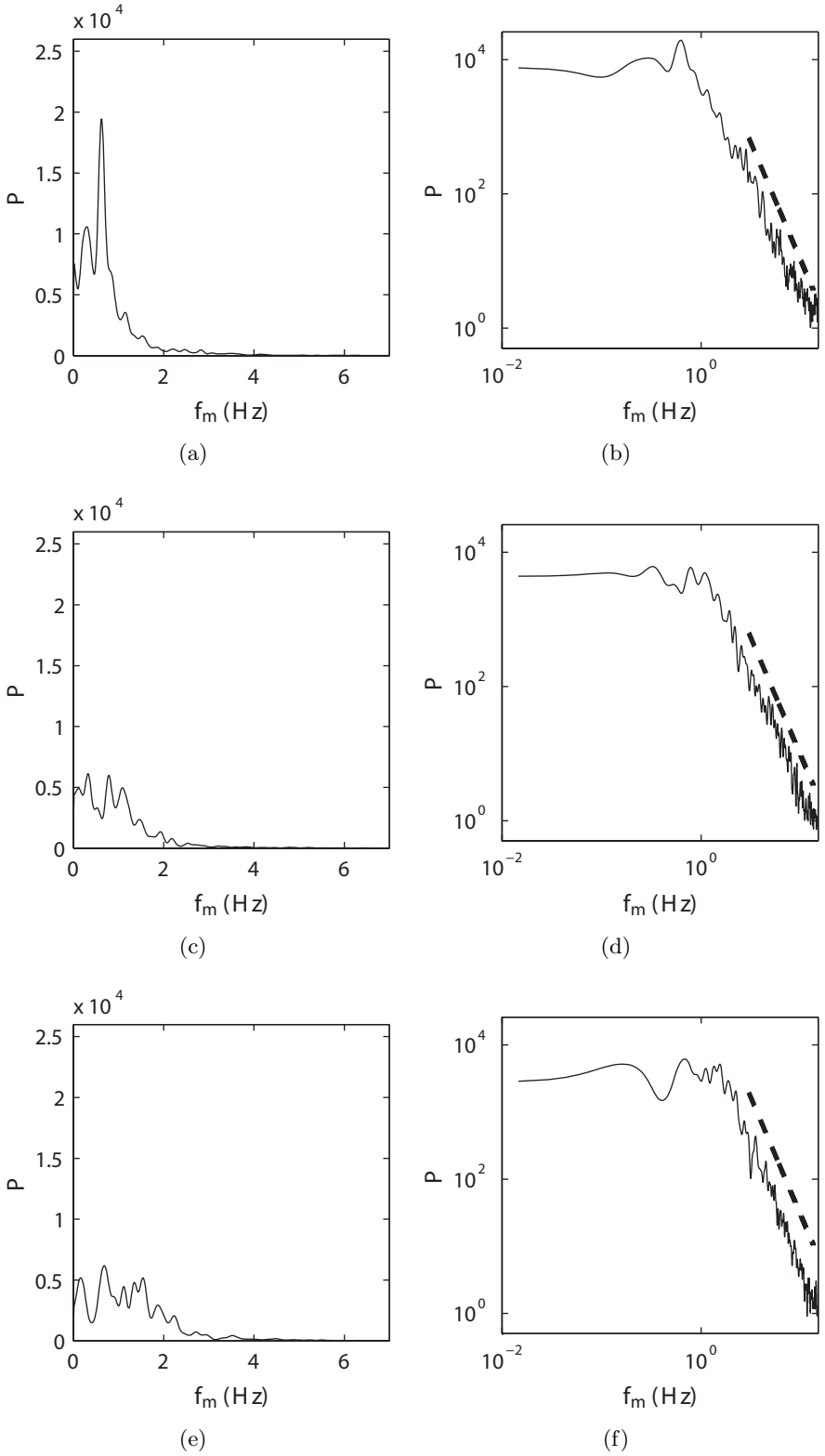

FIG. 5.22 – Same as figure 5.21, for $\alpha = 9°$.

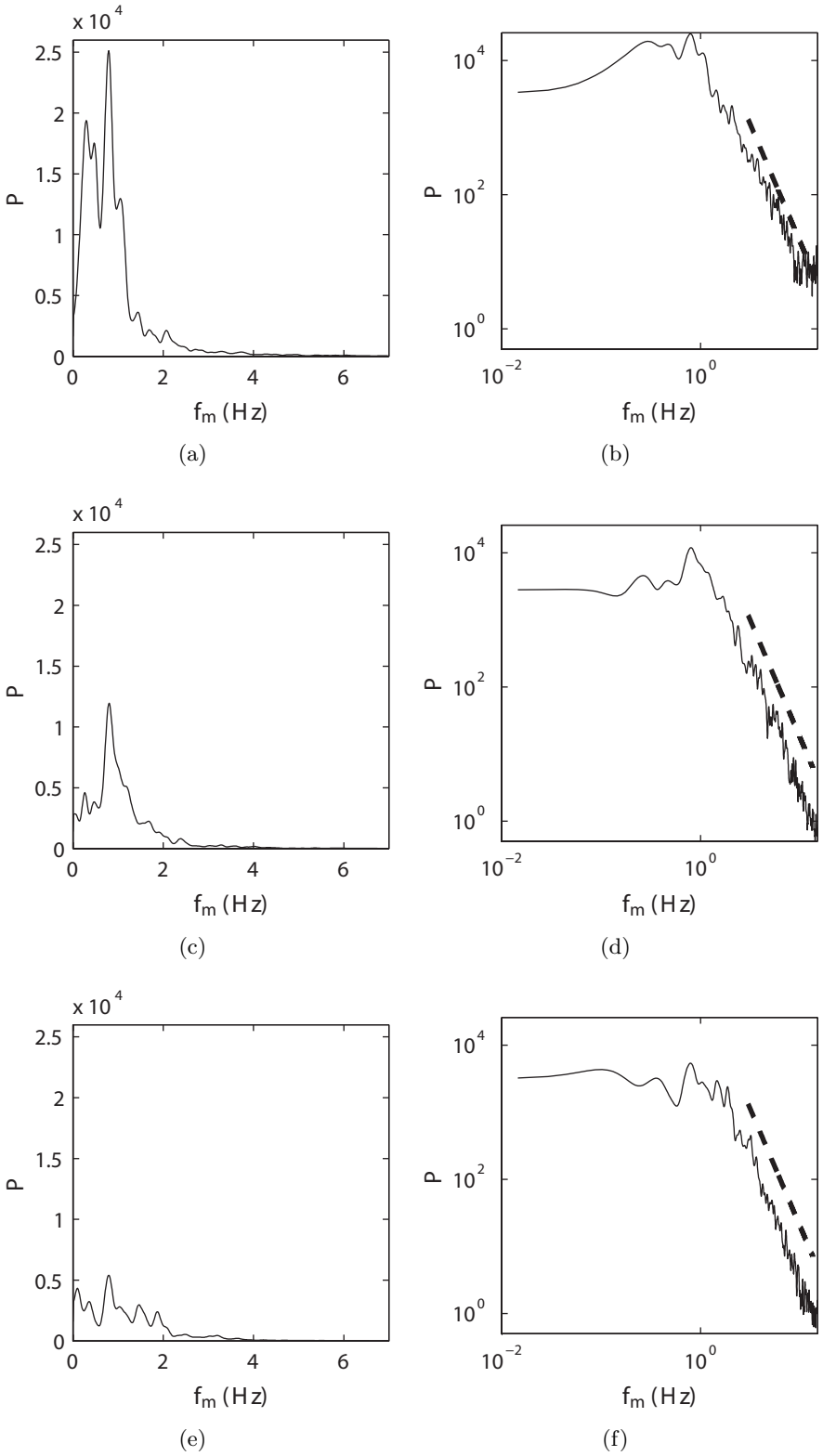

FIG. 5.23 – Same as figure 5.21, for $\alpha = 12°$.

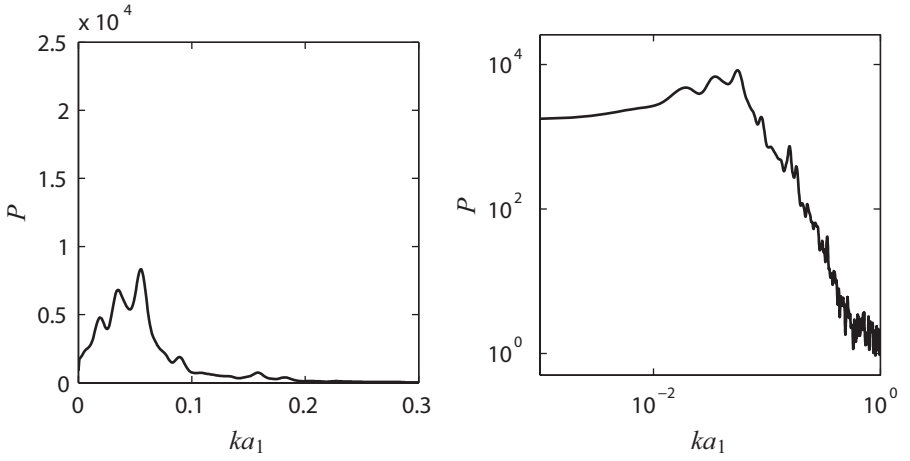

$\alpha = 6°$, $F_p = 25$ Hz (Re $= 8700$, $W_0 = 0.27$)

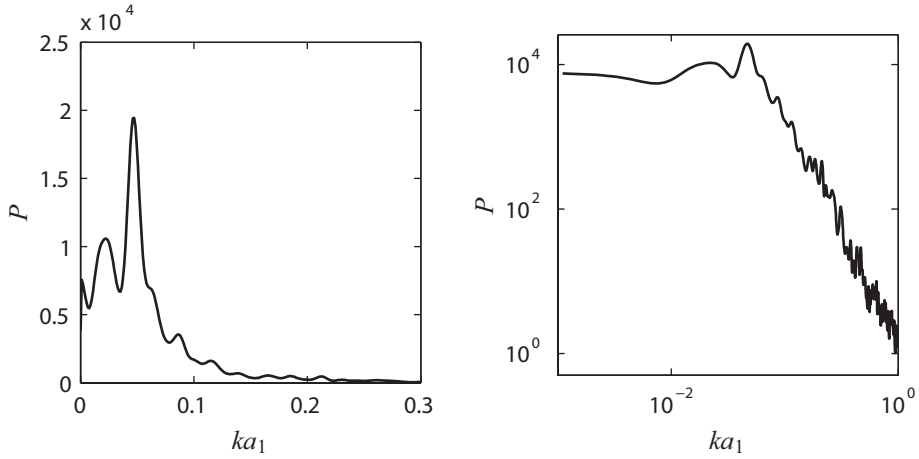

$\alpha = 9°$, $F_p = 25$ Hz (Re $= 12700$, $W_0 = 0.31$)

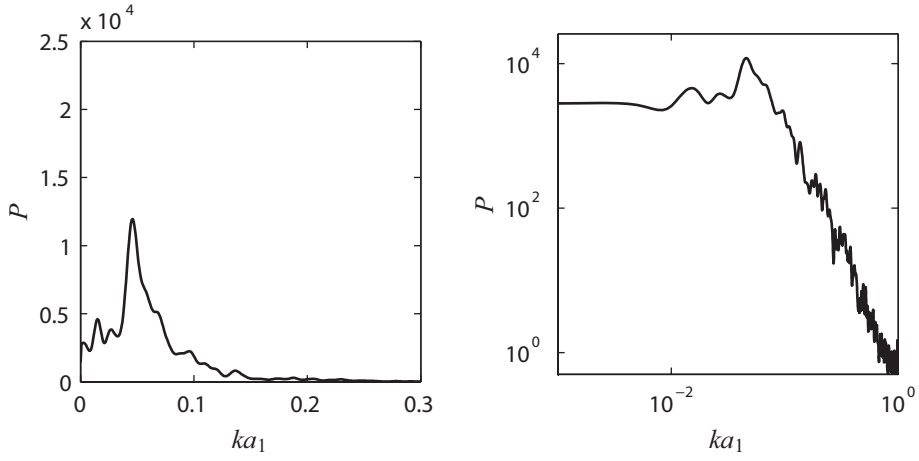

$\alpha = 12°$, $F_p = 35$ Hz (Re $= 22500$, $W_0 = 0.36$)

FIG. 5.24 – Power spectral density P of the projection of the dye image series on the displacement mode 2, as a function of the non-dimensional wave number $ka_1 = 2\pi a_1 f_m / U_\infty$.

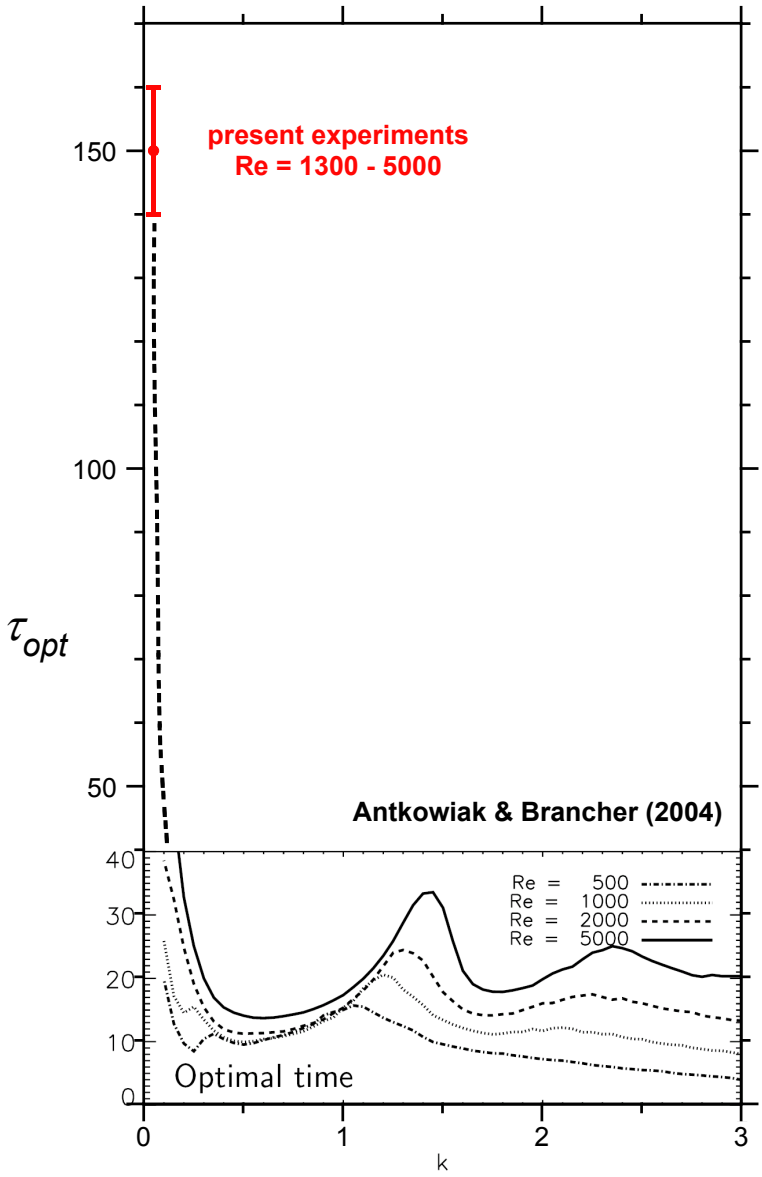

FIG. 5.25 – Optimal time as function of wave number. Results from Antkowiak & Brancher Antkowiak & Brancher (2004) for a Gaussian vortex without axial flow are compared to the present observations. In this figure, the Reynolds number is defined as $\mathrm{Re} = \Gamma/(2\pi\nu)$.

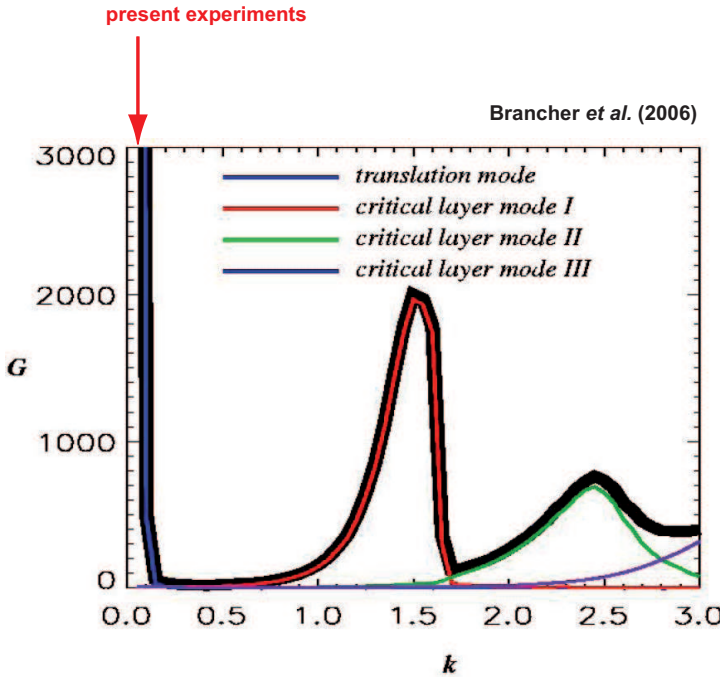

FIG. 5.26 – Optimal gain as function of wave number, and associated perturbation structure, for a Gaussian vortex without axial flow. From Brancher *et al.* Brancher *et al.* (2006).

Chapitre 6

Conclusions

6.1 Synthèse

Dans cette étude nous avons apporté des résultats expérimentaux et numériques sur la dynamique et la stabilité des tourbillons avec une vitesse axiale.

En utilisant un code à éléments spectraux, nous avons réalisé l'étude de stabilité linéaire d'une paire bidimensionnelle de tourbillons co–rotatifs de Batchelor, relativement à des perturbations tridimensionnelles. Cette étude a été faite pour une plage de nombres d'onde axiaux et d'écoulements axiaux. Plusieurs nombres de Reynolds et écartements des tourbillons ont été étudiés. Dans le cas sans écoulement axial, les modes principaux (combinaison de modes de Kelvin dont le label n des branches sont égaux) de nombre azimutaux $(-1, 1)$ sont instables. Nous avons montré que quand l'écoulement axial augmente, les modes $(-1, 1)$ se stabilisent. À la place, des modes instables mettant en jeux des ondes de Kelvin à géométrie azimutale plus complexes ont été identifiés. On a ainsi pu observer les modes principaux $(-2, 0)$, $(-3, -1)$ et $(-4, -2)$. Des modes non–principaux ont également été mis à jour, avec des taux de croissance plus faibles. La présence de modes de couche critique a également été mise en évidence. L'établissement de cette cartographie est importante dans la mesure où, si un jour l'instabilité elliptique est utilisée en aéronautique pour accélérer la destruction des sillages d'avion, il y a de fortes chances que ce soit au niveau des paires co–rotatives formées par les tourbillons de bout d'aile et de volet. Ces deux tourbillons ne subsistent que dans le sillage proche de l'avion et finissent pas fusionner.

Par la suite, nous avons étudié expérimentalement l'instabilité elliptique sur une paire de tourbillons co– et contra– rotatifs, générés au moyen de deux demi–ailes plongées dans l'écoulement d'un canal hydrodynamique. Nous avons développé une méthode de Vélocimétrie Stéréoscopique Par Image de Particules pour mesurer l'écoulement de base. Au moyen de visualisations, nous avons pu mesurer la longueur d'onde de l'instabilité elliptique sur les paires de tourbillons. Dans le cas contra-rotatif, le résultat est en bon accord avec une analyse de stabilité linéaire réalisée sur l'écoulement expérimental. Le taux de croissance mesuré est très proche de celui du mode de l'instabilité elliptique le plus instable numériquement. La structure azimutale du mode a été précisément identifiée par une technique de POD (Proper Orthogonal Decomposition) pratiquée sur des visualisations d'un vortex. On a ainsi mis en évidence deux modes de Kelvin de nombres d'onde

azimutaux $m = 0$ et $m = 2$, correspondant exactement au mode numérique obtenu. L'instabilité elliptique est donc clairement identifiée dans une paire de tourbillons avec écoulement axial.

Nous avons, pour finir, généré un seul tourbillon dans un canal hydrodynamique. Plusieurs nombres de Reynolds ont été étudiés. Nous avons estimé l'amplitude du meandering en mesurant le déplacement du centre du vortex. Les directions de déplacement principales ont été identifiées. Ensuite, au moyen d'une POD sur une série de visualisations d'un vortex, on a identifié les modes de déplacement (de nombre azimutal $m = 1$). Ces modes imposent au vortex une oscillation à grande longueur d'onde que l'on a identifiée. On a comparé ces observations avec les résultats théoriques concernant la croissance transitoire dans un tourbillon gaussien, présentés par Antkowiak & Brancher (2004). Concernant la structure du mode et la longueur d'onde, un bon accord a été montré entre nos mesures et la perturbation optimale au temps d'observation. Cet accord suggère que le meandering peut être expliqué par les phénomènes de croissance transitoire des perturbations.

6.2 Perspectives

Au cours de notre étude, nous avons visualisé des modes de l'instabilité elliptique mettant en jeux des modes de Kelvin de nombre azimutaux $m = 2$. Les études numériques et théoriques prédisaient bien cela. À la vue de la cartographie des modes, il semble difficile qu'un mode à nombre d'onde axial plus élevé soit le plus instable. Cependant, on peut tenter d'exciter certains modes, notamment le mode $(1, 3, 1)$. Il faut quand-même préciser que l'excitation appropriée n'est pas évidente à trouver. Il est peut-être possible de s'appuyer sur une analyse de perturbation optimale similaire à celle de Brion *et al.* (2007) pour se donner des idées.

Pour connaître l'impact de l'instabilité elliptique sur le tourbillon fusionné, il est nécessaire de mener une étude non-linéaire. Un pas dans cette direction a été franchi par Schaeffer & Le Dizès (2008) qui ont montré que le tourbillon issu d'une fusion de deux tourbillons sujets au mode de l'instabilité elliptique $(-2, 0)$, étaient plus diffus qu'un tourbillon issu d'une fusion de deux tourbillons stables. Pour diminuer le danger des sillages d'avion, cela est encourageant car ça implique que le moment de roulis perçu par un avion traversant le tourbillon va diminuer (Fabre, 2002).

Concernant le phénomène de meandering, la concordance entre les observations et la théorie de croissance transitoire des perturbations d'un tourbillon existe. Pour pouvoir conclure de manière définitive sur le lien établi, une possibilité serait de générer un tourbillon dans un canal ou une soufflerie en faisant varier, entre chaque expérience, la distance entre le tourbillon et une paroi solide. Si une corrélation entre la distance à la paroi et la fréquence du meandering mesurée était mise en évidence, on pourrait clairement nommer la croissance transitoire des perturbations du tourbillon comme cause du meandering.

Bibliographie

Alkislar, M. B., Krothapali, A. & Lourenco, L. M. 2003 Structure of a screeching rectangular jet : a stereoscopic particle image velocimetry study. *J. Fluid Mech.* **489**, 121–154.

Antkowiak, A. & Brancher, P. 2004 Transient energy growth for the lamb–oseen vortex. *Phys. Fluids* **16** (1).

Arendt, S., Fritts, D. C. & Andreassen, Ø. 1997 The initial value problem for Kelvin vortex waves. *J. Fluid Mech.* **344**, 181–212.

Baker, G. R., Barker, S. J., Bofah, K. K. & Saffman, P. G. 1974 Laser anemometer measurements of trailing vortices in water. *J. Fluid Mech.* **65** (2), 325–336.

Bashforth, F. & Adams, J. C. 1883 *An Attempt to Test the Theories of Capillary Action by Comparing the Theoretical and Measured Forms of Drops of Fluid*. Cambridge University Press.

Bassom, A. P. & Gilbert, A. D. 1999 The spiral wind-up and dissipation of vorticity and a passive scalar in a strained planar vortex. *J. Fluid Mech.* **398**, 245–270.

Batchelor, G. K. 1964 Axial flow in trailing line vortices. *J. Fluid Mech.* **20**, 645–658.

Batchelor, G. K. 1967 *An Introduction to Fluid Dynamics*.

Bayly, B. J. 1986 Three-dimensional instability of elliptical flow. *Phys. Rev. Lett.* **57**, 2160–2163.

Berkooz, G., Holmes, P. & Lumley, L. 1993 The proper orthogonal decomposition in the analysis of turbulent flows. *Annu. Rev. Fluid Mech.* **25**, 539–75.

Billant, P., Brancher, P. & Chomaz, J.-M. 1999 Three-dimensional stability of a vortex pair. *Phys. Fluids* **11**, 2069–2077.

Boulanger, N., Meunier, P. & Le Dizès, S. 2007 Structure of a tilted stratified vortex. *J. Fluid Mech.* **583**, 443–458.

Boulanger, N., Meunier, P. & Le Dizès, S. 2008 Instability of a tilted vortex in stratified fluid. *J. Fluid Mech.* **596**, 1–20.

Brancher, P., Fabre, D. & Antkowiak, A. 2006 Vortex meandering : a vortex response to background turbulence FAR-Wake Work Package 1 Technical Meeting, 14-15 September 2006, Málaga, Spain.

Brion, V., Sipp, D. & Jacquin, L. 2007 Optimal amplification of the crow instability. *Phys. Fluids* **19**.

Bristol, R. L., Ortega, J. M., Marcus, P. S. & Savaş, Ö. 2004 On cooperative instabilities of parallel vortex pairs. *J. Fluid Mech.* **517**, 331–358.

Canuto, C. 1988 *Spectral methods in fluid dynamics*. Springer-Verlag, New-York.

Carlier, J. & Stanislas, M. 2005 Experimental study of eddy structures in a turbulent boundary layer using particle image velocimetry. *J. Fluid Mech.* **535**, 143–188.

Chatterjee, A. 2000 An introduction to the proper orthogonal decomposition. *Current Science* **78** (7), 808–817.

Chen, A. L., Jacob, J. D. & Savaş, Ö. 1999 Dynamics of corotating vortex pairs in the wakes of flapped airfoils. *J. Fluid Mech.* **382**, 155–193.

Corsiglia, V. R., Schwind, R., G. & Chigier, N. A. 1973 Rapid scanning, three-dimensional hot-wire anemometer surveys of wing-tip vortices. *J. Aircraft* **10**, 752–757.

Crank, J. & Nicolson, P. 1947 A practical method for numerical evaluation of solutions of partial differential equations of the heat conduction type. *Proc. Camb. Phil. Soc.* **43**, 50–64.

Crouch, J. D. & Jacquin, L. 2005 Aircraft trailing vortices / tourbillons de sillages d'avions. *C. R. Physique* **6**, 4–5.

Crow, S. C. 1970 Stability theory for a pair of trailing vortices. *AIAA J.* **8** (12), 2172–2179.

Delbende, I., Chomaz, J.-M. & Huerre, P. 1998 Absolute/convective instabilities in the batchelor vortex : a numerical study of the linear impulse response. *J. Fluid Mech.* **355**, 229–254.

Devenport, W. J., Rife, M. C., Liapis, S. I. & Follin, G. J. 1996 The structure and development of a wing-tip vortex. *J. Fluid Mech.* **312**, 67–106.

Devenport, W. J., Vogel, C. M. & Zsoldos, J. S. 1999 Flow structure produced by the interaction and merger of a pair of co-rotating wing-tip vortices. *J. Fluid Mech.* **394**, 357–377.

Devenport, W. J., Zsoldos, J. S. & Vogel, C. M. 1997 The structure and development of a counter-rotating wing-tip vortex pair. *J. Fluid Mech.* **332**, 71–104.

Eloy, C. & Le Dizès, S. 2001 Stability of the Rankine vortex in a multipolar strain field. *Phys. Fluids* **13** (3), 660–676.

Eloy, C., Le Gal, P. & Le Dizès, S. 2000 Experimental study of the multipolar vortex instability. *Phys. Rev. Lett.* **85** (16), 145–166.

Fabre, D. 2002 Instabilitités et instationnarités dans les tourbillons : application aux sillages d'avions. PhD thesis, ONERA/Université Paris VI.

Fabre, D., Cossu, C. & Jacquin, L. 2000 Spatio-temporal development of the long and short-wave vortex-pair instabilities. *Phys. Fluids* **12**, 1247–1250.

Fabre, D. & Jacquin, L. 2004*a* Short-wave cooperative instabilities in representative aircraft vortices. *Phys. Fluids* **16**, 1366–1378.

Fabre, D. & Jacquin, L. 2004*b* Viscous instabilities in trailing vortices at large swirl numbers. *J. Fluid Mech.* **500**, 239–262.

Fabre, D., Jacquin, L. & Loof, A. 2002 Optimal perturbations in a four-vortex aircraft wake in counter-rotating configuration. *J. Fluid Mech.* **451**, 319–328.

Fabre, D., Sipp, D. & Jacquin, L. 2006 The Kelvin waves and the singular modes of the Lamb-Oseen vortex. *J. Fluid Mech.* **551**, 235–274.

Fletcher, C. A. J. 1984 *Computational Galerkin methods*. Springer-Verlag.

Fletcher, C. A. J. 1991 *Computational techniques for fluid dynamics, vol 1*. Springer-Verlag.

Fontane, J., Brancher, P. & Fabre, D. 2008 Stochastic forcing of the lamb-oseen vortex. *J. Fluid Mech.* Submitted.

Gasparek, E. P. 1957 Viscous decay of a vortex. Master's thesis, Syracuse University, NY.

Gerz, T., Holzäpfel, F. & Darracq, D. 2002 Commercial aircraft wake vortices. *Prog. Aerospace Sci.* **38**, 181–208.

Green, S. I. & Acosta, A. J. 1991 Unsteady flow in trailing vortices. *J. Fluid Mech.* **227**, 107–134.

Heaton, C. 2006 Centre modes in inviscid swirling flows, and their application to the stability of the batchelor vortex. *J. Fluid Mech.* (accepted).

Hoerner, S., F. 1965 *Fluid Dynamic Drag*.

Jacob, J. D. 1995 Experimental investigation of the trailing vortex wake of rectangular airfoils. PhD thesis, University of California at Berkeley.

Jacquin, L., Fabre, D., Geffroy, P. & Coustols, E. 2001 The properties of a transport aircraft wake in the extended nearfield : an experimental study. *AIAA Paper* p. 1038.

Jacquin, L., Fabre, D., Sipp, D., Theofilis, V. & Vollmers, H. 2003 Instability and unsteadiness of wake vortices. *Aerosol Sci. Technol.* **7** (8), 577–593.

Jimenez, J. 1975 Stability of a pair of co-rotating vortices. *Phys. Fluids* **18** (11), 1580–1581.

Jiménez, J., Moffatt, H. K. & Vasco, C. 1996 The structure of the vortices in freely decaying two dimensional turbulence. *J. Fluid Mech.* **313**, 209–222.

Karniadakis, G. E., Israeli, M. & Orszag, S. A. 1991 High-order splitting methods of the incompressible Navier-Stokes equations. *J. Comp. Phys.* **97**, 414–443.

Karniadakis, G. E. & Sherwin, S. J. 1999 *Spectral /hp Element Methods for CFD*. Oxford University Press.

Katz, J. & Bueno Galdo, J. 1989 Effect of roughness on rollup of tip vortices on a rectangular hydrofoil. *J. Aircraft* **26**, 247–253.

Kelvin, Lord 1880 Vibrations of a columnar vortex. *Phil. Mag.* **10**, 155–168.

Kerswell, R. R. 2002 Elliptical instability. *Annu. Rev. Fluid Mech.* **34**, 83–113.

Klein, R. & Knio, O. M. 1995 Asymptotic vorticity structure and numerical simulation of slender vortex filaments. *J. Fluid Mech.* **284**, 275.

Klein, R., Majda, A. J. & Damodaran, K. 1995 Simplified equations for the interaction of nearly parallel vortex filaments. *J. Fluid Mech.* **288**, 201–248.

Kreiszig, E. 1993 *Advanced Engineering Mathematics : Seventh Edition*. John Wiley & Sons.

Krutzsch, C.-H. 1939 Über eine experimenell beobachtete erscheinung an wirbelringen bei ihrer translatorischen bewegung in wirklichen flüssigkeiten. *Annalen der Physik* **427**, 497–523.

Lacaze, L., Birbaud, A.-L. & Le Dizès, S. 2005*a* Elliptic instability in a Rankine vortex with axial flow. *Phys. Fluids* **17** (017101).

Lacaze, L., Le Gal, P. & Le Dizès, S. 2004 Elliptical instability in a rotating spheroid. *J. Fluid Mech.* **505**, 1–22.

Lacaze, L., Le Gal, P. & Le Dizès, S. 2005*b* Elliptical instability of a flow in a rotating shell. *Phys. Earth Planet. Int.* **151**, 194–205.

Lacaze, L., Ryan, K. & Le Dizès, S. 2007 Elliptic instability in a strained Batchelor vortex. *J. Fluid Mech.* **577**, 341–361.

Landman, M. J. & Saffman, P. G. 1987 The three-dimensional instability of strained vortices in a viscous fluid. *Phys. Fluids* **30** (8), 2339–2342.

Laporte, F. & Corjon, A. 2000 Direct numerical simulations of the elliptic instability of a vortex pair. *Phys. Fluids* **12** (5), 1016–1031.

Le Dizès, S. 2004 Viscous critical-layer analysis of vortex normal modes. *Stud. Appl. Math.* **112** (4), 315–332.

Le Dizès, S. & Lacaze, L. 2005 An asymptotic description of vortex Kelvin modes. *J. Fluid Mech.* **542**, 69–96.

Le Dizès, S. & Laporte, F. 2002 Theoretical predictions for the elliptic instability in a two-vortex flow. *J. Fluid Mech.* **471**, 169–201.

Le Dizès, S. & Verga, A. 2002 Viscous interactions of two co-rotating vortices before merging. *J. Fluid Mech.* **467**, 389–410.

Leibovich, S., Brown, S. N. & Patel, T. 1986 Bending waves on inviscid columnar vortices. **173**, 595.

Leontini, J. 2007 A numerical investigation of transversely-oscillating cylinders in two-dimensional flow. PhD thesis, Monash University.

Leontini, J. S., Stewart, B. E., Thompson, M. C. & Hourigan, K. 2006 Wake state and energy transitions of an oscillating cylinder at low reynolds number. *Physics of fluids* **18** (067101).

Leweke, T. & Williamson, C. H. K. 1998 Cooperative elliptic instability of a vortex pair. *J. Fluid Mech.* **360**, 85–119.

Liang, Y. C., Lee, H. P., Lim, S. P., Lin, W. Z., Lee, K. H. & Wu, C. G. 2002 Proper orthogonal decomposition and its applications–part *i* : theory. *J. Sound Vib.* **252** (3), 527–544.

Liu, H.-T. 1992 Effects of ambient turbulence on the decay of a trailing vortex wake. *J. Aircraft* **29**, 255–263.

Malkus, W. V. R. 1989 An experimental study of global instabilities due to tidal (elliptical) distortion of a rotating elastic cylinder. *Geophys. Astrophys. Fluid Dynamics* **48**, 123–134.

Mason, W. H. & Marchman, J. F. 1972 The farfield structure of aircraft wake turbulence. *AIAA, Aerospace Sciences Meeting, 10th, San Diego, Calif., Jan 17-19* .

Maxworthy, T. 1972 The structure and stability of vortex rings. *J. Fluid Mech.* **51**, 15–32.

Meunier, P. 2001 étude expérimentale de deux tourbillons corotatifs. PhD thesis, Université d'Aix-Marseille 1.

Meunier, P., Le Dizès, S. & Leweke, T. 2005 Physics of vortex merging. *C. R. Physique* **6**, 431–450.

Meunier, P. & Leweke, T. 2001 Three-dimensional instability during vortex merging. *Phys. Fluids* **13** (10), 2747–2750.

Meunier, P. & Leweke, T. 2003 Analysis and optimization of the error caused by high velocity gradients in particle image velocimetry. *Exp. Fluids* **35** (5), 408–421.

Meunier, P. & Leweke, T. 2005 Elliptic instability of a co-rotating vortex pair. *J. Fluid Mech.* **533**, 125–159.

Moffatt, H. K., Kida, S. & Ohkitani, K. 1994 Stretched vortices -the sinews of turbulence ; large-Reynolds-number asymptotics. *J. Fluid Mech.* **259**, 241–264.

Moore, D. W. & Saffman, P. G. 1971 Structure of a line vortex in an imposed strain. In *Aircraft wake turbulence* (ed. Olsen, Golburg & Rogers), pp. 339–354. Plenum.

Moore, D. W. & Saffman, P. G. 1973 Axial flow in laminar trailing vortices. *Proc. R. Soc. Lond.* A **333** (1595), 491–508.

Moore, D. W. & Saffman, P. G. 1975 The instability of a straight vortex filament in a strain field. *Proc. R. Soc. Lond.* A **346**, 413–425.

Moulton, F. R. 1926 *New methods in exterior ballistics*. University of Chicago Press.

Ortega, J. M., Bristol, R. L. & Savaş, Ö. 2003 Experimental study of the stability of unequal–strength counter–rotating vortex pairs. *J. Fluid Mech.* **474**, 35–84.

Otheguy, P., Chomaz, J.-M. & Billant, P. 2006 Elliptic and zigzag instabilities on co-rotating vertical vortices in a stratified fluid. *J. Fluid Mech.* **553**, 253–272.

Parras, L. & Fernandez-Feria, R. 2007 Spatial stability and the onset of absolute instability of batchelor's vortex for high swirl numbers. *J. Fluid Mech.* **583**, 27–43.

Pierrehumbert, R. T. 1986 Universal short-wave instability of two-dimensional eddies in an inviscid fluid. *Phys. Rev. Lett.* **57**, 2157–2160.

Pradeep, D. S. & Hussain, F. 2004 Effects of boundary condition in numerical simulations of vortex dynamics. *J. Fluid Mech.* **516**, 115–124.

Prasad, A. K. & Jensen, K. 1995 Scheimpflug stereocamera for particle image velocimetry in liquid flows. *Applied Optics* **34** (30), 7092.

Rennich, C. & Lele, S. K. 1997 Numerical method for incompressible vortical flows with two unbounded directions. *J. Comp. Phys.* **137**, 101–129.

Rossow, V. J. 1999 Lift-generated vortex of subsonic transport aircraft. *Prog. Aerospace Sci.* **35**, 507–660.

Roy, C. & Leweke, T. 2008 Experiments on vortex meandering. *FAR-Wake European Project* **TR 1.1.1-4**.

Roy, C., Leweke, T., Thompson, M. C. & Hourigan, K. 2008*a* Elliptic instability in vortex pairs with axial core flow. *Phys. Fluids* Submitted.

Roy, C., Schaeffer, N., Le Dizès, S. & Thompson, M. C. 2008*b* Stability of a pair of co–rotating vortices with axial flow. *Phys. Fluids* **20** (9), 094101.

Ryan, K. 2004 The analysis of wake structures behind stationary, freely oscillating and tethered cylinders. PhD thesis, Monash University.

Ryan, K., Thompson, M. C. & Hourigan, K. 2005 Three-dimensional transition in the wake of elongated bluff bodies. *J. Fluid Mech.* **538**, 1–29.

Saffman, P. G. 1992 *Vortex dynamics*. Cambridge University Press.

Sarpkaya, T. 1983 Trailing vortices in homogeneous and density-stratified media. *J. Fluid Mech.* **136**, 85–109.

Schaeffer, N. & Le Dizès, S. 2008 Nonlinear dynamics of the short-wavelength elliptic instability. *Phys. Fluids* Submitted.

Scheimpflug, T. 1904 Improved method and apparatus for the systematic alteration or distortion of plane pictures and images means of lenses and mirrors for photography and for other purposes. *Great Britain Patent No. 1196* .

Schmid, P. J. & Rossi, M. 2004 Three-dimensional stability of a burgers vortex. *J. Fluid Mech.* **500**, 102–112.

Scorer, R. S. & Davenport, L. J. 1970 Contrails and aircraft downwash. *J. Fluid Mech.* **43** (3), 451–464.

Sheard, G., Thompson, M. C. & Hourigan, K. 2003 From spheres to circular cylinder : the stability an flow structures of bluff body wakes. *J. Fluid Mech.* **492**, 147–180.

Sheard, G. J. 2004 The stability and characteristics of the flow pas rings. PhD thesis, Monash University.

Singh, P. I. & Uberoi, M. S. 1976 Experiments on vortex stability. *Exp. Fluids* **19** (12), 1858–1863.

Sipp, D. & Jacquin, L. 2003 Widnall instabilities in vortex pairs. *Phys. Fluids* **15**, 1861–1874.

Sipp, D., Jacquin, L. & Cossu, C. 2000 Self-adaptation and viscous selection in concentrated two-dimensional dipoles. *Phys. Fluids* **12** (2), 245–248.

Spalart, P. R. 1998 Airplane trailing vortices. *Annu. Rev. Fluid Mech.* **30**, 107–138.

Taylor, J. R. 1997 *An Introduction to Error Analysis, the Study of Uncertainties in Physical Measurements*, second edition edn. University Science Books.

Thomas, P. J. & Auerbach, D. 1994 The observation of the simultaneous development of a long- and a short-wave instability mode on a vortex pair. *J. Fluid Mech.* **265**, 289–302.

Thompson, D. H. 1975 Experimental study of axial flow in wing tip vortices. *J. Aircraft* **8**, 496–503.

Thompson, M. C., Hourigan, K. & Sheridan, J. 1996 Three-dimensional instabilities in the wake of a circular cylinder. *Experimental Thermal and Fluid Science* **12**, 190–196.

Thompson, M. C., Leweke, T. & Provansal, M. 2001*a* Kinematics and dynamics of sphere wake transition. *J. Fluids Struct.* **15**, 575–585.

Thompson, M. C., Leweke, T. & Williamson, C. H. K. 2001*b* The physical mechanism of transition in bluff body wakes. *J. Fluids Struct.* **15**, 607–616.

Ting, L. & Tung, C. 1965 Motion and decay of a vortex in a nonuniform stream. *Phys. Fluids* **8** (6), 1039–1051.

Tombach, I. 1973 Observations of atmospheric effects on vortex wake behavior. *J. Aircraft* **10** (11), 641–647.

Tsai, C.-Y. & Widnall, S. E. 1976 The stability of short waves on a straight vortex filament in a weak externally imposed strain field. *J. Fluid Mech.* **73** (4), 721–733.

Vincent, A. & Meneguzzi, M. 1991 The spatial structure and statistical properties of homogeneous turbulence. *J. Fluid Mech.* **225**, 1–20.

Waleffe, F. 1990 On the three-dimensional instability of strained vortices. *Phys. Fluids* A **2** (1), 76–80.

Widnall, S. E., Bliss, D. & Tsai, C.-Y. 1974 The instability of short waves on a vortex ring. *J. Fluid Mech.* **66** (1), 35–47.

Widnall, S. E., Bliss, D. B. & Zalay, A. 1971 Theoretical and experimental study of the instability of a vortex pair. *Aircraft Wake Turbulence and its Detection (ed. J. H. Olsen, A. Goldberg & M. Rogers), p. 305. Plenum.* .

Widnall, S. E. & Sullivan, J. P. 1973 On the stability of vortex ring. *Proc. R. Soc. Lond.* A **332**, 335–353.

Willert, C. 1997 Stereoscopic digital particle image velocimetry for application in wind tunnel flows. *Measurement Science and Technology* **8**, 1465–1479.

Zaman, K. B. M. Q., McKinzie, D. J. & Rumsey, C. L. 1989 A natural low–frequency oscillation of the flow over an airfoil nea stalling conditions. *J. Fluid Mech.* **202**, 403–442.

Zang, W. & Prasad, A. K. 1997 Performance evaluation of a scheimpflug stereocamera for particle image velocimetry. *Applied Optics* **36** (33), 8738–8744.

Résumé

Cette étude fondamentale présente des résultats expérimentaux et numériques concernant la dynamique et la stabilité de tourbillons avec écoulement axial, pour des nombres de Reynolds modérés. La première partie de la thèse s'attache à étudier l'instabilité elliptique dans des paires de tourbillons co- et contra-rotatifs, avec écoulement axial. L'étude de stabilité de deux tourbillons de co-rotatifs de Batchelor, réalisée avec un code à éléments spectraux, a permis d'identifier clairement des modes de l'instabilité elliptique à structure spatiale complexe, pour différentes valeurs de l'écoulement axial et du nombre d'onde axial. Expérimentalement, l'instabilité elliptique a été mise en évidence dans des paires de tourbillons co- et contra-rotatifs, générées au moyen de deux demi-ailes placées dans un canal hydrodynamique. L'analyse POD (Proper Orthogonal Decomposition) d'images acquises par une caméra rapide a mené à une caractérisation précise du mode de l'instabilité observé, qui implique des perturbations avec des nombres azimutaux m=0 et m=2, remplissant la condition de résonance de l'instabilité elliptique. L'analyse numérique de stabilité des vortex expérimentaux, caractérisés par une méthode de Vélocimétrie Stéréoscopique par Images de Particules), a montré le même mode instable. Les longueurs d'onde et taux de croissance expérimentaux et numériques sont en bon accord. La deuxième partie de l'étude porte sur le"vortex meanderin", abordé expérimentalement en générant un vortex de bout d'aile. Une analyse détaillée des perturbations du tourbillon permet de mettre ce phénomène en relation avec la théorie de croissance transitoire des perturbations d'un vortex isolé.

Summary

This fundamental study presents experimental and numerical results concerning the dynamics and stability of vortices with axial core flow, for moderate Reynolds numbers. The first part of the thesis focuses on the elliptic instability in co- and counter-rotating vortex pairs with axial core flow. The stability analysis of two Batchelor vortices clearly identifies elliptic instability modes with complex spatial structures, for a range of axial flows and axial wave numbers. Experimentally, the elliptic instability was evidenced in co- and counter-rotating vortices, generated by two half wings in a water channel. High-speed video recordings and Proper Orthogonal Decomposition of dye visualisations allowed a precise characterisation of the instability mode, which involves perturbations of azimuthal wave numbers m=0 and m=2, fulfilling the elliptic instability resonance condition. The numerical stability analysis of the experimental vortices revealed the same unstable mode. Experimental and numerical wavelengths and growth rates are in good agreement. The second part of the thesis deals with "vortex meandering", studied experimentally by generating a single wing-tip vortex. A detailed analysis of the vortex perturbations successfully links this phenomenon to the transient growth theory, predicting that the most energetic (optimal) perturbation of a Gaussian vortex at a finite time should take the form of a displacement mode. The theoretical axial wavelength of the perturbation is of the same order as the typical length of the vortex displacement oscillation measured experimentally.